TECHNISCHE UNIVERSITÄT MÜNCHEN

Max-Planck-Institut für Physik
(Werner-Heisenberg-Institut)

Methods to improve and understand the sensitivity of high purity germanium detectors for searches of rare events

Oleksandr Volynets

Vollständiger Abdruck der von der Fakultät für Physik der Technischen Universität München zur Erlangung des akademischen Grades eines
Doktors der Naturwissenschaften (Dr. rer. nat.)
genehmigten Dissertation.

Vorsitzender:	Univ.-Prof. Dr. Alejandro Ibarra
Prüfer der Dissertation:	
	1. Priv.-Doz. Dr. Béla Majorovits
	2. Univ.-Prof. Dr. Peter Fierlinger

Die Dissertation wurde am 02.07.2012 bei der Technischen Universität München eingereicht und durch die Fakultät für Physik am 27.07.2012 angenommen.

Abstract

Observation of neutrinoless double beta-decay could answer fundamental questions on the nature of neutrinos. High purity germanium detectors are well suited to search for this rare process in germanium. Successful operation of such experiments requires a good understanding of the detectors and the sources of background.

Possible background sources not considered before in the presently running GERDA high purity germanium detector experiment were studied. Pulse shape analysis using artificial neural networks was used to distinguish between signal-like and background-like events. Pulse shape simulation was used to investigate systematic effects influencing the efficiency of the method. Possibilities to localize the origin of unwanted radiation using Compton back-tracking in a granular detector system were examined.

Systematic effects in high purity germanium detectors influencing their performance have been further investigated using segmented detectors. The behavior of the detector response at different operational temperatures was studied. The anisotropy effects due to the crystallographic structure of germanium were facilitated in a novel way to determine the orientation of the crystallographic axes.

Zusammenfassung

Die Beobachtung des neutrinolosen doppelten Beta-Zerfalls könnte grundlegende Fragen über die Art der Neutrinos beantworten. Detektoren aus hochreinem Germanium sind gut geeignet, um in Germanium nach diesem seltenen Prozess zu suchen. Erfolgreicher Betrieb solcher Experimente erfordert ein gutes Verständnis der Detektoren und der Quellen des Hintergrundes.

Mögliche Hintergrundquellen, die im derzeit laufenden GERDA Experiment nicht betrachtet wurden, werden untersucht. Pulsformanalyse mit künstlichen neuronalen Netzen wurde verwendet, um zwischen Signal- und Hintergrundereignissen zu unterscheiden. Pulsformsimulation wurde verwendet, um systematische Effekte, die die Effizienz der Methode beeinflussen, zu untersuchen. Möglichkeiten den Ursprung der unerwünschten Strahlung unter Verwendung von Compton-Back-Tracking zu lokalisieren, wurde in einem granularen Detektor-System untersucht.

Systematische Effekte die das Verhalten von Deterktoren aus hochreinem Germanium beeinflussen wurden mit segmentierten Detektoren weiter untersucht. Das Ansprechverhalten des Detektors bei verschiedenen Betriebstemperaturen wurde untersucht. Die Anisotropie Effekte, aufgrund der kristallographischen Struktur von Germanium, wurden benutzt um in einer neuartigen Weise die Ausrichtung der kristallographischen Achsen zu bestimmen.

If your model contradicts quantum mechanics, abandon it!
Richard Feynman

Table of Contents

List of abbreviations

$0\nu\beta\beta$	Neutrino-less Double Beta-Decay
$2\nu\beta\beta$	Neutrino-accompanied Double Beta-Decay
ANN	Artificial Neural Network
BFGS [method]	Broyden-Fletcher-Goldfarb-Shanno [method]
BI	Background Index
C.L.	Confidence level
DAQ	Data Acquisition System
DEP	Double Escape Peak
FAP	Full Absorption Peak
FET	Field-Effect Transistor
GERDA	Germanium Detector Array
HPGe [detector]	High Purity Germanium [detector]
LAr	Liquid Argon
MSE	Multi Site Event
PROOF	Parallel ROOT Facility
PSA	Pulse Shape Analysis
ROI	Region of Interest
SP	Survival Probability
SS, **SD**	Single Segment, Single Detector
SSE	Single Site Event

Introduction

Neutrino physics has been an exciting field in fundamental research ever since the neutrino was postulated. A significant step forward was the resolution of the solar neutrino puzzle. For almost 30 years, physicists were trying to find an explanation why the observed number of neutrinos originating from the sun was about a factor of three smaller than expected from the standard solar model. About a decade ago, the origin was identified as oscillations between different neutrino species. Neutrino oscillations were confirmed by a series of experiments studying neutrinos from the sun, the atmosphere, reactors and accelerators.

Oscillation experiments established that neutrino masses are different from zero. However, they cannot establish their absolute mass scale. There is also a question about the nature of the neutrinos which remains unanswered: Are neutrinos distinct from anti-neutrinos (Dirac nature) or are they their own anti-particles (Majorana nature)? The observation of neutrinoless double β-decay, $0\nu\beta\beta$, would be the proof that neutrinos are Majorana particles. A measurement of the half life for this very rare process would also provide information on the absolute mass scale.

The number of experiments searching for neutrinoless double beta-decay in various isotopes is constantly growing. Some of them are presently being constructed, some are already taking data. Searches for $0\nu\beta\beta$ in the germanium isotope ^{76}Ge are particularly tempting because high purity germanium is a semiconductor material used to manufacture detectors that have a very high detection efficiency and a very good energy resolution. In addition, high purity germanium is one of the purest men-made materials, thus minimizing the intrinsic background.

The presently running GERDA experiment [1] searching for $0\nu\beta\beta$ in ^{76}Ge uses, at the moment, 15 kilograms of enriched high-purity germanium detectors. The detectors are directly submerged in liquid argon which serves as cooling medium for the detectors and as shielding against surrounding radiation simultaneously. Such a design minimizes the background rate in the region of interest to a level never reached before. The 15 kg·yr of exposure during the first phase of the experiment will allow to confirm or disproof the claim that $0\nu\beta\beta$ was observed, which was made by part of the Heidelberg-Moscow collaboration [2].

Low levels of background are a necessary requirement to improve the sensitivity of experiments searching for $0\nu\beta\beta$. Deep underground locations and massive shielding of the detectors already reduce the unwanted background. Offline analyses of the time structure of the detector response, pulse shapes, can further reduce it by discriminating between

signal-like and background-like pulse shapes. Pulse shape analysis is also used in the analysis of the GERDA data.

The main goals of the work presented here were to study background sources and the usage of pulse shapes to identify background events, and to perform systematic studies of the dependence of the pulse shapes on environmental conditions and detector configurations. A significant part of the studies was performed using segmented high purity germanium detectors to evaluate their possible application in future experiments.

The thesis is structured as follows. Chapter 1 provides a current picture on neutrino physics with the focus on searches for neutrinoless double beta-decay. The concept of the GERDA experiment and the current status of data taking is summarized in Chapter 2. Basic principles of the operation of germanium detectors and their response to radiation are explained in Chapter 3.

Chapter 4 describes Monte Carlo simulations relevant for several background sources not considered previously for GERDA or future tonne-scale experiments.

The analysis of pulse shapes using artificial neural networks to identify background events is presented in Chapter 5. The influence of systematic effects on the performance of the method is also demonstrated.

Variations of the detector temperature lead to changes of the pulse shapes. In Chapter 6, the effect is discussed and the measured dependence of the pulse lengths on the temperature is presented and compared to model expectations.

Chapter 7 describes how the so called transverse anisotropy in germanium crystals affects the performance of detectors and how the effect can be used to determine the orientation of the crystallographic axes in segmented detectors using simulated pulse shapes.

The knowledge of the direction from which radiation reaches a detector helps to identify the origin of such unwanted background. Chapter 8 presents two methods to determine the origin of gamma radiation using Compton-backtracking. Such methods are only applicable in a granular detector array such as GERDA or a segmented detector. A novel method to determine the (x, y, z) coordinates of the origin of the radiation is proposed.

The last chapter summarizes the work presented in this thesis.

Chapter 1

Neutrinos

With the discovery of the electron by J.J.Thomson in 1897, a new era of physics – now called particle physics – started. For over hundred years, the theoretical model of particles, the Standard Model (SM) [of particle physics], has been enhanced and today it is very successful and well supported by a series of experiments, mostly accelerator-based.

In the Standard Model, the building blocks of matter consist of 12 fermions, six quarks and six leptons, all of them with spin $\frac{1}{2}$. There is one fermion species, neutrinos, about which is the known least. They are leptons, therefore do not take part in strong interactions, and have zero electric charge, hence no electromagnetic interactions. This makes neutrinos very hard to investigate with existing technologies. However, neutrinos are the obvious tool with which to explore weak processes. The history of neutrino physics and weak interactions are strongly connected.

With the discovery of neutrino oscillations, it became clear that neutrinos have a finite rest mass. The absolute mass of neutrinos could not be measured yet. The field of neutrino physics still holds a number of unanswered questions.

1.1 Historical overview

The history of neutrino physics began with the investigation of β-decay. In 1914 J. Chadwick discovered a continuous energy spectrum of electrons emitted in β-decay. W. Pauli explained this in 1929 by introducing an additional neutral spin $\frac{1}{2}$ particle which he called *neutron*. Later, in 1933, it was named *neutrino* by E. Fermi.

In 1952, an evidence for existence of neutrinos was found by measuring the recoil energy of ^{37}Ar in the electron capture (EC) reaction [3]

$$^{37}\mathrm{Ar} + \mathrm{e}^- \rightarrow ^{37}\mathrm{Cl} + \nu_e + Q.$$

The observation of the electron neutrino succeeded in 1953 [4] and was confirmed in 1956 [5], by F. Reines and C. L. Cowan. It is interesting to note that in 1955 R. Davis reported a negative result on the reaction $\bar{\nu}_e + ^{37}\mathrm{Cl} \rightarrow ^{37}\mathrm{Ar} + \mathrm{e}^-$ [6], therefore showing that there must be no right-handed weak currents, even before the neutrino was discovered. In 1957 B. Pontecorvo first assumed that neutrinos can oscillate in the same way as kaons

[7], if more than one generation of neutrinos existed. In 1962, the muon neutrino was discovered by the group of Lederman, Schwartz and Steinberger [8]. With the discovery of τ-lepton in 1975 by M. Perl [9], and finally the observation of the τ-neutrino in 2000 by the DONUT experiment at Fermilab [10], the observation of the lepton sector of the Standard Model was complete.

1.2 Neutrinos in the Standard Model and beyond

The lepton sector of the Standard Model (SM) is presented by the three charged leptons, electron, muon and τ lepton, and their partners, the neutrinos. Neutrinos are neutral particles. They only take part in the electroweak interactions described by the $\mathrm{SU}(2)_L \otimes \mathrm{U}(1)_Y$ gauge symmmetry. The first theory of weak interaction, 4 particle interaction by Fermi, was very successful at low energies but could not explain the data at higher energies and the observed parity violation. The introduction of vector gauge bosons, Z and $W^{\pm}$, and the assumption of V-A currents could explain these features and lead to the unification of electromagnetic and weak theories. In this framework, right-handed neutrinos can not take part in the electroweak interactions, which is denoted as $\mathrm{SU}(2)_L$. The lepton sector in the SM is therefore presented by the doublet ν_{lL}, l_L and the singlet l_R, with $l \in e, \mu, \tau$, i.e.

$$L_l \equiv \begin{pmatrix} \nu_{lL} \\ l_L \end{pmatrix}, l_R \quad l \in e, \mu, \tau, \tag{1.1}$$

plus antiparticles.

The mass term of particles in the Lagrangian has the form of $L = m\overline{\psi}\psi$. A possible neutrino mass term can be constructed using chiral projections of the neutrino field:

$$\mathcal{L}_\nu^D = -m_D \overline{\nu}\nu = -m_D \overline{(\nu_L + \nu_R)}(\nu_L + \nu_R) = -m_D \overline{\nu_R}\nu_L + h.c., \tag{1.2}$$

where m_D is denoted as the neutrino mass. The subscript D refers to the Dirac nature of neutrino mass as it is similar to other mass terms in the SM. The terms $-m_D\overline{\nu_L}\nu_L$ and $-m_D\overline{\nu_R}\nu_R$ vanish: $\overline{\nu_L}\nu_L = \overline{P_L\nu}P_L\nu = \overline{\nu}P_RP_L\nu = 0$ from the definition of the chiral projections P_L and P_R. In Eq. 1.2 the chirally left-handed neutrino field ν_L couple to the chirally right-handed one ν_R.

The absence of right-handed neutrinos seems to imply that neutrinos are massless. From the oscillation experiments, described in Section 1.3.2, it is, however, known that neutrinos have non vanishing masses. This requires both left- and right-handed neutrino interactions. In the Dirac case, neutrinos and anti-neutrinos are distinct particles and the lepton number is conserved in interactions. Since neutrinos are electrically neutral, it could also be possible that neutrinos and anti-neutrinos are the same particles, i.e. $\overline{\nu} = \nu$. In this case the neutrinos are said to be of Majorana type. In addition to the Dirac mass term a Majorana mass term appears in the Lagrangian:

$$\mathcal{L}_\nu^M = -m_M^R \overline{\nu_R^c}\nu_R - m_M^L \overline{\nu_L}\nu_L^c + h.c., \tag{1.3}$$

with two Majorana masses m_M^R and m_M^L. In this case the Lagrangian includes the coupling of the neutrino field to the anti-neutrino field. The existence of Majorana terms implies that the lepton number is not conserved during the interactions.

The inclusion of Majorana masses into the Lagrangian can explain why neutrino masses are so tiny through the see saw mechanism [11], according to which there is one light, $\sim 0.01\,\text{eV}$, and one heavy, $\sim 10^{15}\,\text{GeV}$, neutrino, in terms of the Majorana mass.

1.3 Neutrino oscillations

1.3.1 Neutrino flavour mixing

Introducing masses for electrically neutral neutrinos also implies that there can be mixing between different neutrino flavours as in the quark sector of the SM. It means that the flavour state of a neutrino, $\nu_\alpha, \alpha \in e, \mu, \tau$, is a linear combinations of the mass eigenstates, $\nu_j, j = 1, 2, 3$, with masses m_j:

$$\nu_\alpha = \sum_j U_{\alpha j} \nu_j, \tag{1.4}$$

where U is a unitary matrix – the neutrino mixing matrix [12, 13, 14, 15]. The matrix is usually referred as the Pontecorvo-Maki-Nakagawa-Sakata (PMNS) mixing matrix. Eq. 1.4 implies that the individual lepton charges, L_α, are not conserved. The full lepton charge, $L = L_e + L_\mu + L_\tau$ can, however, still be conserved.

The PMNS matrix, U, can parametrized by 3 angles, θ_{12}, θ_{13}, θ_{23}, and, depending on whether neutrinos are Dirac or Majorana particles, by 1, δ, or 3, δ, α_1, α_2, violation phases [16]:

$$U = \begin{pmatrix} 1 & 0 & 0 \\ 0 & c_{23} & s_{23} \\ 0 & -s_{23} & c_{23} \end{pmatrix} \begin{pmatrix} c_{13} & 0 & s_{13}e^{-i\delta} \\ 0 & 1 & 0 \\ -s_{13}e^{i\delta} & c_{13} & \end{pmatrix} \begin{pmatrix} c_{12} & s_{12} & 0 \\ -s_{12} & c_{12} & 0 \\ 0 & 0 & 1 \end{pmatrix} \begin{pmatrix} e^{i\alpha_1/2} & 0 & 0 \\ 0 & e^{i\alpha_2/2} & 0 \\ 0 & 0 & 1 \end{pmatrix} \tag{1.5}$$

where c_{ij} and s_{ij} are $\cos\theta_{ij}$ and $\sin\theta_{ij}$, respectively. The Majorana phases α_1 and α_2 can be different from zero only if neutrinos are of Majorana type. The physical consequences of this, in particular the possibility of neutrinoless double beta-decay, will be discussed in Section 1.5.

If only two-flavour mixing is considered (say, $\nu_e \leftrightarrow \nu_\mu$), then U becomes

$$\begin{pmatrix} \nu_e \\ \nu_\mu \end{pmatrix} = \begin{pmatrix} \cos\theta & \sin\theta \\ -\sin\theta & \cos\theta \end{pmatrix} \begin{pmatrix} \nu_1 \\ \nu_2 \end{pmatrix} \tag{1.6}$$

The neutrino mixing parameters are derived from neutrino transitions while moving in space, called neutrino oscillations. The development in time can be derived from the Schrödinger equation. Taking natural units of c and $\hbar$, $c = \hbar = 1$, after travelling a distance L, a neutrino of flavour α transforms into the state

$$|\nu_\beta(L)\rangle = U_{\beta j} |\nu_j(L)\rangle = U_{\beta j} e^{-i\left(m_j^2/2E\right)L} U_{\alpha j}^* |\nu_\alpha\rangle . \tag{1.7}$$

The transition probability of a neutrino with energy E at distance L can be derived as shown in [17, p. 191-192], [18, p. 189]:

$$P(\nu_\alpha \to \nu_\beta) = |\langle \nu_\alpha | \nu_\beta(L) \rangle|^2 = \sum_{jk} U^*_{\beta j} U_{\alpha j} U_{\beta k} U^*_{\alpha k} \exp\left(-i \Delta m^2_{jk} L/2E\right), \tag{1.8}$$

where $\Delta m^2_{ij} = m^2_i - m^2_j$. The same also implies for $P(\bar{\nu}_\alpha \to \bar{\nu}_\beta)$, with replacement of U by its complex conjugate. As seen from Eq. 1.8, the Majorana phases α_1, α_2 do not affect neutrino oscillations.

The general transition formulae in the 3-neutrino scenario are quite complex. In most cases only one mass scale is relevant, $\Delta m^2_{31} \approx \Delta m^2_{23} = \Delta m^2_{\text{atm}}$, where Δm^2_{atm} denotes the "atmospheric" mass scale, first measured with atmospheric neutrinos. The simplified formulae in 3-neutrino scenario for the transitions $\nu_e \leftrightarrow \nu_\mu, \nu_e \leftrightarrow \nu_\tau$ and $\nu_\mu \leftrightarrow \nu_\tau$ do not contain θ_{12} [17, Eq. 8.32–8.34]. This value is derived from 2-neutrino scenarios for $\nu_e \leftrightarrow \nu_\mu$, with the transition probability

$$P(\nu_e \to \nu_\mu) = P(\nu_\mu \to \nu_e) = P(\bar{\nu}_e \to \bar{\nu}_\mu) = P(\bar{\nu}_\mu \to \bar{\nu}_e) = \sin^2 2\theta_{12} \times \sin^2\left(\Delta m^2_{12} L \,/\, 4E\right). \tag{1.9}$$

The quantity Δm^2_{12} is often denoted as Δm^2_{sol}, where "sol" stands for the "solar" mass scale, first observed in solar neutrinos. Experimental results on neutrino mixing parameters are described in the following section.

1.3.2 Experimental approaches

Experimentally, the mixing parameters, along with the neutrino mass differences squared, are extracted from the measurements of the transition probability given in Eq. 1.8 which has an oscillating phase $\Delta m^2_{jk} \cdot L/E$. Several terms in Eq. 1.8 may vanish or become negligible by choosing the proper distance from the source to the detector. The other phases in the exponents may on the other hand become large enough. An experiment in this case is said to be sensitive to a particular oscillation component. The ratio L/E acts as an important sensitivity parameter of an experiment. The value of L/E is usually chosen to maximize the transition amplitude of interest, i.e. $L/E \simeq 1/\Delta m^2_{jk}$.

There are several usable sources of neutrinos with different continuous energy spectra. Depending on the parameter L/E, the same neutrino source may be used by several detectors to probe different transitions between neutrino species. Table 1.1 from the PDG [19] summarizes the neutrino sources and the locations of experiments to probe different neutrino oscillation parameters.

Solar neutrinos were historically the first test for neutrino oscillations. Neutrinos emitted from the sun are a direct probe of the fusion reactions that occur in the center of the sun. According to the Standard Solar Model (SSM) [20], the dominating reaction is the *pp* reaction: $p + p \to {}^2\text{H} + e^+ + \nu_e$. The emitted neutrinos have a continuous spectrum up to 0.42 MeV. Another important reaction, denoted as ^{8}B, is $^8\text{B} \to 2\,^4\text{He} + e^+ + \nu_e$ with the maximal neutrino energy of 14.06 MeV. Several experiments [21, 22, 23] reported the "neutrino puzzle" which consisted in the observation of neutrino events three times smaller

Source	Type of ν	$\overline{E}$ [MeV]	L [km]	L/E[km/MeV]	min(Δm^2)eV^2
Reactor	$\bar{\nu}_e$	~ 1	1	~ 1	$\sim 10^{-3}$
Reactor	$\bar{\nu}_e$	~ 1	100	~ 100	$\sim 10^{-5}$
Accelerator	ν_μ, $\bar{\nu}_\mu$	$\sim 10^3$	1	$\sim 10^{-3}$	~ 1
Accelerator	ν_μ, $\bar{\nu}_\mu$	$\sim 10^3$	10^3	~ 1	$\sim 10^{-3}$
Atmospheric	$\nu_{\mu,e}$, $\bar{\nu}_{\mu,e}$	$\sim 10^3$	10^4	~ 10	$\sim 10^{-4}$
Sun	ν_e	~ 1	1.5×10^8	$\sim 10^8$	$\sim 10^{-11}$

Table 1.1: Sensitivity of different oscillation experiments.

than expected. This was later explained by $\nu_e \to \nu_\mu$ transitions, i.e. electron neutrinos disappearance.

Atmospheric neutrinos arise from the decay of secondaries (predominantly π, K and μ), produced by primary cosmic ray interactions in the atmosphere. These neutrinos follow a continuous power low spectrum with much higher energies than solar neutrinos. At these energies, the dominating terms correspond to the transition $\nu_\mu \to \nu_\tau$ with the parameters Δm^2_{23} and $\theta_{\text{atm}} \approx \theta_{23}$.

Accelerator neutrinos are produced at proton accelerators. Charged pions that are produced by protons hitting a target, decay into muons, $\pi^{+(-)} \to \mu^{+(-)} + \bar{\nu}_\mu(\nu_\mu)$. The energy spectrum of accelerator neutrino beams expands to hundreds of MeV and higher, which opens the possibility to probe higher Δm^2, i.e. Δm^2_{atm} and smaller mixing angles via $\nu_\mu \to \nu_e$ and $\nu_\mu \to \nu_\tau$ transitions.

Neutrino beams from accelerators allow the usage of two detectors – a near detector, several hundred meters away from the neutrino source, and a far detector, several hundred kilometers away. The near detector acts as a precise counter of ν_μ that did not yet have time to oscillate, and the far detector either counts ν_e or ν_τ to measure the transitions, or counts ν_μ to analyze the muon neutrino disappearance.

Reactor neutrinos are constantly produced during the operation of nuclear reactors. Nuclear plants have played a crucial role in exploring the properties of neutrinos, from the first direct observation of the neutrino in 1956 to current neutrino oscillation experiments. Nuclear reactors are high intensity, isotropic sources of electron anti-neutrinos. Considering a typical thermal power of a reactor of 3 GW, there are about $6 \times 10^{20}\, \bar{\nu}_e/s$ produced. More than 99.9% of the anti-neutrinos result from four nuclei: ^{235}U, ^{238}U, ^{239}Pu and ^{241}Pu. The measured energy spectrum of the $\bar{\nu}_e$ peaks at about 2–3 MeV, with the maximum at about 8 MeV. These neutrino energies are too low to produce a muon or tau leptons in the detector. Therefore, only the electron neutrino disappearance is measured. Using the mean energy of 3.6 MeV, the baseline, L_{max}, for the oscillation maxima corresponding to the "solar" and "atmospheric" Δm^2 can be estimated from the transition probabilities:

$$\Delta m^2_{12} \sim 8 \times 10^{-5}\,\text{eV}^2 : \qquad L_{\text{max}} \sim 60\,\text{km} \tag{1.10}$$

$$\Delta m^2_{13} \sim 2.5 \times 10^{-3}\,\text{eV}^2 : \qquad L_{\text{max}} \sim 1.8\,\text{km} \tag{1.11}$$

According to these two values, experiments on reactor neutrinos can be divided into two groups:

1. Long-baseline experiments. Used to explore the region of $\Delta m^2 \approx 10^{-5}\,\mathrm{eV}^2$ and large mixing angle. Typical distance of the baseline is $\mathcal{O}(100)\,\mathrm{km}$.
2. Short-baseline experiments. Used to search for $\Delta m^2 \approx 10^{-2}$–$10^{-3}\,\mathrm{eV}^2$ region. Typical distance between a reactor and the detector is not more than 1 km.

The current state of the art gives the values and limits on the oscillation parameters listed in Table 1.2.

Parameter	Value(limit)
$\sin^2 2\theta_{12}$	0.87 ± 0.03
$\sin^2 2\theta_{23}$	> 0.92
$\sin^2 2\theta_{13}$	$< 0.19, 90\%\,\mathrm{CL},\ 0.092 \pm 0.016 \pm 0.005$ [24]
Δm^2_{21}	$(7.59 \pm 0.20) \times 10^{-5}\,\mathrm{eV}^2$
$\lvert\Delta m^2_{32}\rvert$	$(2.43 \pm 0.13) \times 10^{-3}\,\mathrm{eV}^2$

Table 1.2: Best values and limits on the neutrino oscillation parameters [19, 25]. The value of $\sin^2 2\theta_{13}$ was recently measured by the Daya Bay collaboration and also listed.

Neutrino oscillation experiments can only measure the mixing parameters and the mass-squared differences. It is also known from the solar neutrino experiments that the value of Δm^2_{21} is positive due to the MSW effect [26] in the sun. The sign of Δm^2_{32} is, however, not known and allows two possible neutrino mass hierarchies, *normal* and *inverted*, depicted in Fig. 1.1. The hierarchy cannot be resolved from the oscillation experiments as the absolute masses do not enter the transition probability formulae and the sign of Δm_{32} cannot be extracted.

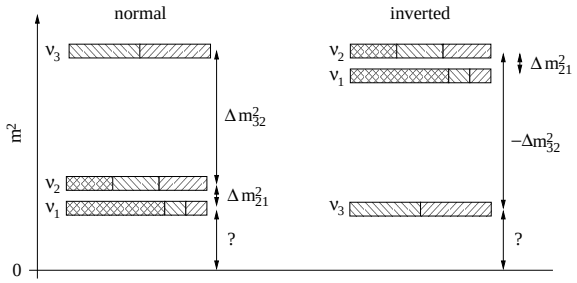

Figure 1.1: Normal and inverted hierarchy of the neutrino masses.

1.4 Measurements of neutrino masses

The observation of neutrino oscillations [27] has been an indirect proof of finite neutrino rest-masses. The measured values of Δm^2_{ij} are small. The measurement of an upper

limit on one neutrino species automatically also implies upper limits on the others. Measurements of neutrino masses have been a challenge that people have tackled ever since the neutrino was discovered. As the lowest upper limit can experimentally be obtained for the electron neutrino, the definition of the neutrino mass scale is strongly connected to the measurement of the electron neutrino mass.

Direct determination. A direct method to determine the effective electron neutrino mass uses beta-decay. In this process a neutron in a nucleus decays into a proton with the emission of an electron and an anti-neutrino. The electron energy is not constant as the neutrino carries away part of the energy.

The typical shape of the spectrum is shown in Fig. 1.2. The endpoint energy, E_0, corresponds to the energy released in the decay, the Q-value, Q_β. Neglecting the recoil energy of a nuclei in a beta-decay, they equal, $E_0 = Q_\beta$. For a non-zero neutrino mass, the spectra will have a different, smaller, endpoint of the spectrum, shifted to lower energies. The lack of events in the region at the unshifted endpoint is used to extract the neutrino mass. Experimentally it is preferred to have as low E_0 as possible. The number of events of interest below the unshifted endpoint compared to the total number of events is larger for smaller E_0. Tritium is the most suitable isotope for the mass determination; it has Q_β of 18.6 keV and relatively short half life of 12.3 y. However, even in this case, the lack of events in the region $E_0 - m_\nu c^2$ to E_0 (as shown in Fig. 1.2(b) with filled area) for $m_\nu = 1\,\text{eV}$ is only 10^{-13} of the total sum of the spectra.

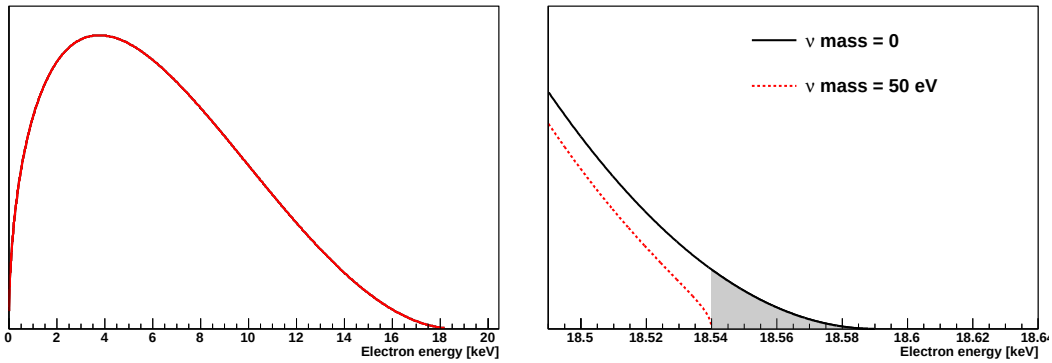

(a) (b)

Figure 1.2: (a) Distribution of the kinetic electron energy from beta-decay of ^{3}H and (b) zoomed region around $E_0 = 18.59\,\text{keV}$.

The neutrinos emitted in a beta-decay are flavour states. Therefore, the measured effective electron neutrino mass is a superposition of mass eigenstates using the matrix in Eq. 1.5. The measured value is $m^2_{\nu_e} = \sum_i |U_{ei}|^2 m^2_{\nu_i}$. The Majorana phases do not contribute to m_ν. Therefore, the nature of the neutrinos, whether Dirac or Majorana, cannot be distinguished in single beta-decay experiments.

The two most accurate results were reported by the Mainz and Troitsk neutrino experiments. The limits were set to $m(\nu_e) < 2.3\,\text{eV}$ [28] and $m(\nu_e) < 2.05\,\text{eV}$ [29], respectively.

The future spectrometer experiment KATRIN [30] is designed to improve the sensitivity to the sub-eV mass range.

A relatively new approach uses cryogenic bolometers with microcalorimeters. In this method, the ^{187}Re isotope with the lowest known Q_β, 2.5 keV, is used in cryogenic $AgReO_4$ bolometers cooled down to mK temperatures. The same idea to analyze the endpoint of the β-spectrum is used here. The difference is that the source is "integrated" in the detector. The current upper limit on the mass determined with this method is relatively high. It was set in 2004 [31], $m(\nu_e) < 15$ eV. The future project MARE [32] is projected to have a sub-eV sensitivity on the neutrino mass.

The mass of the muon neutrino can be extracted from measurements of pion decays, $\pi^+ \to \mu^+ + \nu_\mu$. For pion at rest, the mass of the neutrino is simply

$$m^2_{\nu_\mu} = m^2_\pi + m^2_\mu - 2m_\pi\sqrt{p^2_\mu + m^2_\mu}. \tag{1.12}$$

The experiment [33] conducted in 1996 reported a limit on the muon neutrino mass of $m(\nu_\mu) < 190$ keV (90% CL).

The tau neutrino mass can be evaluated using the same method from the $\tau^- \to \nu_\tau + (n\pi)^-$ decay with different combinations of charged and neutral pions, denoted as $(n\pi)^-$. The best limit was set by ALEPH, $m(\nu_\tau) < 18.2$ MeV [34].

Cosmological considerations allow the **Indirect determination** of upper limits on the neutrino mass. The most model independent limits come from the observed matter content and structure formation. These limits are around 1 eV. Some models (e.g. reported in [35]) suggest individual neutrino mass limits of $m_i \lesssim 0.1$ eV.

Another indirect probe of neutrino mass is neutrinoless double beta-decay which will be described in more detail in the following section.

The mass values extracted with different methods cannot be directly compared. The measured quantities have different origin. The values from cosmology are given for the mass eigenstates, m_i; the results from tritium experiments give the effective mass, m_β, which is a real combination of all the mass eigenstates. The value derived from the neutrinoless double beta-decay is the effective Majorana mass, $m_{\beta\beta}$, which is a coherent sum that includes also the CP-violating phases.

1.5 Double beta-decay

In a double beta-decay two neutrons in a nucleus coherently decay emitting two electrons and two anti-neutrinos. Double beta-decay is a much more rare transition that single beta-decay. To observe it, single beta-decay should be forbidden or at least strongly suppressed. The beta-decay of an even-even nuclei (Z, A) may be forbidden if the neighboring nuclei (Z±1, A) has a higher binding energy due to pairing energy difference. Apparently, this cannot happen for even-odd or odd-even nuclei. The isotope ^{76}Ge is an example. The binding energies of the isobar nuclei with $A = 76$ are shown in Fig. 1.3. The decay ^{76}Ge→^{76}As is energetically forbidden, however the decay ^{76}Ge→^{76}Se is allowed.

The suppression of single beta-decay can also happen if the transition occurs between states with a large difference in angular momenta of the nuclei (for example, ΔL =5 or 6

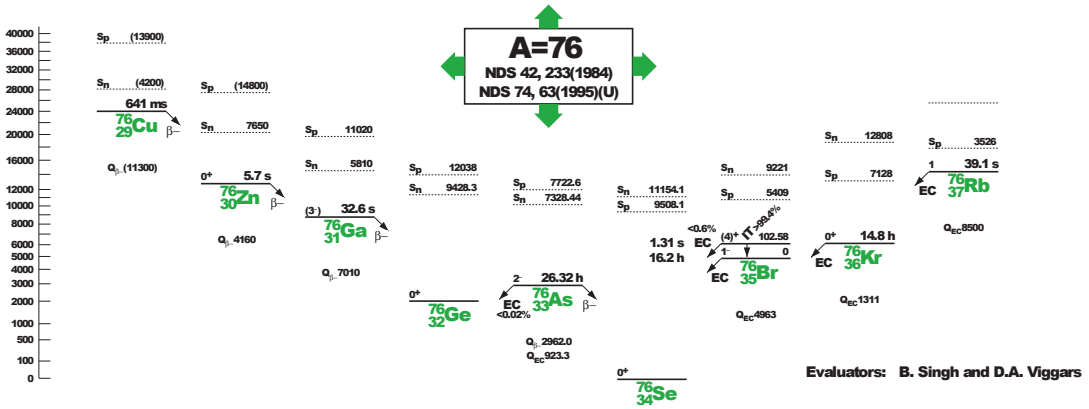

Figure 1.3: Energy levels for isobars with $A = 76$ taken from [36]. The single transition ${}^{76}_{32}\mathrm{Ge}\rightarrow{}^{76}_{33}\mathrm{As}$ is forbidden, but the double beta-decay ${}^{76}_{32}\mathrm{Ge}\rightarrow{}^{76}_{34}\mathrm{Se}$ is allowed.

for ${}^{48}\mathrm{Ca}$).

Two modes of double beta-decay usually considered are:

$$(Z, A) \rightarrow (Z + 2, A) + 2e^- + 2\bar{\nu}_e \qquad (2\nu\beta\beta), \tag{1.13}$$

$$(Z, A) \rightarrow (Z + 2, A) + 2e^- \qquad (0\nu\beta\beta). \tag{1.14}$$

In the case of the **neutrino-accompanied double beta-decay**, see Fig. 1.4(a), two electrons are emitted together with two neutrinos. This is a second order weak process in the Standard Model. Therefore, the half life of double beta-decay is much higher than for single beta-decay. The rate of the $2\nu\beta\beta$ process does neither depend on neutrino masses nor on any mixing [37]. Therefore, the decay is allowed irrespectively whether neutrinos are of Majorana or Dirac nature. It has been measured for 10 isotopes [38]. Some values are listed in Table 1.3. The half lives are of the order of $10^{20\pm2}$y.

Transition	$Q_{\beta\beta}$ [keV]	$T^{2\nu\beta\beta}_{1/2}$ [10^{20}y]
${}^{76}\mathrm{Ge} \rightarrow {}^{76}\mathrm{Se}$	2039	15
${}^{100}\mathrm{Mo} \rightarrow {}^{100}\mathrm{Ru}$	3034	0.071
${}^{116}\mathrm{Cd} \rightarrow {}^{116}\mathrm{Sn}$	2802	0.28
${}^{150}\mathrm{Nd} \rightarrow {}^{150}\mathrm{Sm}$	3367	0.082

Table 1.3: Examples of $2\nu\beta\beta$ candidates and the experimental results for half-lives.

In the neutrino-accompanied mode, two neutrinos carry away part of the energy released in the decay. As a result, the sum of the energies of the two electrons, neglecting the nuclear recoil energy, is a continuous function up to the Q-value of double beta-decay, $Q_{\beta\beta}$. The

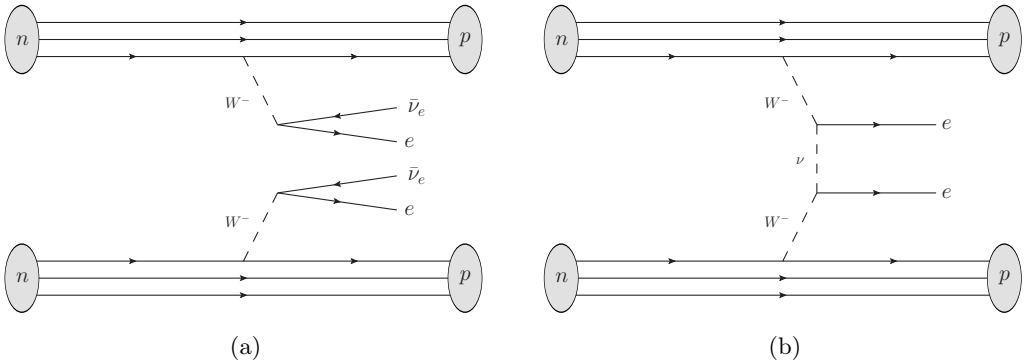

Figure 1.4: Feynman diagrams for double beta-decays. a) Neutrino-accompanied double beta-decay. The lepton number is conserved. b) Neutrino-less double beta-decay. A Majorana neutrino is exchanged violating the lepton number conservation.

energy distribution, dN/dE, can be approximated using the formula in [17, Ch. 7.2]:

$$\frac{dN}{dE} \approx E\,(Q_{\beta\beta} - E)^5 \left(1 + 2E + 4E^2/3 + E^3/3 + E^4/30\right) \tag{1.15}$$

with the maximum around $Q_{\beta\beta}/3$, see hatched area in Fig. 1.5.

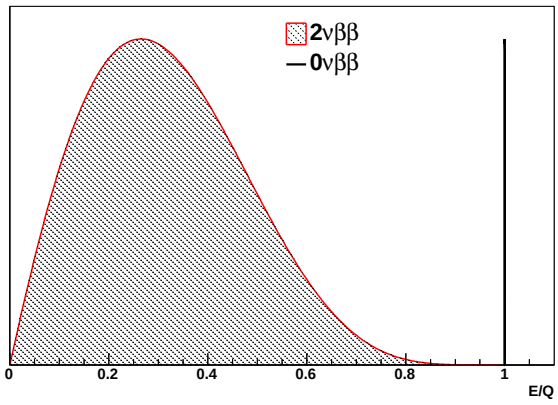

Figure 1.5: The distribution of summed electron energies for $0\nu\beta\beta$ and $2\nu\beta\beta$.

In **neutrino-less double beta-decay**, see Fig. 1.4(b), a right-handed anti-neutrino emitted by one neutron is absorbed in the second as a left-handed neutrino, thus a helicity flip needs to occur. The lepton number is violated by two units. The process is not allowed in the Standard Model. Therefore it is of high interest as a search for new physics. Its half life is expected to be even larger than that of $2\nu\beta\beta$. However, neutrinoless double beta-decay has not been observed up to now. The best limits on $0\nu\beta\beta$ half lives are well above 10^{21}y.

In the neutrino-less mode, the summed energy of the two electrons is almost equal to $Q_{\beta\beta}$ itself, ignoring the recoil energy of the nucleus which is negligible compared to the

electron energies, see Fig. 1.5.

The rate of $0\nu\beta\beta$ can be described with the most common assumption of a virtual light Majorana neutrino exchange [37] being responsible for the helicity flip:

$$\left(T^{0\nu}_{1/2}\right)^{-1} = G_{0\nu}(Q_{\beta\beta}, Z) \cdot |M_{0\nu}|^2 \cdot \langle m_{\beta\beta}\rangle^2 \propto Q^5, \tag{1.16}$$

where $G_{0\nu}(Q_{\beta\beta}, Z)$ is the phase-space factor, $M_{0\nu}$ is the Nuclear Matrix Element (NME) and $\langle m_{\beta\beta}\rangle^2$ is the effective Majorana neutrino mass which contains also the Majorana CP violating phases,

$$\langle m_{\beta\beta}\rangle = \left|\sum_i m_i U^2_{ei}\right|. \tag{1.17}$$

While the phase space factors can be calculated precisely, the NME are less well understood. Unfortunately, the NME cannot be measured from other experiments. Theoretical models are listed in e.g. [39]. The uncertainty on the NME is of the order of a factor of 2. This directly defines the precision of the probed neutrino mass. Taking the neutrino mass of $\langle m_{\beta\beta}\rangle = 50\,\text{meV}$, the half-lives are estimated to be of the order of 10^{26}–10^{27} y [39], depending on the isotope and matrix elements.

1.5.1 Experimental considerations

A direct way to measure the $0\nu\beta\beta$ half-lives, $T^{0\nu}_{1/2}$, is pursued in **counting** experiments. As was mentioned before in this section, the summed energy of the two electrons emitted in $0\nu\beta\beta$ equals $Q_{\beta\beta}$. In an experiment, the number of events, N, under this peak is counted. The effective neutrino mass can be extracted using Eq. 1.16 once the half life $T^{0\nu}_{1/2}$ has been measured.

The value of N is related to $T^{0\nu}_{1/2}$ as

$$N = \log 2 \cdot \frac{N_A}{W} \cdot \epsilon \cdot \frac{Mt}{T^{0\nu}_{1/2}}, \tag{1.18}$$

where M and W are the total mass and the atomic weight of the isotope, respectively, t is the data taking time, N_A is Avogadro's constant and ϵ is the detection efficiency. The terms in Eq. 1.18 and Eq. 1.16 suggest several requirements to be met in an experiment in order to get a good sensitivity. The exposure Mt has to be large. This means that $0\nu\beta\beta$ experiments usually run over several years. To increase the mass, the isotope under study should have high abundance in the used material, either naturally or by enrichment.

An important issue for all $0\nu\beta\beta$ experiments with small number of expected events is the presence of background. The quantitative parameter to describe it is the Background Index (BI), calculated as

$$\text{BI} = \frac{N_B}{Mt\Delta E}, \tag{1.19}$$

where N_B is the number of background events in the energy window ΔE around $Q_{\beta\beta}$, called Region Of Interest (ROI) [1]. Let's imagine an ideal experiment with BI=0. If the experiment measures no events, $N = 0$, the upper limit on the neutrino mass can be set from combining Eqs. 1.16 and 1.18 [39]:

$$\langle m_{\beta\beta} \rangle \leq K_1 \sqrt{\frac{A}{\epsilon M t}}, \tag{1.20}$$

where K_1 is the isotope-specific constant and $A = 2.3(3)$ for a 90%(95%) CL. The limit improves as $(Mt)^{-1/2}$. In a real experiment, BI$\neq$ 0. The Bayesian approach for the limit calculation [40] demonstrates the worsening of the dependence on the exposure. In the case of the large background approximation [39], when the number of signal events is less than the standard fluctuation expected for background, the dependence becomes

$$\langle m_{\beta\beta} \rangle \leq K_2 \sqrt{1/\epsilon} \left(\frac{c \Delta E}{Mt} \right)^{1/4}, \tag{1.21}$$

where K_2 is an another isotope-specific constant and c is the background counting rate. In this case the mass limit improves only as $(Mt)^{-1/4}$. Figure 1.6 demonstrates the dependence of the possible limits on BI.

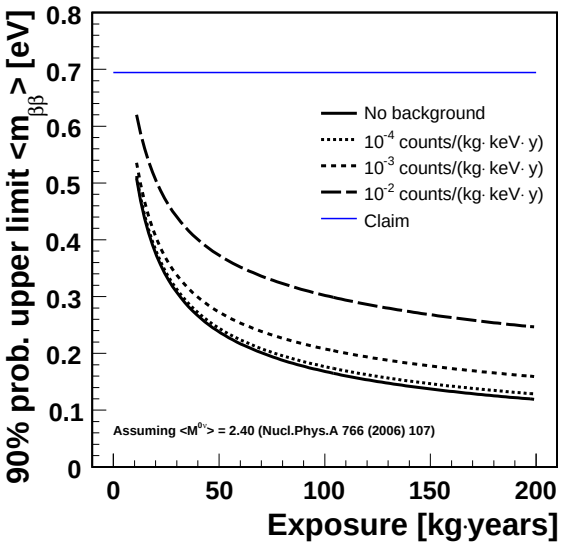

Figure 1.6: The expected 90% probability upper limit on the effective Majorana neutrino mass versus the exposure for different values of BI, adopted from [40]. The effective Majorana neutrino mass for the claimed observation [2] is also shown.

The sources of background are different from one experimental site to another, but the ways to shield against it are common. The main sources of background and their common mitigation strategies are as follows:

[1] The energy window is chosen depending on the energy resolution of a detector

- **Gammas** from radioactive decays in the experimental hall. Gammas originating from the isotopes produced in the uranium and thorium decay chains are usually the main contributors to the gamma background. The flux of gammas can be significantly suppressed by large amount of passive shielding like lead, water, copper, argon, etc. Lead bricks, however, are also radioactive, giving an additional intrinsic to the shield flux of gammas. Sometimes significantly less radioactive lead from old sunken roman ships is used. It is several hundred or thousand years old and due to a short life-time of contained isotopes, its radioactivity significantly decreased. The flux of gammas in an experiment cannot be reduced to zero as all materials have traces of primordial contamination with isotopes like U and Th and their decay products. Special care has to be taken in the production and the cleaning of the parts of an experiment, especially for parts like detector holders, cables, etc., which are close to the detectors.

- **Radon** can be produced as the decay product of U and Th. It is a noble gas and can penetrate large distances without being absorbed. It is hard to avoid the "traveling" of radioactive radon ions, therefore a special care has to be taken in the production and the cleaning of the parts of an experiment. Radon can also reach the detector by convention in gas or liquid that is used in the experiment, therefore it is also important to take care during the operation of an experiment to avoid it.

- **Betas** and **Alphas** are mostly produced during decays in U and Th decay chains. Since both electrons and alphas do not penetrate material deeply, only contributions very close to a detector surface are relevant. The experiment-specific background requirements put limits on the allowed contamination of materials that are used in, e.g. detector metalization and passivation, and close to the detector.

- **Muons** from cosmic ray showers can be suppressed by locating an experiment deep under ground. Muon-induced events can also be tagged by using e.g. a water Cherenkov veto. This does not reduce the flux but acts as *active shielding*.

- **Neutrons** from natural radioactivity mostly are produced in the U and Th decay chain. Such decays occur everywhere around an experiment. Neutrons coming from rocks and soil can be suppressed by *passive shielding* by placing large amount of concrete or water around an experiment. Also materials like polyethylene and borated water are good materials to screen against neutrons.

Another requirement to be met in order to get high event rate is the value of $Q_{\beta\beta}$. According to Eq. 1.16, the event rate is proportional to $Q^5_{\beta\beta}$. Therefore, the preferred isotopes to search for $0\nu\beta\beta$ would be ^{48}Ca, ^{150}Nd, ^{82}Se, ^{130}Te or even ^{136}Xe, for which $Q_{\beta\beta}$ are 4271, 3368, 2996, 2528 and 2458 keV, respectively. Moreover, for higher Q-values, the gamma background, like from the 2.6 MeV gammas from ^{208}Tl, becomes less significant. However, ^{76}Ge with $Q_{\beta\beta}$ of 2039 keV is also widely used due to a very good intrinsic cleanliness and energy resolution of high-purity Ge-detectors of less than 0.2 % at $Q_{\beta\beta}$.

Apart from requirements on the isotope, experiments searching for $0\nu\beta\beta$ use one of two general approaches for the source and detector configuration:

1. Source ≠ detector. In this case thin source foils are stacked between detectors. Many isotopes were investigated with this method in e.g. NEMO 3 experiment [41].

2. Source = detector. In the experiments of this kind, the detector contains the $\beta\beta$-emitting isotope. It can be either a scintillator (^{48}Ca in CaF_2 crystals, ^{116}Cd in $CdWO_4$, ^{160}Gd in Gd_2SiO_5:Ce crystals), a semiconductor detector (^{76}Ge, ^{116}Cd, ^{130}Te), or liquid and gas Time Projection Chambers (TPC) (^{136}Xe).

The advantage of having detector and the source identical is that the electrons and the recoiling nuclei emitted in the double beta-decay get fully absorbed in the detector with high efficiency. This also adds a possibility to distinguish background-like events, in which energy deposits are non-localized from localized double beta-decay events.

In the "source≠detector" method, the main advantage is that the source can be exchanged and several isotopes can be tested. Additionally, the electrons can usually be tracked to better understand the event topology. A good background rejection efficiency is reachable. But generally the energy resolution is worse and the source has to be made in thin foils to let the electrons escape from the material volume.

1.5.2 Experiments for $0\nu\beta\beta$ search in ^{76}Ge

High purity germanium, HPGe, detectors are a sensitive tool for the search of $0\nu\beta\beta$. Usually the "source = detector" approach is used which maximizes the efficiency to register a $0\nu\beta\beta$ event, and, as was already mentioned, Ge-detectors have a very good energy resolution and intrinsic cleanliness. The natural abundance of ^{76}Ge is only 7.6 % [42]. This is why germanium detectors of the current generation of experiments are produced from *enriched* material with up to 88% enrichment in ^{76}Ge.

The most sensitive experiments of the past were the IGEX experiment in the Canfranc Underground Laboratory and the Heidelberg-Moscow (HdM) experiment in the Gran-Sasso Underground Laboratory, both operating with enriched detectors. The IGEX experiment set a limit on the life time, $T^{0\nu}_{1/2} > 1.6 \cdot 10^{25}$ yr, and the neutrino mass, $\langle m_\nu \rangle < 0.3(1.3)$ eV [43], depending on the model for the matrix elements calculation. Parts of the HdM experiment claimed the discovery of $0\nu\beta\beta$ with $T^{0\nu}_{1/2} = 1.2(1.8) \cdot 10^{25}$ yr [44] ([45]). Earlier publications presented a lower limit $T^{0\nu}_{1/2} > 1.6(1.9) \cdot 10^{25}$ yr and $\langle m_\nu \rangle < 0.38(0.35)$ eV [46]([47]). The final spectra for both experiments are shown in Fig. 1.7.

Table 1.4 lists the main parameters of the $0\nu\beta\beta$ experiments using HPGe detectors.

The presently running experiment GERDA started its operation in 2010. The physics runs started in 2011 with detector mass (mass of ^{76}Ge) of 25(16) kg. The detailed description of the experiment will be discussed in Chapter 2.

There is a series of experiments planned for searches in other $0\nu\beta\beta$-decaying isotopes. An overview is given in e.g. [39] and [48].

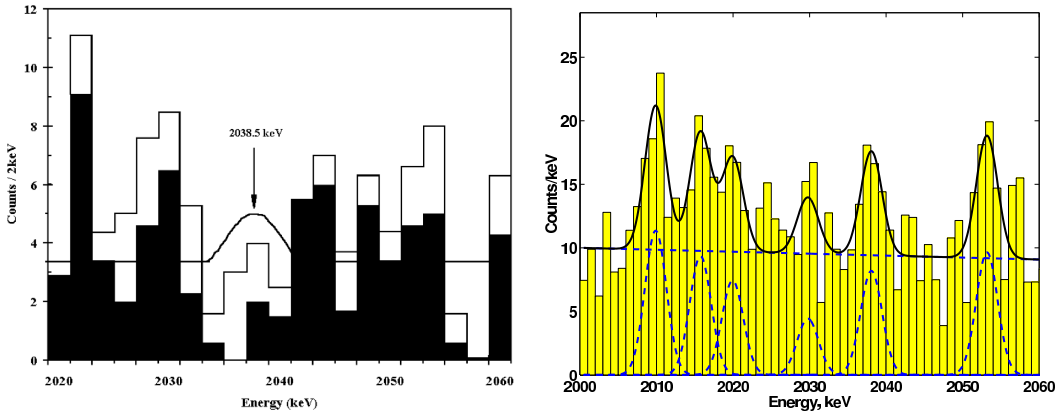

(a) IGEX (b) HdM

Figure 1.7: The spectra from the IGEX and HdM experiments around the Q-value.

Experiment	Running period	Detector mass	Exposure		BI
		[kg]	[kg·yr]	[mol·yr]	$[\frac{\text{cts}}{\text{kg·yr}\cdot\text{keV}}]$
IGEX	1991–2000	6	8.8	117	0.17 [43]
HdM	1990–2003	11	71.7	810	0.11 [2]
GERDA Phase I	started 2011	25	~ 25	-	$2 \cdot 10^{-2}$
GERDA Phase II	planned	$\sim$40	-	-	10^{-3}

Table 1.4: Parameters of the $0\nu\beta\beta$ experiments with ^{76}Ge.

Chapter 2

The GERDA experiment

The GERmanium Detector Array (GERDA) experiment is designed to search for neutrinoless double beta-decay in ^{76}Ge. Its main design feature is to operate "naked" high purity germanium detectors submerged in liquid argon. The GERDA experiment was proposed in 2004 [1]. Its construction was finished in 2010 and first data from non-enriched detectors were collected in 2010. Data taking with the full set of available enriched HPGe detectors was started in November 2011.

The experiment will run in two phases, with different target mass of germanium and different envisaged background levels. In the first phase, started in November 2011, the 18 kg of enriched detectors from the Heidelberg-Moscow [46, 47, 2, 44] and IGEX [43] experiments are used. Assuming a total exposure of 15 kg·yr and the designed level of background of 0.01 cts/(kg·yr·keV), the possible claim for observation of neutrinoless double beta-decay by part of the Heidelberg-Moscow collaboration [44] can be confirmed or refuted with 90 % C.L. within one year of data taking. Phase II is scheduled to start in 2013, with up to 20 kg of additional enriched detectors that are currently being produced. Taking the total exposure of 100 kg·yr and the designed background level of 0.001 cts/(kg·yr·keV), an upper limit of 0.2 eV of neutrino mass is achievable with 90 %C.L. [40].

2.1 Location and apparatus

The GERDA experiment is located in Hall A of the Laboratori Nazionale del Gran Sasso (LNGS) (see Figs. 2.1 and 2.2). Rocks corresponding to at least 3400 meter of water equivalent (m.w.e.) shielding power surround the experimental hall from all sides and shield against cosmic rays, reducing the flux of muons by six orders of magnitude compared to the flux at the surface.

"Naked" high purity germanium, HPGe, detectors, enriched in the isotope ^{76}Ge to ∼86 %, are submerged in Liquid Argon (LAr). The LAr acts as cooling medium and shielding against external radiation simultaneously. The detectors inside 65 m^3 of LAr, corresponding to 98 t, are contained in a low activity stainless steel cryostat with 4.16 m diameter and 5.88 m height (7.62 m with the neck). A layer of high purity copper covers the inner cryostat wall to shield radiation due to this wall. The design of having "naked"

Figure 2.1: Location of the GERDA experiment at LNGS laboratory.

detectors, i.e. not installed in a conventional vacuum cryostat, provides the possibility to reach a significantly lower level of background with respect to earlier experiments using vacuum cryostats. The operational temperature of the detectors in GERDA is provided by the LAr, avoiding the need for extra material for a vacuum cryostat which may have radioactive contamination.

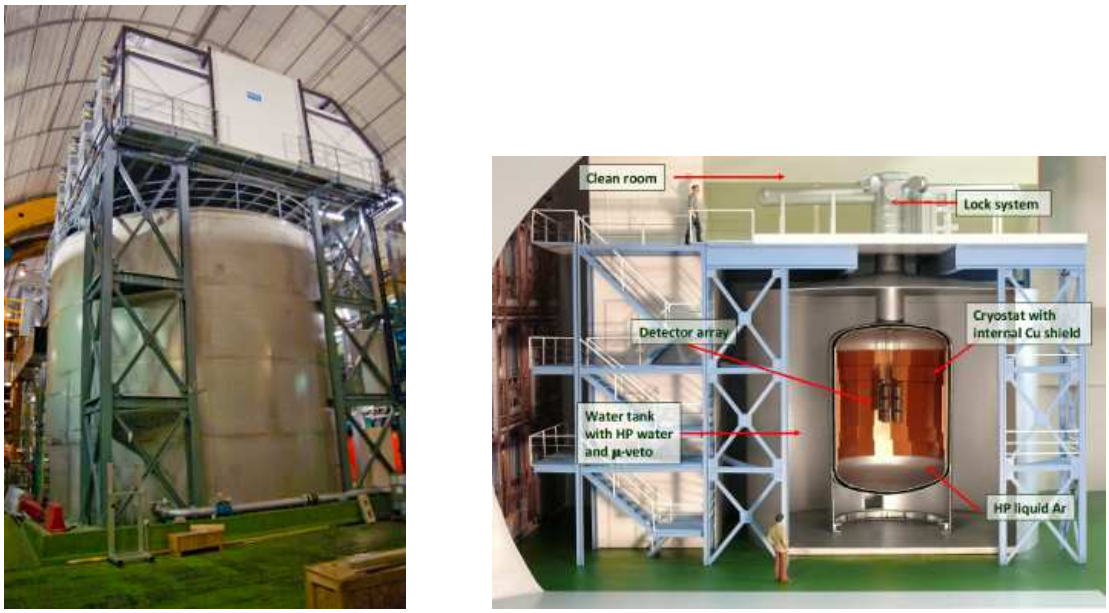

Figure 2.2: The experiment as mounted at LNGS and its schematic view. The main parts as discussed in the text are indicated.

The cryostat is mounted inside a water tank with an outer diameter of 10 m and a height of about 9 m [49]. The tank is filled with 630 m^3 of ultra-pure water to moderate and reduce the flux of neutrons coming mostly from natural radioactivity from the rocks surrounding the laboratory.

Liquid argon can be produced with a very high radio purity [50] and does therefore not introduce significant amount of background The LAr also acts as a shielding against gammas that come from the surrounding, the infrastructure and the water tank. In addition, liquid argon scintillates at 128 nm. It has been shown that this scintillation light can be used to veto background events [51, 52]. This feature will be exploited for the second phase of the experiment.

The detector integration happens in a cleanroom, class 10 000, located on top of the water tank. The detectors are lowered by a mechanism mounted inside a vacuum-tight lock that is inside the cleanroom. The detectors are mounted on two strings that can be lowered into the cryostat. Each string can support several detectors. The read-out electronics includes the first pre-amplifier stage, the cold FETs installed close to the crystals, ∼30 cm above the uppermost detectors. The main amplifying circuits are at room temperature.

To further reduce the muon background a muon veto containing 66 photo-multipliers was installed in the water tank [53] to detect Cherenkov light produced by muons while passing through the water. Additionally, seven plastic scintillator panels with dimensions of $(220 \times 50 \times 3)\,cm^3$ [53] are installed on top of the cryostat. Signals coincident in detectors and the muon veto can be considered as background. The muon veto has a rejection efficiency of better than 99 % as estimated from Monte Carlo simulation [54].

2.2 Detectors and run configurations

There are several non-enriched GTF (Genius Test Facility) [55] detectors available to test the performance of GERDA at different data taking periods, ***Runs***. Their characteristics are, however, not the focus of the present work. An overview of the enriched detectors available for GERDA is given in Table 2.1. The indicated resolutions were extracted from one of the calibration measurements shown in Fig. 2.3 taken with a ^{228}Th calibration source during ***Run 30***. All of the detectors are closed-end p-type HPGe detectors. The detectors ANG1 and RG3 started to draw high leakage current during data taking and are not considered for further analysis.

	ANG1	ANG2	ANG3	ANG4	ANG5	RG1	RG2	RG3
Total mass [g]	958	2833	2391	2375	2746	2113	2168	2087
Resolution [keV]	–	4.7	4.7	4.4	4.4	4.6	5.3	–

Table 2.1: Enriched detectors deployed in GERDA. ANG1 and RG3 detectors are not considered as they are most probably not usable due to high leakage current.

The commissioning measurements in GERDA started in July 2009 with three non-enriched GTF detectors with a total mass of 7.6 kg. In further tests, started in June 2010,

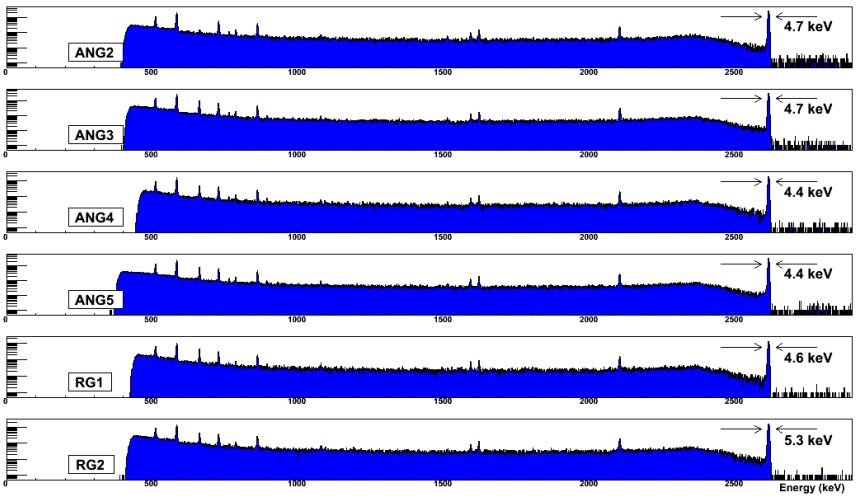

Figure 2.3: Calibration data taken during ***Run 30***. Also indicated are the full width at half maximum at 2.6 MeV. Adopted from Ref. [56]

three enriched detectors were added. The full set of eight enriched detectors together with three non-enriched detectors was installed in November 2011 to start physics data taking.

Configurations of detectors in different ***Runs*** and the corresponding channel mapping as recorded by the DAQ, as of Spring 2012, are listed in Tables 2.2 and 2.3 [57].

Run number	1-7	8-9	10-13
Starting date	Jul 2010	Nov 2010	Dec 2010
Chan. 0	GTF45	GTF45	GTF45
Chan. 1	GTF32	GTF32	GTF32
Chan. 2	GTF112	BEGe	GTF112

Table 2.2: GERDA run configurations with non-enriched detectors. Channel number corresponds to the channel ID mapping in the DAQ.

2.3 First results and current status

The first commissioning background data, see Fig. 2.4, revealed an unexpected full absorption peak at 1525 keV [58]. This was studied by the GERDA collaboration in detail. The line originates from the consequent decays ^{42}Ar$\rightarrow^{42}$K$\rightarrow^{42}$Ca. The beta-decay ^{42}K$\rightarrow^{42}$Ca, shown schematically in Fig. 2.5(a), has a maximal electron energy of 3525 keV and is with $\approx 18\,\%$ probability accompanied by the emission of a photon with an energy of 1525 keV. If ^{42}K decays occur close to the detector surfaces, the energy of the electrons can be high enough to contribute significantly to the background around the $0\nu\beta\beta$ Q-value, 2039 keV. This background contribution thus needs to be reduced. In order to mitigate the ^{42}Ar background, a copper shroud was installed around the detectors [58]. High voltage

Run number Starting date	14-15 Jun 2011	16-19 Jul 2011	20-22 Aug 2011	23 Oct 2011	24-31 and on Nov 2011
Chan. 0	RG1	RG1	RG1	GTF45	ANG1
Chan. 1	ANG4	ANG4	ANG4	GTF32	ANG2
Chan. 2	RG2	RG2	RG2	GTF112	ANG3
Chan. 3		GTF32	GTF32	GTF110	ANG4
Chan. 4		GTF45	GTF45	GTF42	ANG5
Chan. 5		GTF112	GTF112	empty	RG1
Chan. 6		GTF110			RG2
Chan. 7					RG3
Chan. 8					GTF112
Chan. 9					GTF45
Chan. 10					GTF32

Table 2.3: (contd.) GERDA run configurations with enriched detectors. Channel number corresponds to the channel ID mapping in the DAQ.

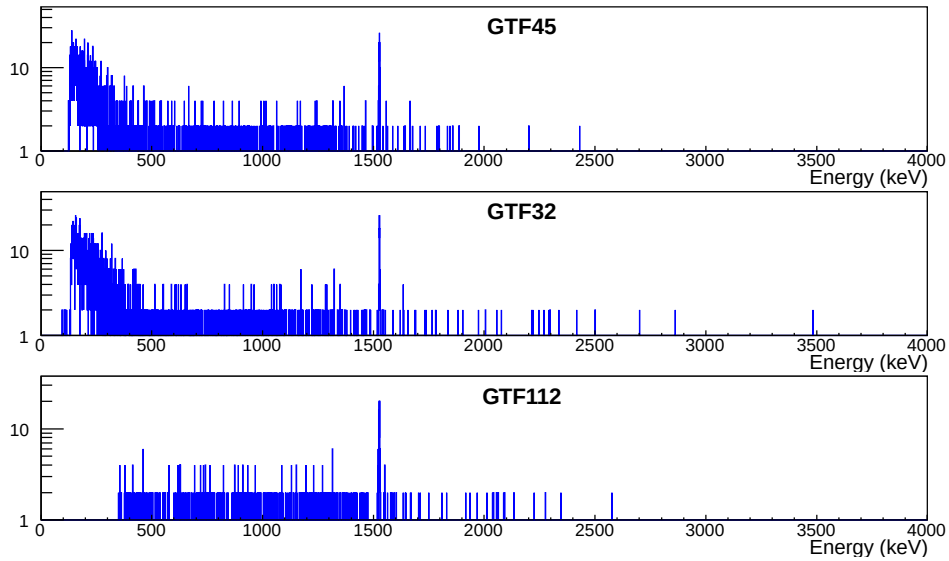

Figure 2.4: First data from ***Run 1*** taken in July 2010. The exposure is 77.7 kg·d.

of different polarities was applied to the shroud to attract or repel the ^{42}K ions generated by the decay of ^{42}Ar. Figure 2.5(b) shows a much reduced event rate in the 1525 keV full absorption peak with the shroud installed compared to a "field free" configuration.

A more recent background spectrum of Phase-I taken during ***Runs 25–29*** is depicted in Fig. 2.6. The total mass of enriched detectors used for the analysis was 14.63 kg, corresponding to an exposure of 3.801 kg·yr. The expected contribution from neutrino-accompanied beta-decay of ^{76}Ge is also shown together with major background contributions obtained from simulation. Note that the sum of the components is not a fit. It

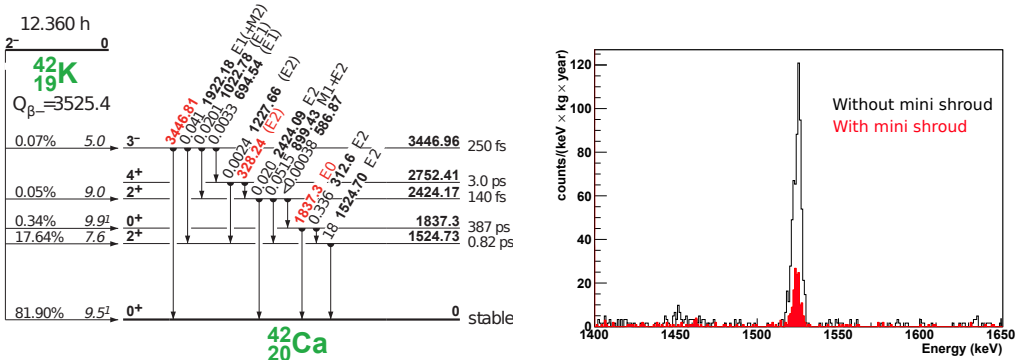

(a) (b)

Figure 2.5: (a) Decay scheme of ^{42}K, taken from [36]. (b) Normalized energy spectra in the energy region (1400–1650) keV in Runs 1-3, without the mini-shroud, and for Runs 10-11, with the mini-shroud [58].

describes the data reasonably well. The minor discrepancies in some regions are being investigated by the analysis team of the GERDA collaboration.

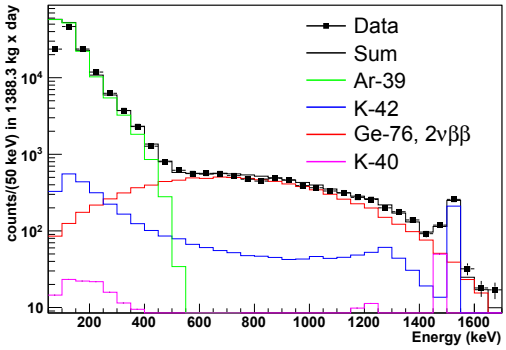

Figure 2.6: Energy spectrum measured with the enriched detectors during Runs 25–29. Also shown are simulated spectra for known background components: Ar-39 from natural argon with an activity of 1 Bq/kg [59], $2\nu\beta\beta$ in Ge-76 with the half life of $1.74 \cdot 10^{21}$ yr [60], K-42 uniformly distributed in liquid argon scaled to the 1525 keV peak, K-40 contribution from the detector holders, scaled to the 1460 keV peak, and Sum of the modeled background spectra. Adopted from Ref. [56].

The currently achieved background index, not taking into account active background suppression methods like pulse shape analysis, is $0.017^{+0.009}_{-0.005}$ ($0.049^{+0.015}_{-0.013}$) cts/(kg·yr·keV) in the energy region of interest for the enriched (non-enriched) detectors [56]. The region of interest was taken between 1839 keV and 2239 keV excluding the window at $Q_{\beta\beta}$, (2039 ± 20) keV, in which the data are blinded. In comparison, the level of background in HdM experiment was 0.16 cts/(kg·yr·keV) at the ROI.

Chapter 3

Germanium detectors

High purity germanium detectors are widely used in spectroscopy, in particular in the detection of single photons from low levels of radioactivity. They are also used in various applications in particle and nuclear physics [61, 62]. In particular, they are used for gamma ray tracking in arrays like AGATA and GRETA [63] and in searches for rare events, like neutrinoless double beta-decay and dark matter as was discussed in Section 1.5.1.

The extraction of information from semiconductor detectors, and in particular germanium detectors, contains several steps. The main mechanisms behind signal formation and extraction are described in this chapter.

3.1 Interaction of particles with matter

The passage of a particle through matter depends on the type of the particle. For any particle, the stopping power in a given material is described by the attenuation length. It is the distance after which $1/e$, or sometimes $1/2$, of the particles remain in the beam with the same energy and momentum; the rest of the particles were lost via an interaction (absorbed, scattered, etc.). Different particles have different mechanisms to deposit energy in the detector. The following particles are relevant for the present work:

1. heavy charged particles: protons, α-particles (alphas), ions;
2. light charged particles: electrons, positrons;
3. photons;
4. neutrons.

Heavy charged particles loose their energy mainly through electromagnetic interaction with electrons. The main process is ionization and excitation of atoms. The energy loss can be described by the quantity dE/dx, the average energy lost by the particle per unit length. The value of dE/dx depends on the energy of the particle and its mass, m. The penetration depth of charged particles is the length after which, in average, a particle has lost all its energy. For an α-particle with an energy of 5 MeV, a common energy of

an α-particle emitted in radioactive decays, it is about 20 μm in aluminum. Sometimes a large portion of the incident energy is transferred to an atomic electron which acquires enough energy for further ionization. These electrons are called δ-electrons. The emission of *bremsstrahlung* photons by heavy particles is rare as it scales as m^{-4}.

Light charged particles deposit energy by the same mechanisms as heavy charged particles. However, the emission of *bremsstrahlung* photons is important and becomes dominant above a certain threshold energy. In a dense material, e.g. lead, this threshold energy is about 10 MeV. The penetration depth of electrons in lead is about 0.5(5) mm for an electron energy of 1(10) MeV.

Photons interact mainly through the following mechanisms:

- Photo-electric effect: a photon is fully absorbed by an atomic electron. The full energy of the photon, E_γ, is transferred to the electron which can be excited or knocked-out of the atom. The electron then can undergo the processes described above. It should be noted that full absorption cannot happen on a free electron, as energy and momentum could not be conserved simultaneously. The photo-electric effect is dominating at lower energies and irrelevant above ≈ 500 keV, depending on the target material.

- Compton scattering: a photon can scatter off an atomic electron with a partial energy transfer. The scattering angle, θ, and the energies of the incoming and outgoing photons, E_γ and E', respectively, are related:

$$1 + \frac{E_\gamma}{m_e c^2}\,(1 - \cos\theta) = \frac{E_\gamma}{E'}, \tag{3.1}$$

  where m_e is the electron mass. The knocked-off electron can further ionize the neighboring atoms or emit a *bremsstrahlung* photon. The Compton scattering process dominates at energies 100 keV$\lesssim E_\gamma \lesssim$ 2 MeV.

- Pair production: in an electric field, a photon can create an electron-positron pair if $E_\gamma > 2m_e = 1022$ keV. The pair production can only occur in an external electric field, created e.g. by nuclei or electrons. It is the dominant component of the total cross section for $E_\gamma \gtrsim 2$ MeV.

For photons, the attenuation length is also usually called penetration depth. It is about 10(15) mm in lead for 1(10) MeV photons. The total cross section of photons as a function of the energy is depicted in Fig. 3.1.

Neutrons are heavy neutral particles. They do not interact electromagnetically, therefore the penetration power of neutrons is relatively high. The mechanisms of interaction of neutrons depend on their energy. They are as follows:

- Radiative capture: *slow* neutrons with a kinetic energy of up to sub-eV can be absorbed by a nucleus. It occurs if the Q-value of this reaction is positive. The outcome of the capture can be the de-excitation of the nucleus with the emission of one or more photons, (n, γ). Alternatively, an electron from the lower shell of the nucleus can be emitted instead of a photon, (n, e). For heavy nuclei, an emission

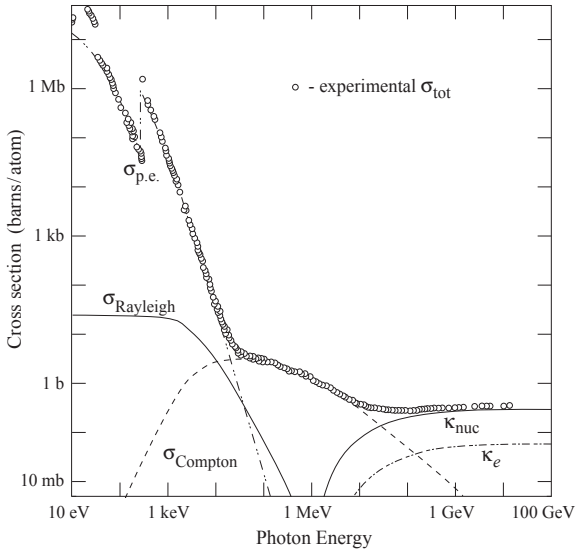

Figure 3.1: Photon total cross section as a function of energy in carbon [19, Ch. 27]. The major contributions are the photoelectric effect $\sigma_{\text{p.e.}}$, Compton scattering σ_{Compton} and pair production in the nuclear/electron field $\kappa_{\text{nuc/e}}$. For a description of σ_{Reyleigh}, please refer to the original reference.

of heavy charged particles is also possible. This process is called transmutation of elements as it produces a nucleus of a different element. Transmutation is the dominating process at sub-eV neutron kinetic energies and above 100 MeV.

- Elastic scattering: a neutron collides with a nucleus, transfers some energy to it (also called recoil energy) and bounces off in a different direction. The recoil energy is usually below 200 keV and its distribution drops exponentially. A series of elastic scatters in the absorbing material is called moderation of neutrons. Elastic scattering is the dominating process for energies between eV to several tens of MeV.

- Inelastic scattering: at energies from 1 to several tens of MeV, a neutron can be temporarily absorbed in the nucleus and form a compound nucleus in an excited state. It then de-excites by emitting another neutron of lower energy together with a photon.

- Deep inelastic scattering: a neutron with a kinetic energy above 1 GeV can interact through its constituents via the exchange of gauge bosons, such as virtual photons, $W^{\pm}/Z$ or gluons. In this process, the interaction can cause the destruction of the neutron and the target nucleus. The result is the emission of various particles like pions, kaons, etc. Neutrons of such high energies naturally only occur as secondary particles in cosmic ray showers. The flux of such neutrons is usually very small compared to the neutrons below the 10 MeV level.

3.2 Germanium detectors characteristics

The basic working principle of semiconductor detectors is the electron-hole creation by the interactions of particles. Crystalline germanium as a semiconductor has a low concentration of intrinsic charge carriers, i.e. electrons in the **conduction band** and holes in the **valence band**. The difference in energy between the lowest level in the conduction band and the highest level in the valence band is called **band gap**. For germanium, the band gap at room temperature is 0.67 eV. For an ideal germanium crystal, at 0 K the conduction band is vacant, and the valence zone is completely filled. With increasing temperature, the kinetic energy of the electrons increases and the probability that they are thermally excited from the valence band to the conduction band increases according to the Boltzmann distribution, $p(E) \sim \exp(-E/kT)$, where E is the kinetic energy of an electron, k is the Boltzmann constant and T is the temperature. Both, electrons in the conduction band and holes in the valence band, contribute to the electric conductivity.

In order to collect electrons and holes created by an interaction, other free charge carriers should not be present. This can be achieved in a diode by applying a reverse bias voltage as depicted in Fig. 3.2. The region between the contacts becomes depleted with increasing bias voltage V. If the full volume of the diode is depleted, the detector is said to be fully depleted. The depleted zone acts as an *active volume* of the detector. Electrons and holes created by an interaction drift to the corresponding contacts due to the electric field and the charges induced on the contacts are collected using charge-sensitive amplifiers.

The detector performance is influenced by several operational conditions. There is

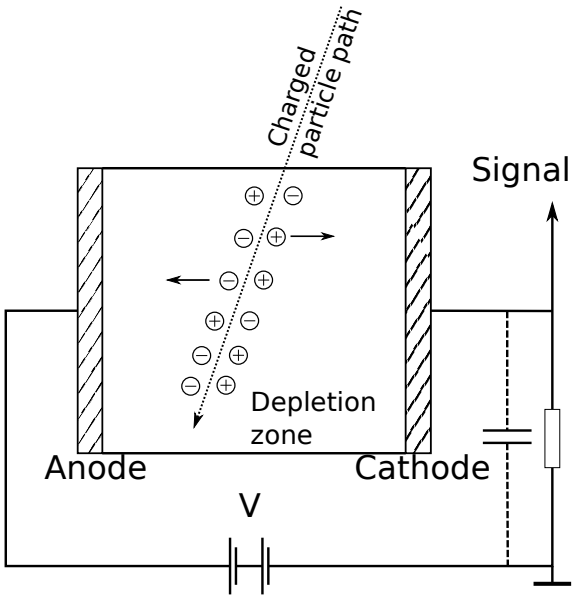

Figure 3.2: Working principle of a semiconductor detector.

always a chance that thermal electrons from the Boltzmann tail in the lattice can have enough energy and can pass the band gap into the conduction band. This current is called the *leakage current*. The leakage current is very temperature-dependent, and therefore germanium detectors have to be cooled down to temperatures of about 100 K.

The properties of a semiconductor detector are determined by the crystal impurities. The presence of *electrically active* impurities leads to additional energy levels in the band gap. There are two types of electrically active impurities: *acceptors* that create additional energy levels in the band gap close to the valence band, and *donors* that create additional energy levels close to the conduction band. With additional levels in the band gap, the electric conductivity becomes larger and higher voltages are needed to deplete a detector. This is why germanium detectors are produced from ultra-high-purity material. Modern germanium detectors may contain as little as 10^9 electrically active impurities per cm^3, which corresponds to one atom of impurities per 10^{13} atoms of germanium. The common level of impurities of $\mathcal{O}(10^{10})/\mathrm{cm}^3$ provides the possibility to fully deplete a detector over several centimeters with a depletion voltage of several kilovolts.

The need for large detector volumes with manageable depletion voltages leads to a *coaxial* detectors geometry. Coaxial detectors are cylindrical with a central bore which either penetrates (*true-coaxial*) or leaves a cap. The contacts are inside the bore hole and on the mantle.

Germanium detectors can also be manufactured with a segmentation of the mantle electrodes. This opens the possibility to obtain information on event topologies. This can be used for gamma tracking [63] and background rejection in low background experiments [64].

3.3 Signal formation

The mechanism of signal formation is described numerically by the Ramo-Shockley theorem. The drift trajectories of the charge carriers, electrons and holes, determine the time evolutions of the charge and current induced on the read-out electrodes, the so called charge and current pulses, according to the formulas [65, 66]:

$$Q(t) = -Q_0 \times [\phi_w(\boldsymbol{r}_h(t)) - \phi_w(\boldsymbol{r}_e(t))]\,, \tag{3.2}$$

$$I(t) = Q_0 \times [\boldsymbol{E}_w(\boldsymbol{r}_h(t)) \cdot \boldsymbol{v}_h(t) - \boldsymbol{E}_w(\boldsymbol{r}_e(t)) \cdot \boldsymbol{v}_e(t)]\,, \tag{3.3}$$

where Q_0 is the total charge carried by electrons/holes, $\boldsymbol{r}_{h/e}(t)$ and $\boldsymbol{v}_{h/e}(t)$ are the positions and the velocities of the charge carriers at time t, $\phi_w(\boldsymbol{r})$ and $E_w(\boldsymbol{r})$ are the weighting potentials and the weighting fields, respectively. The latter are calculated for each electrode by solving the Poisson equation, $\Delta\phi_w(\boldsymbol{r}) = 0$, with the boundary conditions: $\phi_w(\boldsymbol{r}) = 1$ on the corresponding electrode and 0 on all other electrodes.

If the charge carriers are not trapped on their drift path, the **pulse amplitude**, i.e. the charge collected on the electrode, is proportional to the energy deposited in the detector. The shape of the pulse contains information on the drift of the charge carriers. It can be used to extract information about position of the interaction. Important is also the **pulse**

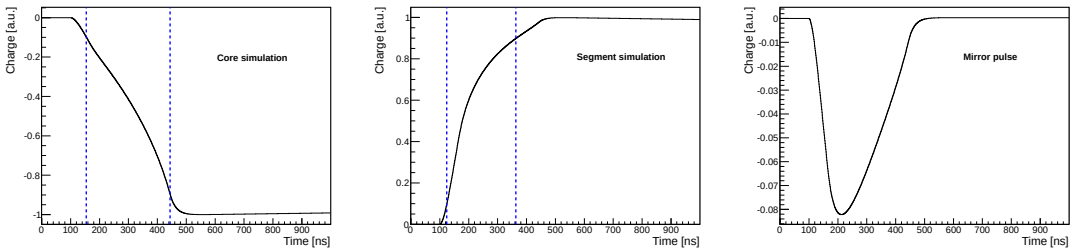

(a) (b) (c)

Figure 3.3: Examples of pulses simulated for a true-coaxial segmented detector for (a) the core electrode, (b) the segment electrode collecting charge and (c) the neighboring segment where a mirror pulse is induced. The pulse amplitudes were normalized to the absolute value of the amplitude of the core pulse. Please note the different scales for the collected and the mirror pulse. The times at which the pulses (a) and (b) reach 10 % and 90 % of the amplitude are indicated as dashed lines.

length, which corresponds to the time during which charge carriers drift. Often used is the time interval in which a pulse grows from 10 % to 90 % of its amplitude, the *10–90 rise time*, $t_r^{10\text{–}90}$, see Fig. 3.3(a) and 3.3(b).

The geometry of the detector determines the electric field configuration and thus the drift trajectories. In true-coaxial detectors, the pulse lengths slightly depend on the initial energy deposit. In a closed-end detector, the electric field configuration is very different from the one in a true-coaxial detector. As the result, pulse shapes strongly depend on the location of the energy deposit. Pulse lengths may in this case be significantly different.

At the end of the drift, the charge carriers will reach one or more segments in which the full energy pulse is collected. The charge on the collecting electrodes is induced while the charge carriers drift. However, charge is also induced on electrodes that do not collect, leading to *mirror pulses*, see Fig. 3.3(c). Mirror pulses return to the baseline once the charge carriers reach the collecting electrodes. The amplitude of a mirror pulse depends on the distance of the charge carriers to the relevant electrode and is usually several orders of magnitude smaller than the real pulse. Mirror pulses may also be used to reconstruct the position of the energy deposits [67].

3.4 Crystal structure

Not only the external field, but also the crytal structure has influence on the trajectories of charge carriers. Germanium crystals have a face-centered cubic (*fcc*) lattice with four additional atoms associated with each point of the *fcc* lattice. The tetrahedral bonding characteristic of this structure is shown in Fig. 3.4(a). The corresponding tetrahedron structure with the principal crystallographic axes, $\langle 001 \rangle$, $\langle 100 \rangle$, $\langle 110 \rangle$ and $\langle 111 \rangle$, is shown in Fig.3.4(b).

The physical properties of germanium differ along the different axes. This is caused by different energy levels for the electrons located around different axes.

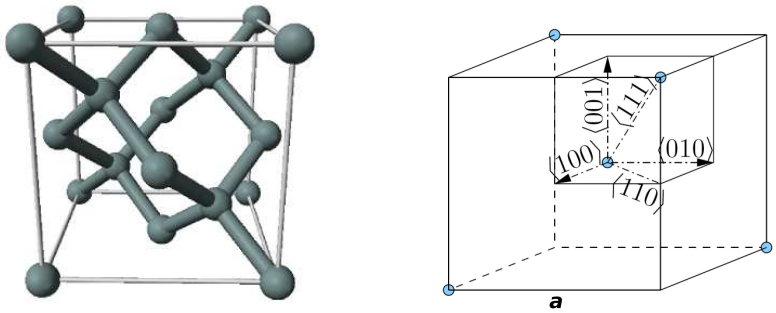

(a) (b)

Figure 3.4: Schematic view of a face-centered cubic germanium crystal: (a) location of nuclei, (b) crystallographic axes [68].

Electrons can be excited from the valence band to the conduction band by the absorption of an optical photon. This absorption process can either be **direct** or **indirect**. In the **direct** process, see Fig. 3.5(a), an optical photon with the energy $E_g = \hbar\omega_g$ can be absorbed by the crystal, leaving an electron in the conduction band and a hole in the valence band. In the **indirect** process, see Fig. 3.5(b), the minimum energy gap of the band structure involves electrons and holes separated by a wavevector $\boldsymbol{k}_c$. Here, a direct photon transition across the minimal gap cannot satisfy the requirement of conservation of wavevectors. But if a thermal phonon with a wavevector $\boldsymbol{K} = -\boldsymbol{k_c}$ and frequency Ω is created, the wavectors can be conserved if $\hbar\omega = E_g + \hbar\Omega$. The phonon energy $\hbar\Omega$ ($\sim$0.01–0.03 eV) is generally much smaller than the energy gap, E_g ($\sim$ 1 eV).

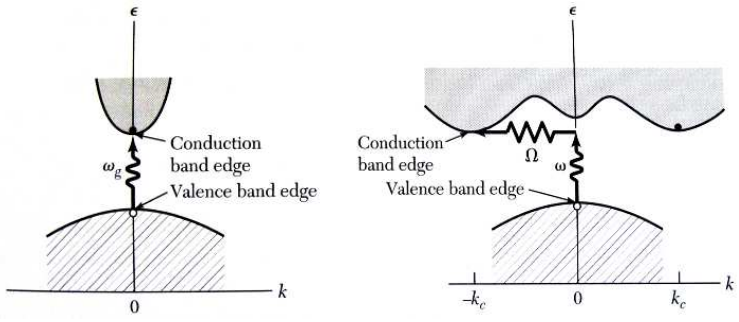

(a) (b)

Figure 3.5: In (a) a direct optical transition is drawn vertically with no significant change of $\boldsymbol{k}$. The threshold frequency ω_g for absorption determines the energy gap $E_g = \hbar\omega_g$. The indirect transition in (b) involves both a photon and a phonon. The threshold energy for the indirect process in (b) is greater than the true band gap, $E_g = \hbar\omega + \hbar\Omega$. The picture adopted from [69].

The band structure in germanium [69] is quite complicated. The edge of the lowest

conduction band is relevant for electrons located on the ⟨111⟩ axis. The equipotential surfaces in this region form prolate ellipsoids and are called **valleys**. They are shown in Fig. 3.6.

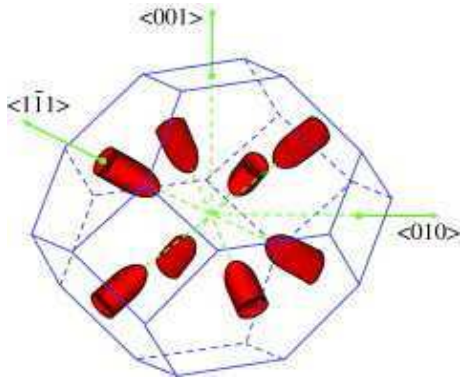

Figure 3.6: Eight half-ellipsoidal valleys along ⟨111⟩ directions, where electrons have minimal energies [70].

Due to the valley structure the drift velocity of the electrons depends on the relative orientation of the drift induced by the external electric field to the crystallographic axes. This dependence in described by the ***mobility***, μ, connecting the velocity, $\boldsymbol{v}(\boldsymbol{r})$, and the electric field, $\boldsymbol{E}(\boldsymbol{r})$: $\boldsymbol{v}(\boldsymbol{r}) = \mu \cdot \boldsymbol{E}(\boldsymbol{r})$. The velocity of electrons and holes is the highest along ⟨100⟩ and the lowest along ⟨111⟩ [71].

At temperatures relevant for germanium detectors operation, $T \approx 100\,\mathrm{K}$, at which the temperature of the crystal, T_{lattice}, is much larger then the temperature of charge carriers, T_e, the mobility is a tensor and the trajectories of charge carriers do not necessarily follow the electric field lines [72, 73, 74]. This effect causes the so called *transverse anisotropy* in a crystal.

The mobility tensor is temperature dependent. This has been modeled using the approximation of charge carrier scattering off acoustic phonons [75]. A moving electron or hole reacts with the crystal vibrations, i.e. it interacts with waves of the crystal lattice, and is scattered. The amplitude of the crystal waves depends on the temperature, T. This dependence is reflected in the T dependence of the mobility. In this approximation, $\mu \propto T^{-3/2}$. Later measurements of the electron mobility showed slightly different temperature dependencies, $\mu \propto T^{-1.6}$ [76] and $\mu \propto T^{-1.66}$ [77].

Studies on electron and hole mobility will be presented in Chapters 6 and 7.

3.5 Test facilities for germanium detectors at the MPI

Several test facilities for germanium detectors are available at the Max-Planck-Institute for Physics, Munich. Two of them, **Gerdalinchen-II** and **K1** were used.

Gerdalinchen-II is a special cryostat developed by the technical division of the Max-Planck-Institute for Physics to test up to three segmented germanium detectors submerged

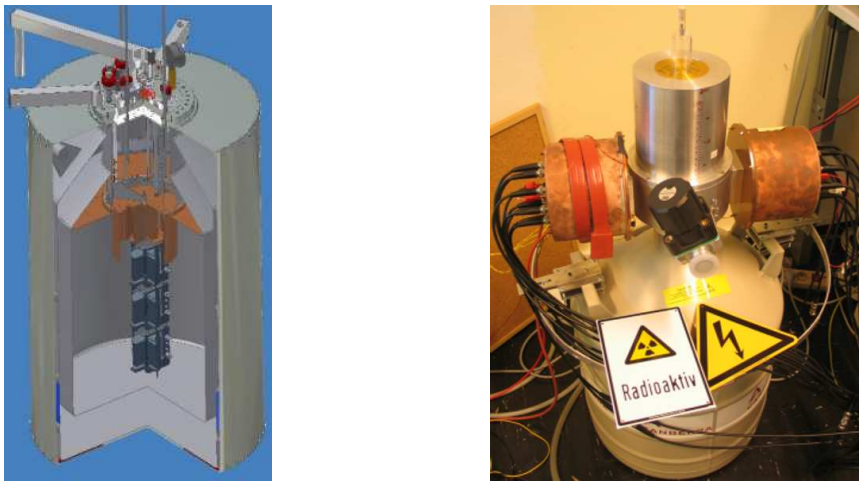

(a) Gerdalichen-II. (b) K1.

Figure 3.7: Test facilities at the MPI.

in cryogenic liquid. It consists of a two-walled cryogenic dewar inside a cylindrical aluminum tank. A schematic view is depicted in Fig. 3.7(a). A detailed description of the setup can be found in [78]. The top flange is moved up to mount detectors and a source either with or without a collimator. During operation, the source cannot be exchanged. The source position can be varied vertically in z, and by about 90° in the polar angle, ϕ.

K1 is a vacuum cryostat that was procured by Canberra-France. It was designed for the characterization of segmented detectors. It consists of a two-walled aluminum vacuum can for the detector. The vacuum can holds two copper "ears" developed at the MPI housing the pre-amplifier boards. The detector in K1 is cooled down through a copper cooling finger submerged in a standard liquid nitrogen dewar. The setup is depicted in Fig. 3.7(b). Due to the changing level on liquid nitrogen in the dewar, the temperature of the detector increases with time. It and can be measured by a PT-100 thermistor installed as close to the detector as possible. Collimated or non-collimated calibration sources can in principle be positioned in any position except those occupied by the "ears".

The signals in both setups were read out by PSC-823C charge-sensitive pre-amplifiers, produced by Canberra-France, with a decay time of 50 μs and a total bandwidth of about 10 MHz. In the Gerdalinchen-II setup, all FETs of the pre-amplifiers were installed on the pre-amplifier boards. In K1 the situation was different. The FET for the core was installed inside the vacuum can as close to the detector as possible. The segment FETs were incorporated in the pre-amplifier boards installed in the "ears". As the signal of the core cable was pre-amplified inside the K1 cryostat, but fed through the cryostat cap on the same feedthrough as some segment signals, it caused significant crosstalk during the data taking period denoted as ***Run 6***. To reduce the crosstalk in K1, the core read-out cable was remounted to a feedthrough not containing segment signal lines for ***Run 7***. Schematic layouts of the read-out cables and feedthroughs for ***Run 6*** and ***Run 7*** are depicted in Fig. 3.8. The following notations are used for the core FET: **D** for drain, **S** for source, **FB**

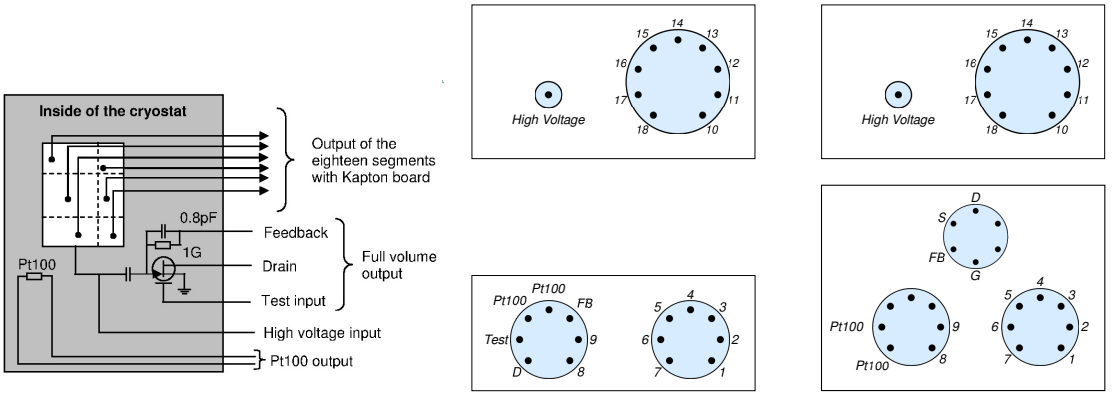

(a) Read out scheme

(b) Layout of the feedthroughs, Run 6

(c) Layout of the feedthroughs, Run 7.

Figure 3.8: Layout of the front-end electronics mounted in the K1 cryostat. For notations please refer to the text.

for feedback and **G** for ground. The numbers indicate segment numbers.

Energies and pulses were recorded using a "DGF Pixie-4" data acquisition system, DAQ, manufactured by X-Ray Instrumentation Association, XIA. The DAQ has 14-bit ADCs and operates at a sampling frequency of 75 MHz. Detailed specifications can be found elsewhere [79].

The properties of segmented detectors were measured and their operation under different conditions was tested using the Siegfried-I and Siegfried-II detectors, manufactured by Canberra-France. They are 18-fold ($3z \times 6\phi$) segmented n-type detectors. The Siegfried-II detector is depicted in Fig. 3.9. The main geometrical and physical parameters of the detectors as reported by the manufacturer are listed in Table 3.1. Siegfried-I was already characterized in detail [67], Siegfried-II was previously used to test the performance in a cryogenic liquid [80]. New studies on Siegfried-II published in [81] and [82] will be presented

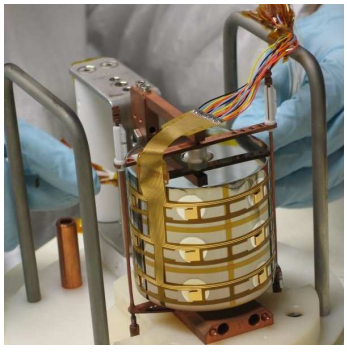

Figure 3.9: The Siegfried-II detector being prepared for installation.

Parameter	Siegfried-I	Siegfried-II
Height [mm]	70	70
Inner radius [mm]	5	5
Outer radius [mm]	37.5	37.5
Impur. level, top [10^{10}/cm^3]	0.70	0.35
Impur. level, bottom [10^{10}/cm^3]	1.35	0.55
Operation voltage, [V]	3000+	2000+

Table 3.1: Main parameters of Siegfried-I and Siegfried-II.

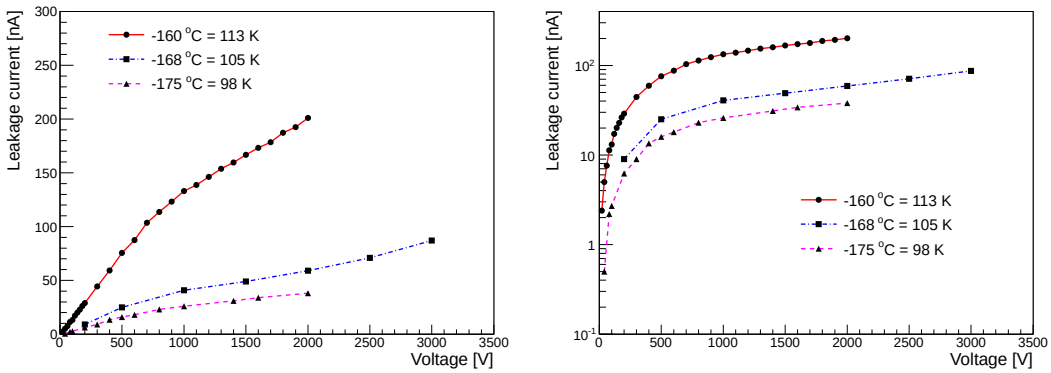

(a) (b)

Figure 3.10: Leakage current of the Siegfried-II detector as a function of the bias voltage for different temperatures in (a) linear and (b) logarithmic scales. The markers show the measurement points.

in detail in Chapters 6 and 7.

One of the segments, Segment 9, of the Siegfried-II detector was damaged, resulting in a high leakage current through Segment 9. It is shown in Fig 3.10 measured for selected temperatures and bias voltages. The detector was, however, fully functional, except for deteriorated energy resolutions in the core and segment 9.

Chapter 4

Possible background sources in GERDA and future experiments

The present work continues the studies on background contributions expected in the GERDA experiment and future projects. The major contributions in GERDA have been studied during Monte Carlo campaigns before [83, 84, 85]. They were performed for various contaminations in detectors, detector strings and the GERDA infrastructure. In the following studies, further possible background sources in the cable chains and the cleanroom floor were investigated. They were considered for GERDA Phase II, in which the foreseen background index should not exceed 10^{-3} cts/(kg·yr·keV) in the energy region of interest.

The next generation of experiments for searches of neutrinoless double beta-decay in ^{76}Ge would need an active mass of ≈ 1 ton of germanium and a background level below 10^{-5} cts/(kg·yr·keV) in the energy region of interest, which is three to four orders of magnitude lower compared to the level reached so far. This necessitates the investigation of so far unimportant background contributions. The background expected from the detector metalization and muon-induced neutrons inside germanium crystals was calculated.

4.1 Monte Carlo simulation

A Monte Carlo simulation was performed using the MaGe [86] framework based on Geant4 [87]. An array of true coaxial HPGe detectors corresponding to a nominal phase II arrangement of GERDA, denoted as *PhaseIIideal*, was simulated. The array consisted of seven strings with three detectors each, with the strings being aligned at the same height. The configuration had hexagonal closest packing with a closest radial distance of 15 mm between the detector surfaces. The distance in height between the detector boundaries was 60 mm. All detectors were true coaxial n-type 18-fold segmented with 75 mm diameter and 70 mm height and a bore hole diameter of 10 mm [67].

For the simulation of decay chains an event splitter based on timing information was applied. If not applied, it results in energy deposits of all the daughter decays being summed together. With the time splitter the daughter events following in intervals longer than 100 μs, a typical dead time of the existing pre-amplifiers, were recorded in separate

events.

The *BBdecay* realm was used in the simulation. The energy resolution $\sigma(E)$ of the detectors was simulated as

$$\begin{aligned} \sigma(E) &= \frac{\sqrt{a^2 \cdot E + b^2}}{\sqrt{\ln 2 \sqrt{8}}}, \\ a &= 0.0405, \\ b &= 1.31, \end{aligned} \tag{4.1}$$

where E is the segment or core energy in keV. The term a describes the noise due to the Fano factor and b describes the electronic noise. Both values were set according to measurements with germanium detectors previously performed in the group at the Max-Planck-Institute for Physics (see e.g. [84]).

The following contributions were simulated:

- Electronics cables

  The contributions from ^{108m}Ag and ^{110m}Ag in the signal and high voltage cables were simulated. ^{108m}Ag and ^{110m}Ag have a complicated decay scheme [36] with a possible emission of two gammas in a prompt cascade with the total energy above $Q_{\beta\beta}$ of ^{76}Ge. The cables are implemented as boxes of 0.4 mm×9 mm×3.038 m with an average density of 8.715 g/cm^3. The total mass of a single cable box is 95.3 g, among which 94.5 g of copper and 0.73 g of kapton. It is located above the front-end electronics in each string with its lower end ≈30 cm above the detectors. The cables are contained in hollow boxes corresponding to the stainless steel cable chains. The thickness of the cable chains surrounding the cables is 0.8 mm. The part of the cables above 3 m is irrelevant for the background estimation [84].

  In total a simulation of 70·10^6 decays of both ^{108m}Ag and ^{100m}Ag each randomly distributed in the cables was performed.

- Cleanroom floor.

  It is part of the infrastructure located far from the detectors, therefore limitations on the level of radioactivity are less severe. However, the filler material has a measured activity of ≈10 mBq/kg of ^{228}Th [88], thus the expected contribution to the background in the ROI needs to be studied in some more detail. The contamination from ^{228}Th in the cleanroom floor was simulated. The floor was simulated as a 2 mm thick plate of (10×10) m^2 located on top of the cryostat. Low energy gamma lines do not penetrate that far, therefore only 2.6 MeV gammas from ^{208}Tl were simulated. In total 400·10^6 gammas randomly distributed in the cleanroom floor volume were simulated. To save computing time, the gammas were always pointing to the detector array, within a box $(30 \times 30 \times 30)$ cm^3 located ≈5 m below the cleanroom floor. This scales to the value of $\mathcal{O}(5 \cdot 10^{12})$ isotropically emitted gammas inside the cleanroom floor.

- Detector metalization

It is a thin layer of aluminum usually covering the outer surface of n-type HPGe detectors. The metalization is implemented in MaGe as an outer cylindrical dead layer of 40 μm thickness, however it is usually a much thinner layer. The height of the dead layer corresponds to the detector height, i.e. $\approx$ 7 cm. Contributions from ^{26}Al and ^{22}Na cosmogenically produced in the metalization were simulated. Decay schemes of ^{26}Al and ^{22}Na are shown in Fig. 4.1. Both isotopes decay via β-decay with their Q_β values larger than $Q_{\beta\beta}$ value of germanium. Being located on the detector surface, the electrons emitted in a β-decay contribute to the background in the region of interest around $Q_{\beta\beta}$ of ^{76}Ge. A detailed description of the origin of ^{22}Na and ^{26}Al in aluminum is given in Ref. [89].

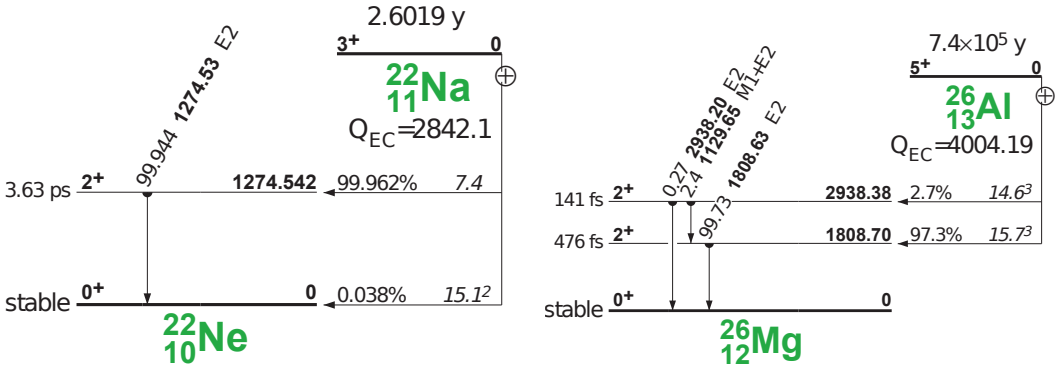

Figure 4.1: Decay schemes (a) ^{22}Na$\rightarrow^{22}$Ne and (b) ^{26}Al$\rightarrow^{26}$Mg.

In addition, primordial ^{226}Ra and ^{228}Th contaminations were simulated.

For the detector metalization, 25.2·10^6 decays of each isotope being randomly distributed on the metalized surfaces of all detectors was performed.

- Neutrino-induced neutron background in HPGe detectors.

  At a depth above 12 km of water equivalent underground the flux of cosmic ray muons saturates and does not decrease anymore with depth [19, Chapter 24], [25, Cosmic rays]. The remaining muon component arises from the neutrino interactions in the rock, producing muons. Interactions of muons in dense material can lead to the production of neutrons. The expected flux in germanium is shown in Fig. 4.2. The neutrons can deposit energy in the detectors, also in the region of interest. Interaction of neutrons produced in the detectors was simulated for an extended GERDA array geometry. The array consisted of 19 strings with 5 detectors each and is denoted below as *PhaseIImaximum*. The detectors and relative distances between them remained the same as for the *PhaseIIideal* configuration. 190·10^6 events with an energy distribution shown in Fig. 4.2 randomly distributed in the detectors were simulated.

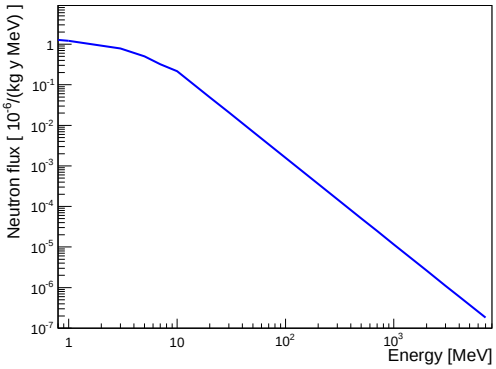

Figure 4.2: Neutron flux in germanium induced by upwards going muons from the atmospheric neutrino interaction in Earth obtained from parametrization [90].

4.2 Contamination of aluminum in detector metalization

The metalization of n-type HPGe detectors are usually made of aluminum. Aluminum is refined from bauxite deposits that have rested on or close to the surface for the past million years. The bauxite layers are usually as thin as 2 m to 4 m [91].

The isotopic composition of aluminum in bauxite is almost 100 % of ^{27}Al which is a stable isotope. Secondary cosmic rays can cosmogenically activate the aluminum and produce ^{26}Al and ^{22}Na. In order to account for the shielding by the top soil and the self shielding of the bauxite layer, a Monte Carlo simulation of the cosmic radiation was performed. The MaGe [86] framework based on Geant4 [87] was used.

Two scenarios, typical for major bauxite mining sites, were taken into account: a top soil free mining site and a site with 1 m quartz sand overburden. The composition of the simulated bauxite was chosen according to the one reported for the WEIPA site [92].

The neutron and proton fluxes were simulated at different depths in the bauxite layer: for depths between 0 m and 0.5 m in steps of 0.1 m and for depths between 0.5 m and 2.0 m in steps of 0.5 m. The fluxes calculated for the different depths were averaged to obtain the mean neutron spectra for a bauxite layer with 2 m thickness with and without top soil. The neutron and proton fluxes at sea level were taken from Ref. [93] and [94], respectively

The simulated spectra for neutrons and protons are shown in Fig. 4.3 and Fig. 4.4, respectively. The averaged spectra were used for calculating realistic ^{26}Al and ^{22}Na production rates within a 2 m bauxite layer.

Using parametrization of the measured production cross-sections of ^{27}Al(p,pn)^{26}Al and ^{27}Al(p/n,X)^{22}Na summarized in Ref. [89], the calculated production rates of ^{26}Al and ^{22}Na are listed in Table 4.1.

In equilibrium, the decay and production rates of the isotopes are equal. The equilibrium is achieved after several half lives. It is the case after a few million (10) years for ^{26}Al(^{22}Na). The expected equilibrium activity of ^{26}Al for a 2 m bauxite deposit without top soil is 0.8 mBq/kg. For ease of scaling, an activity of 1.0 mBq/kg was used for the background estimates. ^{26}Al cannot be easily removed during the refining process. Due to

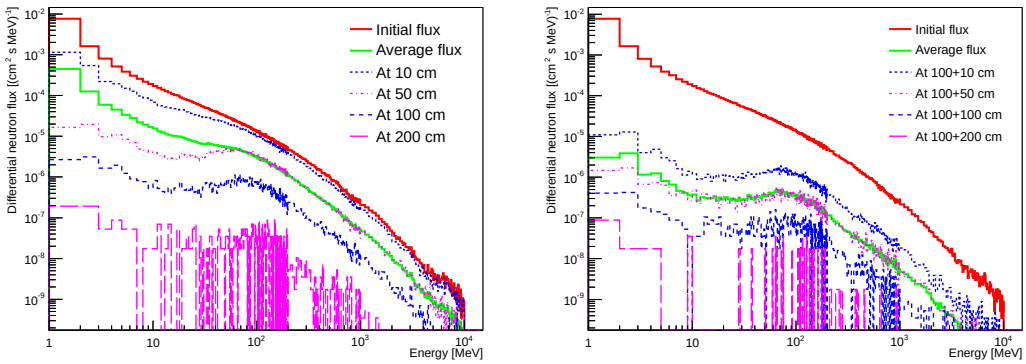

(a) (b)

Figure 4.3: Simulated differential neutron fluxes at different depths and in average in bauxite with (a) no top soil and (b) a 1 m layer of top-soil. The initial flux at the sea level was taken from Ref. [93].

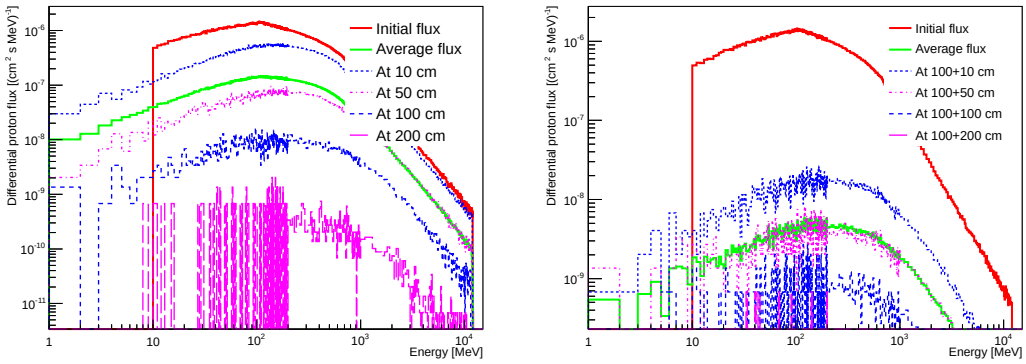

(a) (b)

Figure 4.4: Simulated differential proton fluxes at different depths and in average in bauxite with (a) no top soil and (b) a 1 m layer of top-soil. The initial flux at the sea level was taken from Ref. [94].

its long half life, the decay rate of ^{26}Al is constant for a long period, thus also during the lifetime of any experiment.

The contamination with ^{22}Na is eliminated effectively during the refining process. Thus, for ^{22}Na it is the exposure history after aluminum refinement that determines its activity. After one half life (2.6 years) of exposure to cosmic rays, the decay rate is equal to half of the production rate. For no overburden at sea level, this corresponds to 1.0 mBq/kg. This value was assumed to estimate the background rates.

	^{26}Al		^{22}Na	
	[(g·yr)$^{-1}$]	[mBq/kg]	[(g·yr)$^{-1}$]	[mBq/kg]
Neutrons at sea level	142	4.5	56	1.8
Neutrons in 2 m bauxite	21	0.67	11	0.4
Neutrons, 1 m quarz sand + 2 m bauxite	1.4	0.04	1.0	0.03
Protons at sea level	17	0.54	8.7	0.10
Protons in 2 m bauxite	2.1	0.07	1.0	0.03
Protons, 1 m quarz sand + 2 m bauxite	0.1	0.0	0.01	0.0
n+p, 2m bauxite	23	**0.74**		
sea level, half equilibrium			32	**1.0**

Table 4.1: Calculated production rates and corresponding activities for secular equilibrium for ^{26}Al and ^{22}Na for different overburden scenarios: for a 2 m thick bauxite layer accounting for self absorption and for a 2 m thick bauxite layer underneath 1 m top soil. The last two lines give a realistic prediction for ^{26}Al, where equilibrium is assumed after millions of years in a 2 m bauxite layer, and for ^{22}Na, where half equilibrium is reached at the surface after refinement of the aluminum. Adopted from Ref. [89].

4.3 Calculation of background indices

The background index in the region of interest between 1939 keV and 2139 keV for each type of simulated particles was calculated as

$$BI = SP \cdot \frac{A}{\Delta E} \cdot \frac{m_{\text{material}}}{m_{\text{Ge}}}, \tag{4.2}$$

where SP is the survival probability, i.e. the ratio of events with energy deposited in the detector to the number of generated events in the energy region of interest, A is the specific activity of material in Bq/kg, $\Delta E = 200$ keV is the region of interest around $Q_{\beta\beta} = 2039$ keV, m_{material} is the mass of the material in a considered part and $m_{\text{Ge}} = 35.3(159.6)$ kg is the total mass of detectors in the *PhaseIIideal* (*PhaseIImaximum*) array. The activities used for different materials are listed in Table 4.2.

Background events induced by photon interactions can be identified through the event topologies by requiring the energy to be deposited in a single detector or in case of segmented detectors a single segment [95]. Applying single segment cuts compared to single detector cuts can reduce the background in the region of interest by typically an order of magnitude, depending on the background source. Therefore, the background indices were calculated with no cut on granularity, for single detector, and single segment events. Pulse shape analyses using detectors with a special field configuration, e.g. BEGe detectors, can lead to similar background identification efficiency.

4.4 Results

There were no events in the energy region (2039 ± 100) keV in the spectra of the simulated contaminations in the cleanroom floor and the cables. The calculated background

Part	Total part mass	Isotope	Activity [mBq/kg]
Cleanroom floor	1575 kg	^{208}Tl	10 000
Cables	7×95.3 g	^{108m}Ag	5.0
		^{110m}Ag	1.0
Metalization	21×13.4 mg [89]	^{22}Na	1.0
		^{26}Al	1.0
		^{226}Ra	1.0
		^{228}Th	1.0
Detectors	159.6 kg	Neutrons	–

Table 4.2: Activities of isotopes assumed for selected parts of the GERDA setup and the corresponding masses of the parts.

Part	Isotope	Total BI [10^{-4} cts/(kg·yr·keV]
Cleanroom floor	^{208}Tl	$< \mathcal{O}(0.2)$ (90 % C.L.)
Cables	^{108m}Ag	$< 5 \cdot 10^{-3}$ (90 % C.L.)
	^{110m}Ag	$< 9 \cdot 10^{-4}$

Table 4.3: Limits on the expected background contribution from ^{108m}Ag and ^{110m}Ag in the readout cables and ^{208}Tl in the cleanroom floor in a GERDA like setup.

indices were calculated assuming that the measured number of events was < 2.3, which corresponds to the confidence level of 90 %. The upper limits are listed in Table 4.3. They are significantly below the level of 10^{-4} cts/(kg·yr·keV), therefore are not critical for GERDA Phase II.

The results of the simulation in the detector metalization are listed in Table 4.4. The simulated spectra, normalized to the expected number of decays per year and kilogram of germanium, without any cut, with single detector cut and with single segment cut are shown in Fig. 4.5 and 4.6. The resulting spectra in the energy window between 1939 keV and 2139 keV are shown in the insets of Figs. 4.5 and 4.6. For ^{26}Al, the background rate in the region of interest is approximately constant. A background rate of up to $0.17 \cdot 10^{-5}$ cts/(kg·yr·keV) is expected for a single segment cut. This is not critical for GERDA Phase II. The background expected from ^{22}Na is $\approx 2.6 \cdot 10^{-7}$ cts/(kg·yr·keV) and thus even less critical. The contribution due to a 1.0 mBq/kg ^{228}Th contamination is expected to be $0.5 \cdot 10^{-5}$ cts/(kg·yr·keV), while for ^{226}Ra it is $0.26 \cdot 10^{-5}$ cts/(kg·yr·keV).

If no cut based on event topologies is made, the background rate is higher by roughly one order of magnitude. In this case the background will be at levels of up to 10^{-4} cts/(kg·yr·keV). A single detector cut reduces the backgrounds due to the decays of ^{22}Na and ^{26}Al by factors of 1.4 and 3.2, respectively. A single segment cut gives suppression factors of 10 and 30 for ^{22}Na and ^{26}Al, respectively. For ^{226}Ra and ^{228}Th, the single segment cut gives only suppression factors of 2.6 and 4.5, respectively.

The obtained tolerated activities of the considered nuclides to restrict the background to 10^{-6} cts/(kg·yr·keV) with single segment cut applied are summarized in the last row of

Table 4.4. While for ^{22}Na an activity of a few mBq/kg can be tolerated, the restrictions on ^{26}Al, ^{226}Ra and ^{228}Th contaminations are more severe at the hundreds of μBq/kg level. The tolerated activities are within the measured limits from existing aluminum samples as reported in Ref. [89].

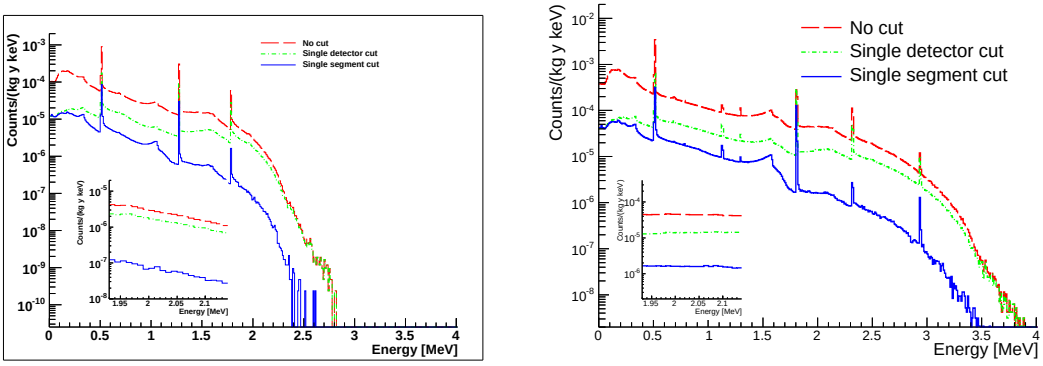

(a) Na-22 (b) Al-26

Figure 4.5: Simulated spectrum from a 1.0 mBq/kg (a) ^{22}Na and (b) ^{26}Al contamination in the metalization of HPGe detectors in a GERDA like setup. Spectra are without any cut, with single detector cut and with single segment cut. The region of interest is shown in the inset.

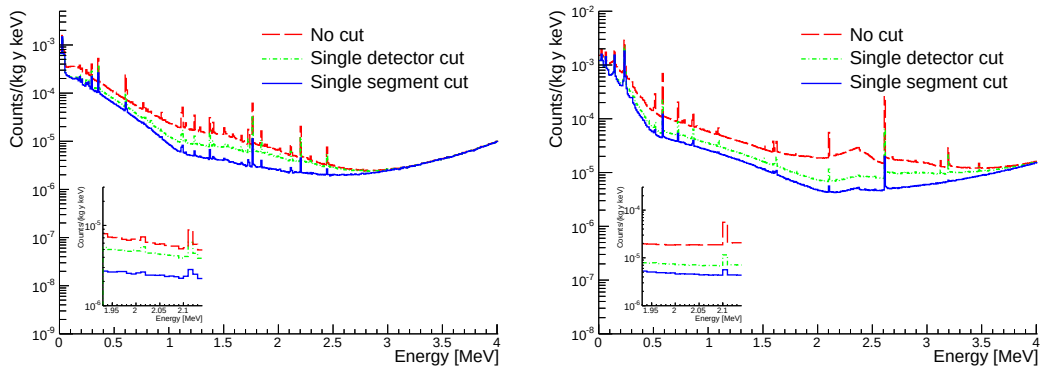

(a) Ra-226 (b) Th-228

Figure 4.6: Simulated spectrum from a 1.0 mBq/kg (a) ^{226}Ra and (b) ^{228}Th contamination in the metalization of HPGe detectors in a GERDA like setup. Spectra are without any cut, with single detector cut and with single segment cut. The region of interest is shown in the inset.

The energy spectrum from muon-induced neutrons in the detectors is shown in Fig. 4.7 with no cut, single detector cut and single segment cut. The background index with not cut is $5 \cdot 10^{-11}$ cts/(kg·yr·keV). The single segment cut reduces this by a factor of almost 13. This is much below the requirement of 10^{-6} cts/(kg·yr·keV) per contribution

Nuclide	Number of events in ROI			Background index			Allowed activity
	total	SD cut	SS cut	total	SD cut	SS cut	
				[10^{-5} Counts/(kg·yr·keV)]			[mBq/kg]
^{22}Na	209 374	122 942	5 335	0.26	0.16	0.03	**3.3**
^{26}Al	843 308	26 828	30 670	4.62	1.45	0.17	**0.6**
^{228}Th	419 903	149 115	93 647	2.19	0.78	0.49	**0.2**
^{226}Ra	127 017	93 907	49 846	0.67	0.49	0.26	**0.4**
neutrons	296 495	104 556	22 847	$5.0{\cdot}10^{-6}$	$1.8{\cdot}10^{-6}$	$3.8{\cdot}10^{-7}$	–

Table 4.4: The first three columns show the simulated number of events which have an integrated energy deposit between 1939 keV and 2139 keV in the detector array (total), in a single detector (SD cut) and in a single segment (SS cut) of a detector. The resulting background indices expected for an activity of 1.0 mBq/kg in this energy window are given in the next three columns. The last column lists the activity allowed to restrict the background to 10^{-6} cts/(kg·yr·keV).

for future experiments for $0\nu\beta\beta$ searches. For experiments like GERDA neutrons can also be produced in the surrounding liquid argon, which has a much larger mass and therefore the production rate. This contribution was however not studied. Note that the rate of muon-induced neutrons can be significantly reduced by a muon veto usually installed in the experiments.

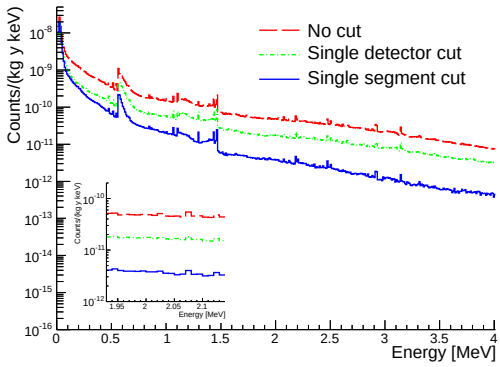

Figure 4.7: Simulated spectrum from neutrino-induced neutrons in the HPGe detectors a GERDA like 95-detector setup. Spectra are without any cut, with single detector cut and with single segment cut. The region of interest is shown in the inset.

4.5 Summary

The considered background sources in the cleanroom and the cables did not contribute to the spectrum around 2039 keV expected in a GERDA like setup. The investigations also show that for future neutrinoless double beta-decay experiments using HPGe detectors

the material used to metalize the surfaces of the detectors has to be carefully screened for radio-impurities.

It was shown that the neutrino-muon-induced neutron background in germanium detectors installed in deep underground laboratories is not large and can be neglected for the next generation of experiments with HPGe detectors, such as the 1-tonne approach.

Chapter 5

Pulse shape analysis using neural network

Key to all low-background experiments like GERDA is to effectively suppress background radiation. Methods of passive shielding were discussed in Section 1.5.1. Granularity cuts and supplementary classification of event topologies by Pulse Shape Analyses (PSA) can help to identify background.

Event topologies of background events can be significantly different to those of typical signal events. Monte Carlo simulations facilitate a quantitative description of different classes of event topologies using the spatial distribution of the individual energy deposits inside a detector as a measure of topology. The spread of energy deposits inside the detector can be described by the radius of the smallest sphere containing 90 % of energy in an event, R_{90}. A "localized" event has a small value of R_{90}. For example, in a $0\nu\beta\beta$ the two emitted electrons create a charge cloud with $R_{90} \sim 1\,\mathrm{mm}$ [95]. Such a localized event is called Single Site Event (SSE). On the contrary, a Compton scattered photon that is absorbed in a distant position inside the detector from the scattering point, will have two separated energy depositions. Such an event may have an R_{90} of several cm and is called Multi Site Event (MSE). The difference in drift paths and times of the charge carriers of SSEs and MSEs is reflected in the pulse shapes due to their different signal formation history described in detail in Section 3.3. PSAs exploit these differences in order to distinguish signal-like events from background-like events.

PSA methods have already been used for several applications with germanium detectors [96, 97, 98, 99]. PSA using Artificial Neural Networks (ANN) has also been considered [100]. These analyses used measured data only. In the present chapter ANNs trained with simulated pulses are investigated for systematic uncertainties of this analysis approach.

Studies using simulated pulses are described in Section 5.1 and the application of a neural network to the GERDA data are discussed in Sections 5.2 and 5.3.

5.1 Systematic studies with simulated pulses

Events from the 2615 keV Double Escape Peak (DEP) of ^{208}Tl at 1593 keV and from the 1620 keV Full Absorption Peak (FAP) of ^{212}Bi decay were selected for the studies. At these energies the dominating process of photon interaction in the detector is Compton scattering (see Section 3.1). A scattered photon of ~ 2 MeV has a mean free path of $\mathcal{O}$(cm). In a FAP event the scattered photon is absorbed in the same detector volume. The two energy deposits will be separated in space and thus FAP events are mostly background-like MSEs. For pair creation $\gamma \rightarrow e^+e^-$ the energies of the positron and the electron are deposited locally; the two 511 keV annihilation photons can escape the sensitive volume of the detector without depositing energy. Such DEP events are dominantly SSEs and thus signal like.

For our purposes, a trained Artificial Neural Network (ANN) should be able to distinguish SSEs with the energy of 2039 keV, the $Q_{\beta\beta}$ value of ^{76}Ge, originating from the $0\nu\beta\beta$ in germanium, from MSEs. The method is based on analyzing the pulse shapes collected in HPGe germanium detectors. Background events from the Compton continuum in the region around 2039 keV should be suppressed, whereas energy depositions from $0\nu\beta\beta$ should be recognized as signal events. In previous studies ANNs were trained using two distinct pulse types, DEP events as SSEs and FAP as MSEs. The event location distribution of DEP events used in the training is however different from the one for $0\nu\beta\beta$ events. The training of an ANN is usually performed using a set of pulses with two different position distributions of energy deposits, which may influence the recognition efficiencies of the trained ANN. In this section the influence of different event position distributions on recognition efficiencies is studied.

5.1.1 Simulation and data sets

Systematic effects in pulse shape analysis using neural networks were studied by simulating photon interactions in the true-coaxial detector Siegfried-I as installed in the K1 vacuum cryostat. For details about the detector and the cryostat please refer to Section 3.5. The event and pulse simulations were performed within the MaGe framework [86].

An ANN was trained using SSE and MSE pulses for two simulated γ-source configurations with different event position distribution for SSEs:

- *Homogeneous* sets:
  - DEP events from 2.6 MeV photons. The pair creation process was forced to occur at defined points homogeneously distributed in the detector. Compton scattering and Bremsstrahlung processes were suppressed. This ensures a clean SSE set.
  - FAP: starting positions of 1620 keV photons were homogeneously distributed in a disk centered on top of the vacuum can parallel to its top surface. The photons were shot vertically downwards. Only Compton scattering and Bremsstrahlung processes were allowed.

- *Top* sets:
  - DEP events from 2.6 MeV photons. The starting positions of the photons were homogeneously distributed in a disk centered on top of the vacuum can parallel to its top surface. The photons were shot vertically downwards. Compton scattering and Bremsstrahlung processes were suppressed as in the *homogeneous* set. Only the pair creation process was allowed.
  - FAP: as in the *homogeneous* set

Each of the four sub-sets contained ~ 5000 events.

For the pulse shape simulation, for each event individual energy deposits inside the detector were combined whenever the distance between them was less than 1 mm. Pulses for the combined energy deposits were generated using the pulse shape simulation package [71] implemented in MaGe using pre-calculated electric field. The following parameters were used for the calculation of the electric field and the pulse simulation:

- Applied voltage to the detector 3 kV;
- Number of grid points for electric field calculation: $33(r) \times 181(\phi) \times 71(z)$;
- Homogeneous level of electrically active impurities of $0.63 \times 10^{10}/\mathrm{cm}^3$;
- Sampling frequency of the charge carriers drift 1125 MHz, pulses re-sampled to 75 MHz in order to represent the existing DAQ; the pulses were determined by 1125 time steps, i.e. for 1 μs [1];
- Amplifier RC-integration constant 20 ns, corresponding to a bandwidth of about 10 MHz;
- Amplifier decay time 50 μs;
- Noise according to a Gaussian distribution with $\sigma = 7$ keV applied to each individual pulse sample.

5.1.2 Event distributions of the simulated training sets

The distributions of the energy barycenters of individual events for the *homogeneous* and *top* sets are shown in Figures 5.1(a) and 5.1(b), respectively. The barycenter for SSEs approximately corresponds to the position of the pair creation. For the *homogeneous* set it is flat as was intended. For the *top* set the DEP events are typically located closer to the detector outer surface, where the annihilation photons have higher chances to escape the detector's active volume. Full absorption events tend to have their barycenter closer to the center of the bulk of the detector, where photons have higher chances to be absorbed than to escape the detector. For these, mostly multi-site events, the locations of the barycenters

[1] Such a procedure is needed to avoid large discrepancies in the drift simulation. Much lower frequencies than 1 GHz change the drift trajectories significantly. Increasing the frequency does not change the trajectories significantly. 1125 MHz was chosen as a multiplier of 75 MHz for easy re-sampling.

can be significantly different from the locations of the individual energy depositions. This explains why for the barycenter distribution of these events also values inside the bore hole of the detector ($r < 5\,\mathrm{mm}$) are allowed.

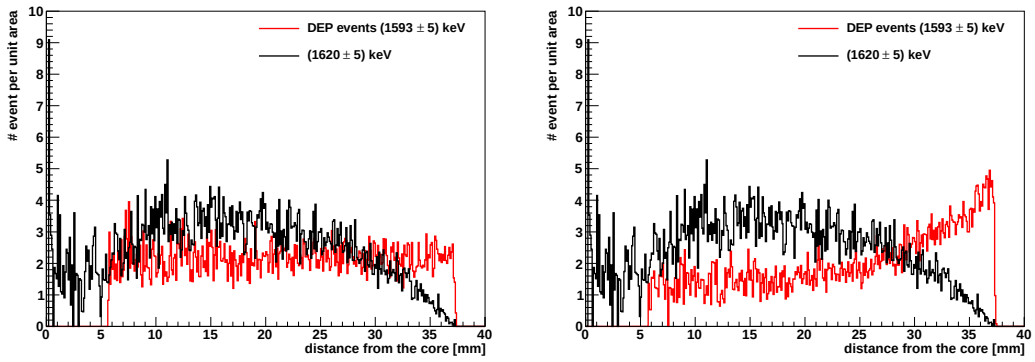

(a) (b)

Figure 5.1: Barycenter distributions of energy deposits in (a) *homogeneous* set and (b) *top* set described in the text. The distributions were normalized per unit area. The sharp peaks at $r \sim 0$ is explained by the small area of this region.

The DEP events in the *homogeneous* and *top* sets are expected to be mostly signal-like. They intentionally have different energy barycenter distributions shown in Figures 5.1(a) and 5.1(b). The distribution of the *homogeneous* DEP set coincides with the one of $0\nu\beta\beta$ events which occur at random locations within the detector. In reality it is, however, not easily possible to collect such a training dataset. Instead, a more realistic, *top* DEP set, has a significantly different event distribution. The difference in these event distributions used for the ANN training will be used to quantify the systematic uncertainties of the pulse shape analysis using ANN.

5.1.3 Neural network training

The pulse shapes of the training sets were used to train the ANN to distinguish between the typical event topologies. The amplitudes of all pulses were normalized to one. Only those parts of the pulses were used in the ANN that contain the information on the charge carrier drifts, i.e. also on the underlying event topology. A usual pulse in Siegfried-I has a 10–90 *risetime* $t_r^{10\text{–}90}$ (see Section 3.3) of about 300 ns (see e.g. [83, Chapter 11]). For a 75 MHz DAQ this corresponds to ≈ 23 time steps. To account for possible pulse length variations, a region containing 40 time steps during which pulses rose was used. The center of the region corresponded to the point where the pulse reaches 50 % of its amplitude. The charge collected on the core electrode during these 40 steps were assigned to the 40 input neurons of the ANN. One hidden layer with 40 neurons and one output neuron was set to the ANN.

The ANN was trained with pulses from two sets, DEP and FAP, separately for the *homogeneous* and *top* sets. Background-like MSEs were assigned an optimal ANN output

of 0, signal-like SSEs were assigned an optimal ANN output of 1. During the training procedure, the sets were automatically separated into two equal subsets, one for training and one for testing. The internal neurons are iteratively adjusted during training using the Broyden-Fletcher-Goldfarb-Shanno (BFGS) learning method [101].

For a trained network, the output quantity, NN, should be close to 1 for SSEs and close to 0 for MSEs. Events can be identified as signal-like if $NN > \overline{NN}$, where $\overline{NN}$ can be chosen from the rejection-acceptance plots depicted in Fig. 5.2. The MSE rejection efficiency, R, as a function of $\overline{NN}$ represents the fraction of events from the FAP set that were rejected with $NN < \overline{NN}$, whereas the values of SSE acceptance efficiency, E, represent the fraction of events from the DEP set kept with $NN > \overline{NN}$. The optimal cut value for $\overline{NN}$ is chosen to maximize the quantity $\sqrt{R \times E}$. As seen from Fig. 5.2, the dependence of R is almost linear down to the $\overline{NN}$ value of 0.2, whereas the E dependence is almost constant and drops rapidly above $\overline{NN} = 0.6$ for both *top* and *homogeneous* sets.

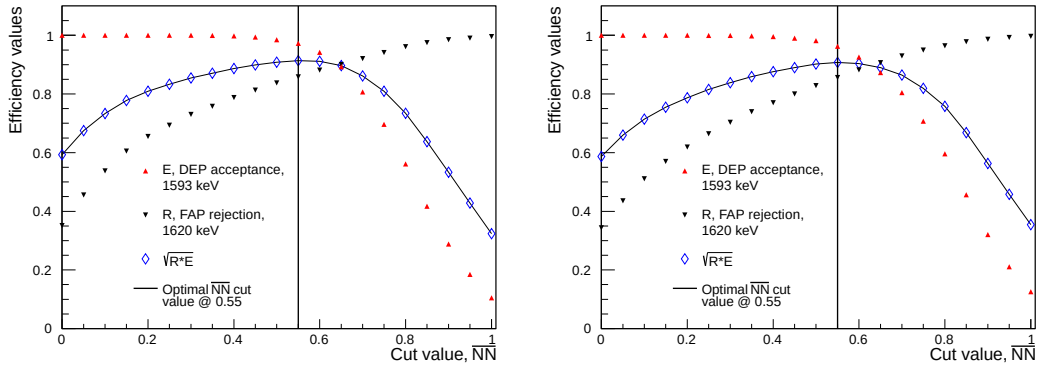

(a) (b)

Figure 5.2: SSE acceptance and MSE rejection efficiencies, E and R, respectively, as functions of the ANN cut $\overline{NN}$ for the training with (a) *homogeneous* set and (b) *top* set.

5.1.4 Results of neural network evaluation

The following simulated data sets, called evaluation sets, were used to evaluate the efficiency of the neural network cut:

A A combination of 2.6 MeV and 1.62 MeV photons irradiated in a narrow beam at $r = 17.5$ cm with a 8° aperture onto the side of the detector, facing a segment in the middle layer. All electromagnetic processes were allowed. The set contained in total ∼120.000 events of these two energies.

B A $0\nu\beta\beta$ set with homogeneous distribution of $0\nu\beta\beta$ events in the detector. The set contained 20.000 events. All electromagnetic processes were allowed. All events were selected, no energy selection was used.

The simulated pulses of the evaluation sets were normalized and centered in the same way as the pulses of the training sets. The ANN obtained from the training with the

different training sets were used to calculate the output values NN for all pulses of the evaluation sets. The *survival probability*, SP, is defined as the fraction of events of a given set surviving the cut $NN > 0.55$, i.e. categorized as SSEs. The SPs for selected peaks and energy regions and both evaluation sets are summarized in Table 5.1. The absolute statistical uncertainties are below 0.01 and therefore not considered in the following as systematic uncertainties are dominant (see below). For comparison, also the expected fractions of SSEs with $R_{90} \leq 2\,\text{mm}$ and the corresponding systematic uncertainties from the previous studies on simulation [98, 95] are listed. The values corresponding to set **A** were calculated for an identical experimental setup and a non-collimated ^{228}Th source [98], denoted below as set **A′**. The value at the last row corresponding to set **B** was calculated for the simulation used in Ref. [95]. This set will be denoted below as **B′**.

Evaluation set	Line	SSE fraction using NN cut		SSE fraction using R_{90} cut
		Homog.	*Top*	
A	DEP, $(1593 \pm 5)\,\text{keV}$:			
	for events under the Gaussian peak	0.88	0.84	
	for all events in the energy region	0.79	0.74	$0.779^{+0.016}_{-0.034}$
A	FAP, $(1620 \pm 5)\,\text{keV}$	0.12	0.11	$0.305^{+0.040}_{-0.036}$
A	$(2039 \pm 20)\,\text{keV}$ (Compton continuum)	0.43	0.40	$0.524^{+0.038}_{-0.076}$
A	FAP, $(2615 \pm 5)\,\text{keV}$	0.13	0.11	$0.122^{+0.060}_{-0.076}$
B	$0\nu\beta\beta$ peak, $(2039 \pm 5)\,\text{keV}$	0.92	0.89	$0.961^{+0.006}_{-0.025}$

Table 5.1: Surviving probabilities of selected peaks and energy regions from evaluation sets **A** and **B** for the ANN cut $NN > 0.55$. The last row for set **A** shows the expected fraction of SSEs with $R_{90} \leq 2\,\text{mm}$ and the corresponding systematic uncertainties adopted from Ref. [98]. The last column of set **B** shows the expected fraction of SSEs calculated for the simulation from Ref [95].

For set **A**, the SPs for events in the DEP region was determined as the area of a Gaussian fitted together with a linear polynomial of the respective spectra, excluding the events from the underlying background. The resulting SPs were 0.88 (0.84) for the training with the *homogeneous* (*top*) set. Both values are slightly larger than the corresponding expected fraction of SSEs by the R_{90} criteria in set **A′**, which is 0.78. The difference can be explained by the underlying "background" events, which are mostly multi-site, not taken into account for the case **A**. This is demonstrated in Fig. 5.3. By considering also these events, the SP of the events in the DEP region becomes 0.79 (0.74) for the training with the *homogeneous* (*top*) set. This is in a very good agreement with the expectation. The difference between the SPs of 0.79 and 0.74 for the two sets originates from the difference of SSE event location distributions used for the ANN training and the evaluation. An absolute systematic deviation of ± 0.05 is therefore derived for the acceptance efficiency of

the ANN due to the difference in event location distributions of the training and evaluation sets.

For the FAPs at 1620 keV and 2615 keV of set **A** the SPs were calculated as the numbers of counts under the peaks extracted from the Gaussian fits. For the FAP at 2615 keV in set **A**, the fraction of events recognized by the ANN as SSE is 0.13 (0.11) for the *homogeneous* (*top*) training set (see also Fig 5.4). This is in a very good agreement with the expected fraction of SSE by the R_{90} criteria of $0.12^{+0.06}_{-0.08}$. The 2615 keV peak does not contain a significant amount of underlying "background" events, therefore the numbers can be directly compared. The deviation between ANN rejection efficiencies at 2615 keV for the *top* and *homogeneous* sets is 0.13-0.11=0.02.

In the region of FAP at 1620 keV the SP due to the ANN cut is 0.12 (0.11) for the *homogeneous* (*top*) training set. The underlying Compton scattering events at this region were not simulated, therefore these numbers should not be compared to the expected number of SSEs from the R_{90} criteria, which is $0.31^{+0.04}_{-0.04}$ (see Fig. 5.3).

The energy region around $Q_{\beta\beta}$ in a spectrum obtained by irradiation with a ^{228}Th source contains mostly events from the Compton continuum from the 2.6 MeV photons. There are almost equal numbers of SSEs, (52^{+4}_{-8}) %, and MSEs, (48^{+8}_{-4}) %, in this region as follows from the R_{90} criteria shown in Table 5.1. The SP due to the ANN cut is 0.43 (0.40) for the *homogeneous* (*top*) training set. The specific source configurations, 2.6 MeV beam-directed photons in set **A** and the full ^{228}Th decay chain containing more photon lines in set **A′**, may be the origin of this difference. Absolute systematic deviations on both rejection and acceptance efficiencies arising from the source configuration could be as much as ±0.12. A systematic deviation between ANN rejection efficiencies for the *top* and *homogeneous* sets due to different event location distributions is however smaller, ±0.03.

The energy deposit barycenter distribution of $0\nu\beta\beta$ events is very similar to the *homogeneous* DEP training set. The SP of events in set **B** after the ANN cut reflects this. The fraction of events surviving the ANN cut for the training with the *homogeneous* set is 0.92. This value is in a reasonable agreement with the expected fraction of SSEs in set **B′**, which is $(0.961^{+0.006}_{-0.025})$. The discrepancy could be related to a small fraction of SSEs present in the FAP training set, shifting the values of NN for events in this set to higher values. The absolute deviation of ±0.04 is consistent with the difference originating from the event location distributions for the *homogeneous* and *top* training set which is ±0.03. An absolute systematic deviation due to different event location distributions of ±0.04 was derived for the acceptance efficiency.

It is instructive to look at the fraction of simulated events surviving the ANN cut at different positions in the detector. The distribution of the mean value of the NN output is depicted in Fig. 5.5 for evaluation set **B**. Regions where the mean value is significantly below 1 are clearly seen as green (color code corresponds to 0.6) and blue (color code corresponds to 0.3) areas. Similar to the distribution of the mean ANN output, the SPs exhibit the same regions in which the ANN can not clearly identify signal events as shown in Fig. 5.6. The affected area is directly related to the overall SP probability for the evaluation set listed in Table 5.1. For the optimal cut $NN > 0.55$, in 8 % of the volume for the training with the *homogeneous* training set and in 11 % of the volume for the *top* training set the ANN does not correctly identifies SSEs. This implies that using a training

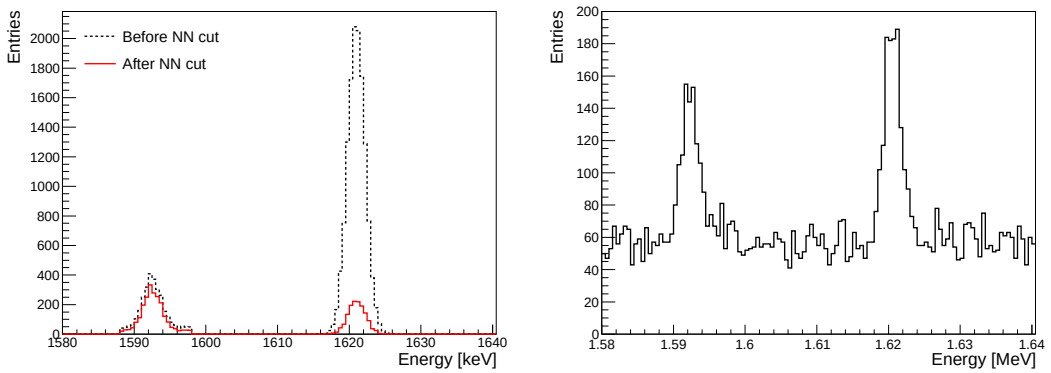

(a) (b)

Figure 5.3: (a) Effect of the neural network cut with $NN > 0.55$ on the selected energy regions of evaluation set **A**. The ANN was trained using the *homogeneous* training set. (b) A typical simulated energy spectra from a ^{228}Th source (peak count ratio and signal/background ratio not to scale).

set with similar event location distribution as for the evaluation set decreases systematic uncertainties. However, the uncertainties are not completely suppressed.

The symmetry in the pattern structures in Figs. 5.6 and 5.5 can be connected to the crystallographic symmetry of the detector. The origin of the patterns themselves are, however, not fully understood. They tend to appear close to the detector surface and in the middle of the bulk around $r \sim 22\,\text{mm}$. This can be related to pulse formation history in these regions, leading to "featureless" pulse shapes. In the regions close to the inner (outer) surface the pulse is determined mostly by the drift of holes (electrons). In the center of the bulk, electrons and holes reach the contacts at the same time. The absence of the kink in the pulse, corresponding to the time at which one type of the charge carriers reached the corresponding contact, could be the reason for poor SSE recognition capability

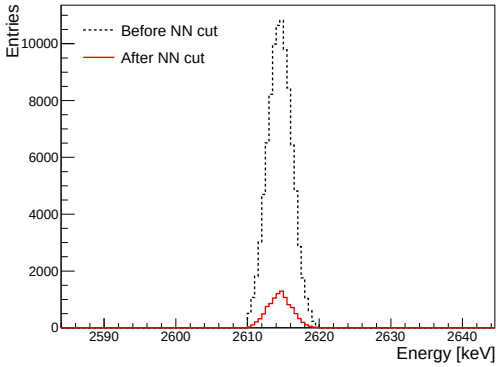

Figure 5.4: Effect of the neural network cut with $NN > 0.55$ on the selected energy region of evaluation set **A**. The ANN was trained using the *homogeneous* training set.

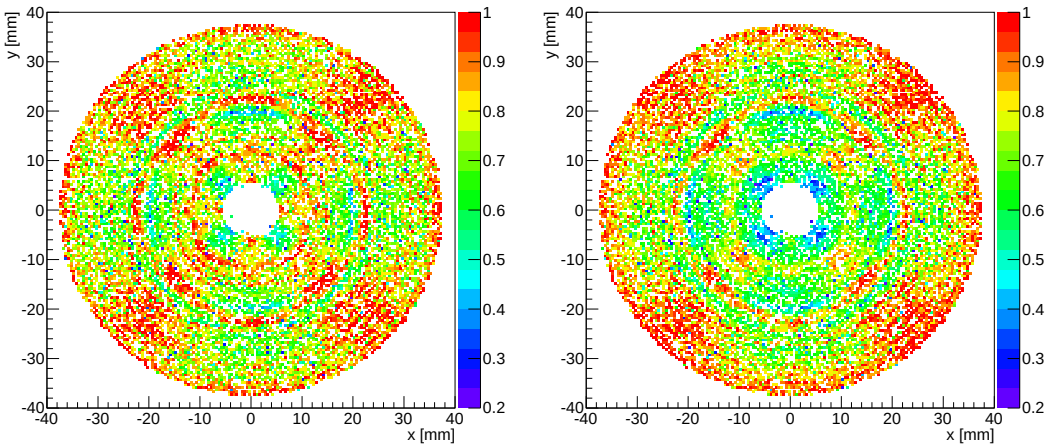

(a) (b)

Figure 5.5: Average NN output value (color palette) for $0\nu\beta\beta$ events at different positions for ANN trained with simulated (a) *homogeneous* set and (b) *top* set. If the average value in a bin was larger than 1 (smaller than 0.2), the bin content was set to 1(0.2) for better representation.

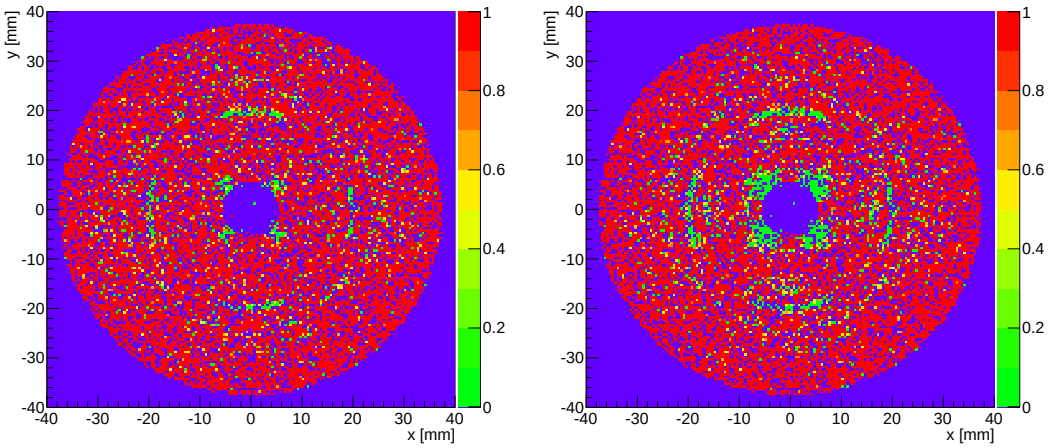

(a) (b)

Figure 5.6: Fraction of simulated $0\nu\beta\beta$ events (color palette) surviving the ANN cut $NN > 0.55$ at different event barycenter positions using the network trained with simulated (a) *homogeneous* set and (b) *top* set. The fraction is displayed by color code.

of the ANN in these regions.

Another reason could be the influence of the charge carrier drift velocities on the ANN training. The most prominent parameter that may cause this is the pulse length. The rise times of the pulses for selected training and evaluation sets vary between $\simeq$ 150 ns and $\simeq$ 350 ns, i.e. by more than a factor of two. Such a huge variation could be a reason for the neural network to prefer events of a particular topology. To study the impact of the pulse length on the results, the original pulses with the sampling frequency of 1125 MHz were stretched to all have the same 10–90 *risetimes* (see Section 3.3). After stretching the pulses they were re-sampled to 75 MHz. An ANN was trained with the *top* and *homogeneous* training sets using pulses with normalized pulse length. The maximum of the $\sqrt{R \times E}$ value is again at $\overline{NN} = 0.55$. The resulting distributions of the mean ANN output and the SPs for $NN > 0.55$ for the evaluation set **B** are shown in Figs. 5.7 and 5.8, respectively. Similar structures are still clearly visible. The affected volume in this case is 15 % for the *top* set and 8 % for the *homogeneous* set out of the total volume. The variation of the cut parameter $\overline{NN}$ leads to similar results as before. It can be concluded that the variations in pulse lengths are not the main reason for the systematically low SSE recognition efficiency at some regions of the detector.

5.1.5 Summary

The main systematic effect that was studied is the effect of difference of event location distributions in the data sets used for training and evaluation. The ANN recognition efficiency for SSEs are dependent on the location within the detector. While distinction between SSEs and MSEs is good on the outer areas, it is worse around the core and in the very center of the bulk ($r \sim 22$ mm). The overall efficiency of the ANN SSE cut is however good. For most cases the fraction of recognized SSEs in a set corresponds to the expected fraction obtained by the R_{90} criteria. The absolute systematic uncertainty on the ANN efficiency resulting from different event location distribution was estimated to be around ± 0.05. The absolute systematic uncertainty due to the volume cut is of the order of ± 0.1.

Pulse length normalization of the pulses does not show significantly different results, however it distorts the regions preferred by the ANN.

5.2 Application to GERDA calibration data

Pulse shape analysis using ANN as described in the previous section was tested on data collected with the GERDA experiment. Calibration data with three ^{228}Th sources collected in detector ANG4 during ***Run 18*** (see Section 2.2) were used to test the efficiency of the neural network to identify background-like events. Note that the detectors used in these studies are not true-coaxial as in the studies with simulation but rather closed-ended. Two calibration sets were used, one of which, collected on Aug. 17, 2011 and denoted below as *CT*, was used for training and one, collected on Aug. 23, 2011 and denoted below as *CE*, for the evaluation.

Following are the specific parameters of the data taking and the neural network:

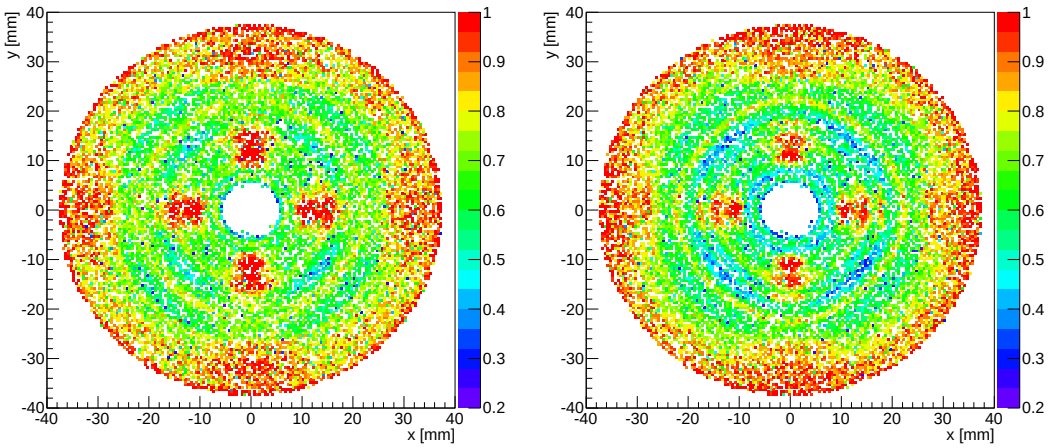

(a) (b)

Figure 5.7: Average NN output value (color palette) for $0\nu\beta\beta$ events at different positions for ANN trained with simulated (a) *homogeneous* set and (b) *top* set with the applied pulse stretching. If the average value in a bin was larger than 1 (smaller than 0.2), the bin content was set to 1(0.2) for better representation.

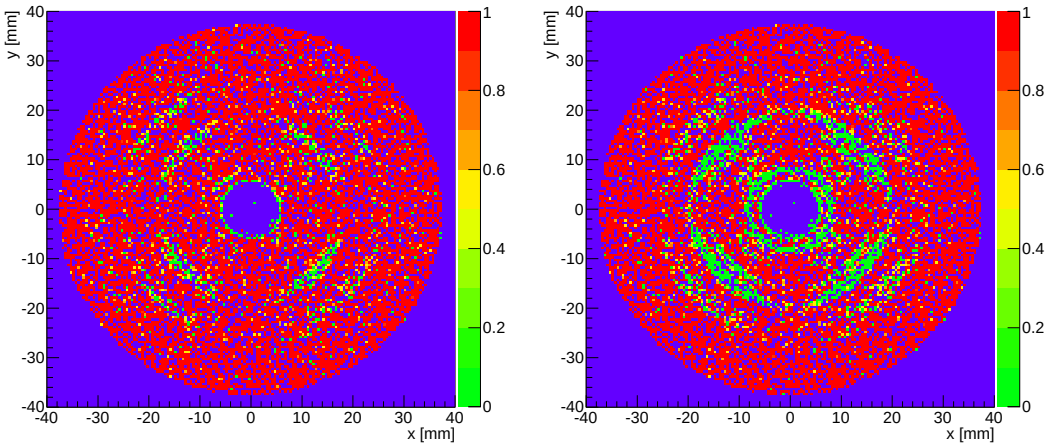

(a) (b)

Figure 5.8: Fraction of simulated $0\nu\beta\beta$ events (color palette) surviving the ANN cut $NN > 0.55$ at different positions using the network trained with simulated (a) *homogeneous* set and (b) *top* set with the pulse lengths normalized. The fraction is displayed by color code.

- Voltage applied to the detector 3000 V;
- DAQ sampling frequency 25 MHz;
- ANN scheme: 1 input layer with 30 neurons, one hidden layer with 30 neurons, one output layer with 1 neuron.

The values for the input neurons were defined as 30 individual charge pulse samples with the first sample corresponding to the point at which a pulse reached 10 % of its amplitude. Information of the pulses were extracted using the GELATIO framework [102]. In total, 1.2 μs-long regions of pulses were considered. It corresponded to the complete charge collection time of normal pulses. An example of pulse samples selected for the training is shown in Fig. 5.9. The selection of the pulse samples is different from what was used in the studies with simulated pulses. The 25 MHz sampling frequency is rather low for such a precise analysis and the pulse sample selection starting at 10 % may skip important information from pulse evolution. This was intentionally done for a first quick check of the pulse shape application to GERDA data. As will be seen later, such selection shows a slightly different ANN recognition efficiency.

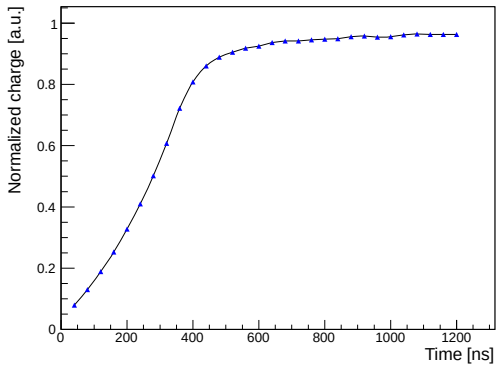

Figure 5.9: An example of 30 samples of a pulse as the input to the ANN.

DEP and FAP sets were selected from the calibration data sets for the training by the following energy cuts:

- DEP: (1593 ± 5) keV gamma line of ^{208}Tl. The set contained ≈ 700 events.
- FAP: (1620 ± 5) keV gamma line of ^{212}Bi. The set contained ≈ 900 events.

As for the simulation, during the training procedure the sets were automatically separated into two equal subsets, one for training and one for testing. Figure 5.10(a) displays the distributions of the NN values assigned to the training pulses after 500 cycles of training. The rejection and acceptance efficiencies are depicted in Figure 5.10(b). The resulting optimal value of the ANN cut is at $\overline{NN} = \max(\sqrt{R \times E}) = 0.45$. The separation capability of the neural network in this case is slightly lower than in case of the simulation. This may be due to the lower bandwidth and to the contamination of the sets, i.e. the DEP set

has an admixture of MSEs from the Compton background from higher lines, and the FAP contains some SSEs.

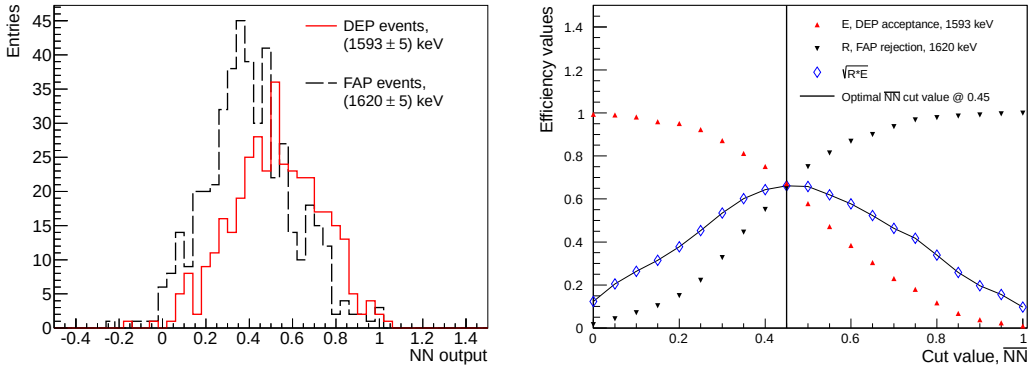

(a) (b)

Figure 5.10: (a) Output of the ANN training for the training sets of ***Run 18*** calibration data and (b) acceptance and rejection efficiencies for these training sets.

A $\overline{NN}$ value of 0.45 was used to evaluate the complete spectrum of the *CT* set. The resulting spectra before and after the ANN cut are shown in Fig. 5.11. The spectra of the *CE* set with the cut of $NN > 0.45$ is shown in Fig. 5.12. The effect of the cut on the DEP at 1593 keV and FAP at 1620 keV is demonstrated in Fig. 5.13(a) for the *CT* set and Fig. 5.13(b) for the *CE* set.

The ANN cut results in the peak counts and SPs listed in Table 5.2 for the *CT* set and in Table 5.3 for the *CE* set. The number of counts in the peak was determined by the area of a Gaussian fitted with a polynomial to the respective peak. The statistical uncertainties of the SPs represent the upper and lower limits on the mean value of the SP at a 68 % confidence level, C.L., according to Ref. [19, Chapter 33]. The efficiencies of the ANN applied to events of the DEP and FAP sets are slightly better for the *CT* set as for the *CE* set. This was expected as half of the *CT* sample being evaluated was used also for training. The rejection efficiency of MSEs does not differ within the statistical uncertainties. The SPs for the other peaks with dominantly MSEs, as well as for the Compton continuum at $Q_{\beta\beta}$, are in agreement.

The quick check of the pulse shape analysis method using ANN applied to GERDA data shows promising results, even though the pulse shape preparation was not optimized. The low bandwidth in data and possibly the suboptimal pulse preparation as well as the limited amount of pulse shapes in the training sets result in a lower efficiency of the ANN to recognize signal-like and background-like events as compared to the simulation. However, the method shows a reasonable recognition power. A more detailed and controlled pulse preparation with a decent amount of pulse shapes in the training sets is discussed in the following section.

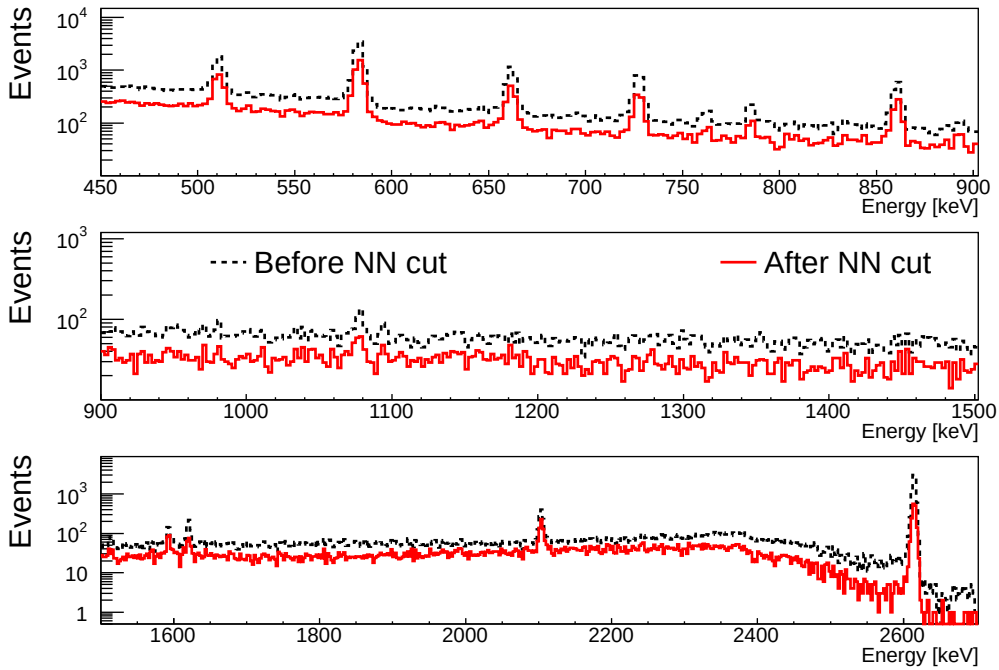

Figure 5.11: Energy spectrum of calibration with ^{228}Th sources before and after ANN cut $NN > 0.45$ for the CT set shown in the energy region (450–2700) keV. Events in the regions (1620 ± 5) keV and (1593 ± 5) keV of this data set were used for training.

Energy peak	Before the cut	After the cut	SP
DEP, 1593 keV	417	329	$0.789^{+0.020}_{-0.028}$
FAP, 1620 keV	584	172	$0.294^{+0.020}_{-0.021}$
FAP, 583 keV	11294	5079	$0.450^{+0.005}_{-0.006}$
Compton cont.,(2039 ± 40) keV	2956	1704	$0.576^{+0.009}_{-0.011}$
FAP, 2615 keV	12424	2443	$0.197^{+0.004}_{-0.004}$

Table 5.2: Number of counts before and after the ANN cut and the corresponding SPs for the evaluation of the CT set. Statistical uncertainties represent the 68 % C.L.

5.3 Application to GERDA background data

A neural network trained using GERDA calibration data with optimized bandwidth was applied to the background data. The specific parameters of the data taking and the neural network were as follows:

- Used detector: ANG3;
- Voltage applied to the detector 3500 V;

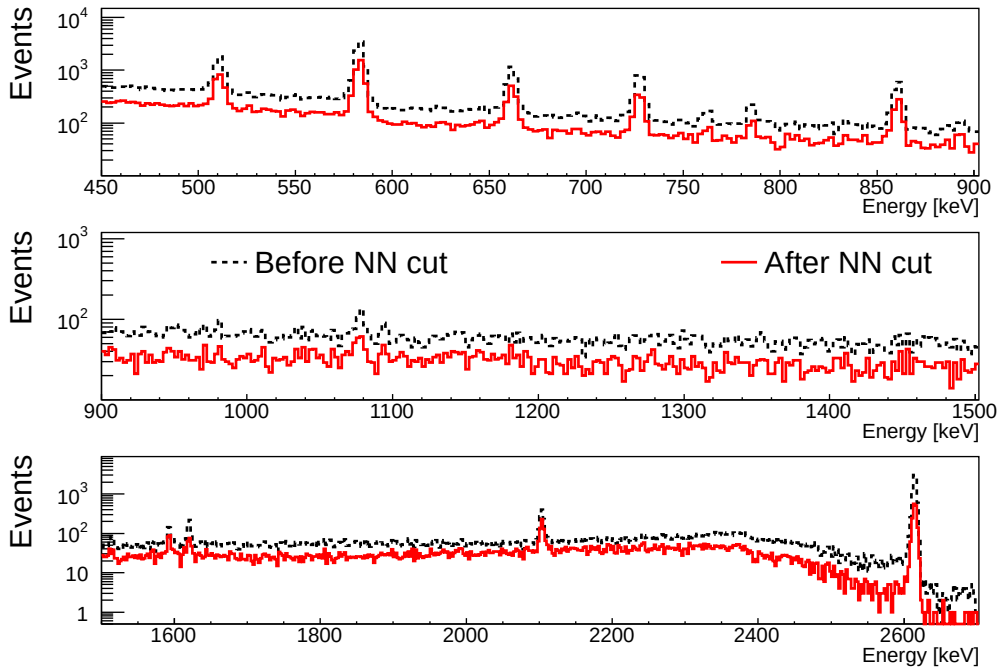

Figure 5.12: Energy spectrum of calibration with ^{228}Th sources before and after ANN cut $NN > 0.45$ for the *CE* set shown in the energy region (450–2700) keV.

- DAQ sampling frequency 100 MHz, using auxiliary waveforms available from GELATIO [102];
- ANN scheme: 1 input layer with 80 neurons, one hidden layer with 80 neurons, one output layer with 1 neuron.

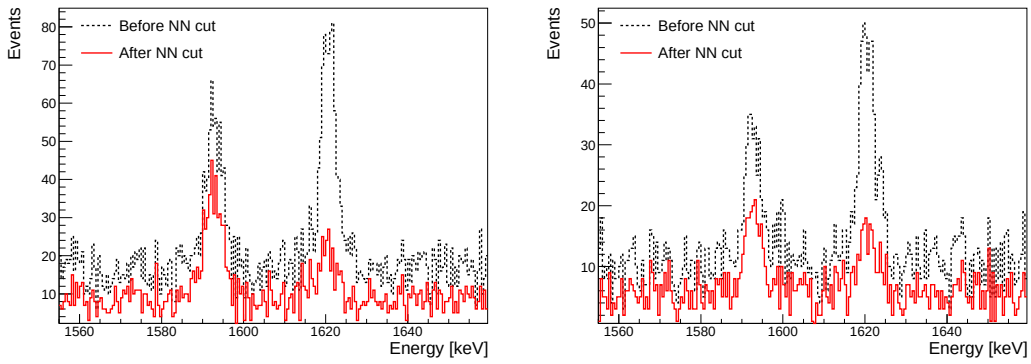

(a) (b)

Figure 5.13: The energy spectra of (a) *CT* set and (b) *CE* set around the DEP and FAP for data before and after ANN cut $NN > 0.45$.

Energy peak/region	Before the cut	After the cut	SP
DEP, 1593 keV	215	138	$0.64^{+0.03}_{-0.04}$
FAP, 1620 keV	393	119	$0.302^{+0.025}_{-0.026}$
FAP, 583 keV	6719	2981	$0.444^{+0.006}_{-0.007}$
Compton cont., (2039 ± 40) keV	1764	1011	$0.573^{+0.012}_{-0.015}$
FAP, 2615 keV	7597	1521	$0.200^{+0.005}_{-0.005}$

Table 5.3: Number of counts before and after the ANN cut and the corresponding SPs for the evaluation of the *CE* set in the selected energy regions. Statistical uncertainties represent the 68 % C.L.

The ANN was trained using the calibration data from three ^{228}Th sources collected with ANG3 during ***Runs 25*** through the middle of ***Run 30*** (see Section 2.2). The training dataset is denoted below as *CT2*. The DEP training set contained ≈ 3000 events, the FAP training set contained ≈ 3600 events. They are about five times larger than the ones used in the training described in the previous section.

The values for the input neurons were defined as 80 individual charge pulse samples. As in the studies with the simulation, the center of the input pulse corresponds to the point at which it reaches 50 % of its amplitude. In total, 0.8 μs-long regions of the pulses were passed to the ANN.

Figure 5.14 displays the results of the training after 1000 training cycles. The distributions look very similar to the ones for the ANG4 detector in ***Run 18*** shown in Figs. 5.10(a) and 5.10(b). The resulting optimal value of the ANN cut is at $\overline{NN} = 0.45$.

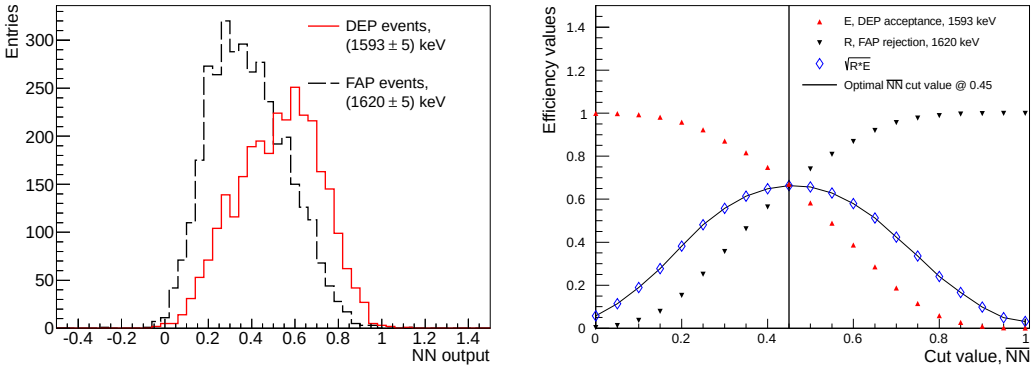

(a) (b)

Figure 5.14: Output of the ANN training using calibration data from ***Runs 26–30***: (a) output of the training for the training sets and (b) acceptance and rejection efficiencies for the training sets.

To cross-check the results of the training, the ANN was evaluated using pulses of a different calibration data set collected during ***Runs 30–31***. This set will be denoted as *CE2*. The peak counts, determined as in the previous section, and the SPs are listed in Table 5.4.

Energy peak/region	Before the cut	After the cut	SP
DEP, 1593 keV	686	571	$0.832^{+0.014}_{-0.020}$
FAP, 1620 keV	910	194	$0.213^{+0.014}_{-0.015}$
FAP, 583 keV	14667	6511	$0.444^{+0.004}_{-0.005}$
Compton cont., (2039 ± 40) keV	5276	2503	$0.474^{+0.007}_{-0.008}$
FAP, 2615 keV	20599	4966	$0.241^{+0.003}_{-0.003}$

Table 5.4: Number of counts before and after the ANN cut and the SPs in the selected energy regions. The ANN was trained with the calibration set *CT2* and applied to the calibration set *CE2*. The statistical uncertainties represent the 68 % C.L.

Table 5.5 summarizes all the survival probabilities described in this chapter. The SP for the ANN application with a 100 MHz sampling frequency (*CT2*→*CE2*) for the DEP is in a very good agreement with the expectation from the simulation despite the different geometries. However, it slightly differs from the results obtained with the 25 MHz sampling frequency. Also for the 1620 keV FAP set the rejection efficiency of the ANN is probably lower due to the lower sampling frequency for the *CE* set as compared to the *CE2* set. The effect is not observed for the FAP at 2615 keV. This cannot be explained only by the sampling frequency. For the case of training with 100 MHz calibration data(*CT2*) the ANG3 detector was used, whereas for the training with *CT* the ANG4 detector was used. They had different locations and therefore different individual exposures to the calibration sources. The discrepancy between event location distributions for 2615 keV photons, which have higher penetration power than 1620 keV photons, can explain the systematically shifted efficiency. For the FAP at 583 keV the SPs are very close to each other at ≈ 45 %, which is in between the SPs for DEP at 1593 keV and FAP at 1620 keV.

The SPs for the FAPs at 1620 keV and 2615 keV for the application to the GERDA data are higher by almost a factor of two than for the simulation. The "inverted" discrepancy for the GERDA data trained with *CT* and *CT2* in comparison to the FAP peak at 1620 keV hints for the event distributions origin for this difference. A significant difference is also observed for the Compton continuum at (2039 ± 40) keV, for which the efficiencies depend on the event location distributions as discussed in Section 5.1. Taking into account the systematic uncertainties derived earlier, the results show that PSA based on ANN is a promising tool for classification of different topologies in GERDA background data.

Energy peak	Simulation		GERDA data			
	Homog.	*Top*	*CT→CT*	*CT→CE*	*CT2→CE2*	*CT2→BgE*
DEP, 1593 keV	0.88	0.84	$0.789^{+0.020}_{-0.028}$	$0.64^{+0.03}_{-0.04}$	$0.832^{+0.014}_{-0.020}$	–
FAP, 1620 keV	0.12	0.11	$0.294^{+0.020}_{-0.021}$	$0.302^{+0.025}_{-0.026}$	$0.213^{+0.014}_{-0.015}$	–
FAP, 583 keV	–	–	$0.450^{+0.005}_{-0.006}$	$0.444^{+0.006}_{-0.007}$	$0.444^{+0.004}_{-0.005}$	–
Compton cont., (2039 ± 40) keV	0.43	0.40	$0.576^{+0.009}_{-0.011}$	$0.573^{+0.012}_{-0.015}$	$0.474^{+0.007}_{-0.008}$	–
FAP, 2615 keV	0.13	0.11	$0.197^{+0.004}_{-0.004}$	$0.200^{+0.005}_{-0.005}$	$0.241^{+0.003}_{-0.003}$	–
$0\nu\beta\beta$ peak, 2039 keV	0.92	0.89	–	–	–	–
(530–1430) keV, $2\nu\beta\beta$ dominated	–	–	–	–	–	$0.654^{+0.011}_{-0.015}$
(1490–1530) keV, ^{42}Ar FAP dominated	–	–	–	–	–	$0.41^{+0.08}_{-0.08}$
(1939–2139) keV, ROI[a]	–	–	–	–	–	$0.29^{+0.26}_{-0.18}$
(1800–2600) keV, Compton continuum[a]	–	–	–	–	–	$0.31^{+0.10}_{-0.09}$

[a] The region (2039 ± 20) keV is excluded from the analyses due to GERDA data blinding

Table 5.5: The efficiency of the neural network for selected training and evaluation sets. Listed are the survival probabilities for selected energy regions, training and evaluation sets. For simulation, the *homogeneous* and *top* training sets are applied to the set with the side position of the indicated gamma sources and the set with $0\nu\beta\beta$ events. The statistical uncertainties are below 0.01 and therefore not listed. For the GERDA data with 25 MHz sampling frequency, calibration training set *CT* is applied to the same set and different calibration set *CE*. Also, for the sampling frequency of 100 MHz, training set *CT2* is applied to different evaluation calibration set *CE2* and evaluation background data set *BgE*. The listed statistical uncertainties represent the 68 % C.L.

The ANN for the training set *CT2* was applied to the background data collected in the same detector during ***Runs 24–30***, denoted below as *BgE*. The resulting spectra before and after the ANN cut are shown in Fig. 5.15 for the energy region (0 – 2.8) MeV. The efficiency of the ANN for the selected regions of different event topology cuts is listed in Table 5.6. For the region where $2\nu\beta\beta$ signal-like SSEs are dominant, the SP is as expected significantly higher than for the energy ROI. The number of events is small and thus the uncertainties are large. Nevertheless, the trend is as expected and gives evidence that ANN can be used to distinguish background-like topologies also for GERDA background data. It has to be kept in mind, however, that the neutrino-accompanied double beta-decay events are homogeneously distributed in the detector, whereas the SSEs of the DEP used for the training are not. As described in Section 5.1, the difference in event location distributions can affect the results. For the region (2039 ± 100) keV the uncertanties on the SPs are large, therefore it is instructive to evaluate the full range of the Compton continuum from 2615 keV photons into the calculations. The SP for this region is $0.31^{+0.10}_{-0.09}$ which is better than for the Compton continuum of the calibration data. As the composition of the calibration and background in the ROI region may significantly differ, the SPs should not be directly compared.

The ANN applied to background data trained with 100 MHz calibration data results in high SPs for signal-like events and significantly lower SPs for energy regions with expectedly high ratio of MSEe. This is promising as it allows PSA based on ANN to investigate the GERDA background composition.

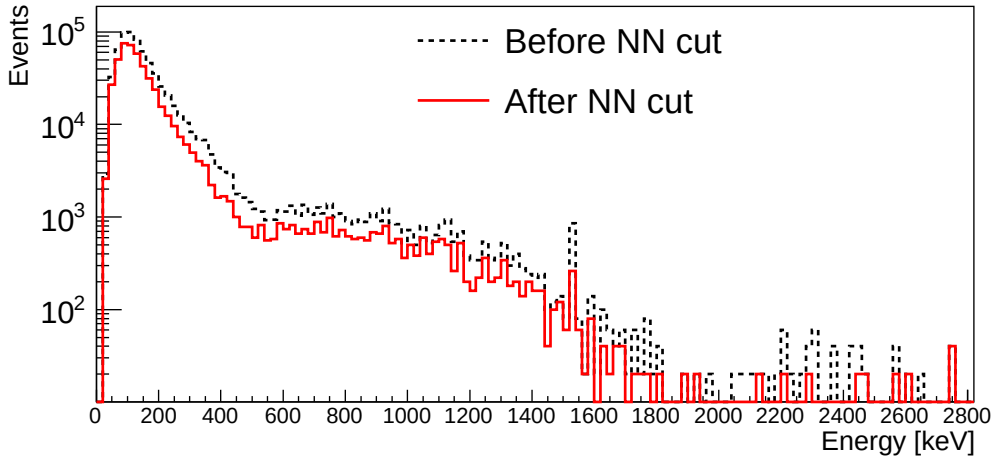

Figure 5.15: Background energy spectrum in the energy region 0–2.8 MeV taken during ***Runs 26–30*** in detector ANG4 before and after the ANN cut $NN > 0.45$.

5.4 Summary and conclusions

Several systematic effects influencing the performance of a pulse shape analysis using artificial neural networks were studied in the frame of this cooperative work. The main

Table 5.6: Number of counts and ratios in the selected energy regions. The ANN was trained with the calibration set *CT2* and applied to the background set *BgE*.

Energy region	Before the cut	After the cut	SP
(530–1430) keV, $2\nu\beta\beta$ dominated	1781	1165	$0.654^{+0.011}_{-0.015}$
(1490–1530) keV, ^{42}Ar FAP dominated	54	22	$0.41^{+0.08}_{-0.08}$
(1939–2139) keV, ROI [a]	7	2	$0.29^{+0.26}_{-0.18}$
(1800–2600) keV, Compton continuum	32	10	$0.31^{+0.10}_{-0.09}$

[a] The region (2039 ± 20) keV is excluded from the analyses due to GERDA data blinding

effect studied using simulated pulses is the difference of event distributions in the data sets used for training and evaluation. The different event distributions resulting from different positions of the radioactive sources may result in a deviation of the ANN efficiency by $\sim 10\,\%$ absolute value. This especially concerns special source configurations such as shadowing of part of the source by other materials or detectors, or collimated sources. Generally the DEP event distribution is not homogeneous thus for ANNs trained with DEP samples there will be an intrinsic bias for the application to $0/2\nu\beta\beta$ events.

It was found that the efficiency of an ANN depends on the location of events. It works well in some parts of the detector, however, SSEs in the inner regions and in the center of the bulk $r \sim 22\,\text{mm}$ are systematically misidentified. The fraction of $\sim 10\,\%$ of the volume is affected. Using training sets with homogeneous SSE location distribution reduces the effect but does not remove it. Normalization of the pulse lengths does not significantly reduce the volume cut in true-coaxial detectors. The normalization of the pulse lengths for non-true-coaxial detectors, such as closed-ended and point-contact, was not studied. It is expected to have a significant effect since pulse evolution in non-true-coaxial detectors strongly depends on the location of energy deposits. Thus, further studies are needed.

A neural network trained with events from the DEP and the FAP from GERDA calibration measurements has a survival probability for events from the spectrum dominated by neutrino-accompanied double beta-decay of 65 %. It has to be kept in mind that the systematic volume cut is reflected in this number.

An important issue in any pulse shape analysis is the presence of noise. This also applies to an ANN analysis. The pulse shapes are normalized, and therefore the ratio noise/signal changes upon the scaling, depending on the event energy. The ANN may have thus different efficiency for events of different energies. Dedicated studies of the influence of the noise are being performed.

ANNs can be used and are very useful for background evaluation, but due to limited efficiency and rather large systematics are not yet efficient for improving sensitivity, as too many signal events are cut away, thus significantly reducing the effective mass.

Studies are still ongoing and may reveal new systematic effects that may be removed or properly taken into account in the future.

Chapter 6

Temperature dependence of pulse lengths

For some applications, the shapes of the electric pulses collected on the electrodes are of interest. They are used in so called pulse shape analyses which are usually used to obtain information about event topologies [97, 98, 99]. The evolution of a pulse described in Section 3.3 depends on many parameters associated with the characteristics of the crystal and environmental conditions. The dominant parameters are the mobility, μ, of the charge carriers inside the crystal and the impurity distribution, ρ_{imp}, inside the crystal.

Two pulse shape quantities are investigated here: the pulse amplitude, A, which is proportional to the amount of charge carriers reaching the contact and the rise time of the pulse, t_r, which depends on the speed of the charge carriers.

6.1 Experimental setup

The measurements were taken using the Siegfried-II detector described in detail in Section 3.5. The detector was installed in two different setups:

- Inside K1, with a cooling finger submerged in liquid nitrogen. A collimated ^{152}Eu source was installed outside the cryostat.
- Inside the Gerdalinchen-II setup, with the detector submerged in liquid nitrogen. A collimated ^{152}Eu source was also submerged in the liquid nitrogen.

In both cases, the same collimated 75 kBq ^{152}Eu source was used inside a tungsten collimator and the $1\,\sigma$ diameters of the beamspots on the outer mantle of the detector were about 5 mm. The coordinate system used in the studies was cylindrical with the origin at the geometrical center of the detector and $\phi = 0$ along the $\langle 110 \rangle$ axis. The operational voltage of the detector was 2000 V.

The temperature inside the Gerdalinchen-II liquid nitrogen volume was constant at 77.4 K. The temperature inside K1 varied. If the nitrogen reservoir of K1 was not refilled, the detector slowly warmed up. The temperature, T_{mon}, was monitored with a thermal

resistor, PT100, mounted within K1 as close as possible to the detector. The temperature, T, of the detector was expected to be between 4–10 K higher than T_{mon}.

In total three datasets, DSs, were collected:

- DS1: detector in Gerdalinchen-II, submerged in LN2, $T = 77.4\,\mathrm{K}$;
- DS2: detector in K1, $95 < T_{\mathrm{mon}} < 100\,\mathrm{K}$;
- DS3: detector in K1, $100 < T_{\mathrm{mon}} < 120\,\mathrm{K}$.

The measurements in K1 were always started after the initial cool-down of the setup and covered the warm-up phase. For DS2, T_{mon} was measured during breaks in the data taking. The value of T_{mon} was interpolated for intermediate times. For DS3, T_{mon} at a given time was extrapolated from test warm-ups where T_{mon} was measured in one minute intervals. Figure 6.1 shows the development of T_{mon} for one measurement of DS2 and two warm-ups for DS3, one at the beginning and one at the end of the data taking.

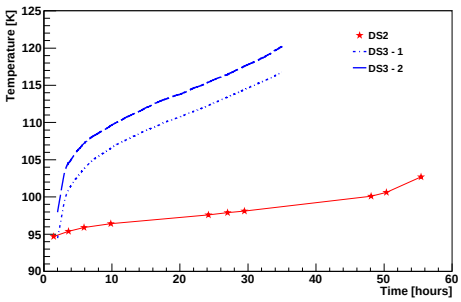

Figure 6.1: Development of T_{mon} for one of the measurements of DS2 and two test warm-ups for DS3.

Data were grouped into 15-minute intervals. For the analysis, it was assumed that T and T_{mon} were constant during these intervals. The steep rise at the beginning of the measurements in DS3 was excluded.

Measurements were taken at four different source positions, two along the crystallographic axes and two in between for cross checks. A schematic of the measurement setup is shown in Fig. 6.2.

Measurements on the $\langle 100 \rangle$ axis were impossible for DS1 due to the geometrical restrictions of the Gerdalinchen-II setup. The available datasets are listed in Table 6.1.

The core and all 18 segments, 19 channels, were read out by the Pixie-4 DAQ described in Section 3.5. Both, energies and pulse shapes were recorded for all channels.

6.2 Event selection

Pulses induced by photons from the 122 keV gamma line of ^{152}Eu were used. They were selected from the segment spectra by applying an energy cut of $122\,\mathrm{keV} \pm 2\sigma$ where the σ were determined by Gaussian+linear fits to the energy spectra. An example of a

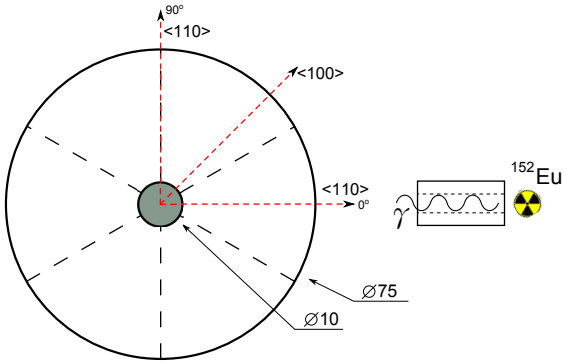

Figure 6.2: Schematic of the measurement setup. Long- and short-dashed lines indicate the segment boundaries and crystallographic axes.

	Orientation	DS1	DS2	DS3
A1	⟨110⟩	0°	0°	5°
A2	⟨100⟩	-	45°	50°
C1	⟨110⟩+5°	5°	-	5°
C2	⟨110⟩-15°	-15°	-	-15°

Table 6.1: Available data used for the analysis, A1 and A2, and for cross-checks, C1 and C2. Each row represents how the data were combined.

segment spectrum with the fit is shown in Fig. 6.3. Single-segment events were selected by requiring all other segments to show an energy below 20 keV. Typical signal to background ratios were 3:1 to 5:1 for DS2 and DS3 and 1:1 to 2:1 for DS1.

6.3 Simulated pulses

The pulse shape simulation package for true coaxial detectors described in [71, 78, 84] was used to produce simulated pulses. They were used as reference pulses for the analysis. The time dependence, $C(t)$, at the contacts was simulated. One pulse was generated for the core, inner electrode, and one for the segment, outer electrode.

The pulses were simulated for a point-like energy deposit of 122 keV at $r = 32.5$ mm, $\phi = 0°$ and $z = 0$. This point is located on the ⟨110⟩ axis, 5 mm deep inside the detector. The depth was chosen as it is the average penetration depth of 122 keV photons.

The parameters of the simulation were:

- Number of grid points for the electric field calculation: $33(r) \times 181(\phi) \times 71(z)$;
- Detector impurity level of $0.45 \times 10^{10}/\text{cm}^3$, corresponding to the specification at $z = 0$ [103];
- Sampling frequency 1 GHz, corresponding to a step size of 1 ns; the pulses were determined by 7000 time steps, i.e. for 7 μs;

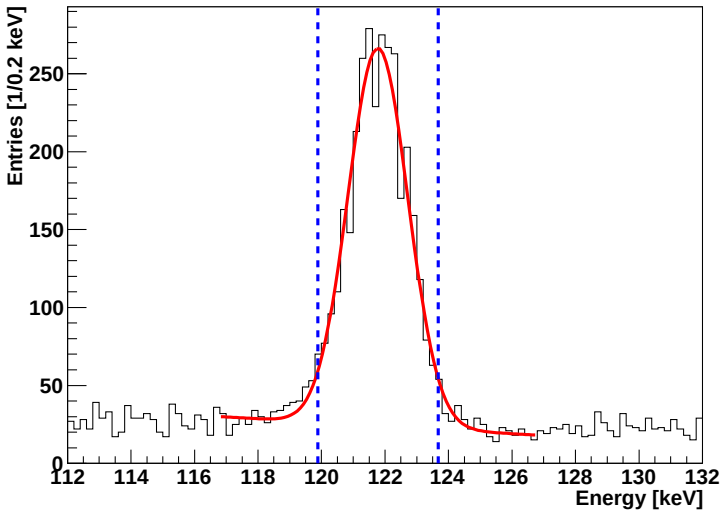

Figure 6.3: Energy spectrum as seen by the segment on the ⟨110⟩ axis being irradiated. Also shown is a fit with a Gauss function plus a first-order polynomial. The 2σ limits are shown as dashed lines.

- RC-integration constant 20 ns, corresponding to the bandwidth of about 10 MHz;
- Amplifier decay time 50 μs;
- No noise.

The simulated charge pulses, $C^{c,s}_{\text{sim}}(t)$, for the core, c, and the segments, s, are shown in Fig. 6.4. The pulses start at 100 ns. The 10–90 rise times, $t_r^{10\text{–}90}$, as defined in Section 3.3, are 290 (239) ns for the core (segment).

6.4 Model expectation

The value of the rise time can be roughly estimated using the following simple assumptions. The electric potential, $\phi(\boldsymbol{x})$, in the crystal at any point $\boldsymbol{x} = (r, \phi, z)$ is described by the Poisson equation,

$$\Delta\phi(\boldsymbol{x}) = -\frac{1}{\epsilon_0 \epsilon}\rho(\boldsymbol{x}), \tag{6.1}$$

where ϵ_0 is the dielectric constant for vacuum, $\epsilon = 16$, is the dielectric constant of germanium and $\rho(\boldsymbol{x})$ is the charge density in the bulk. For a true-coaxial detector with inner and outer radii of r_1 and r_2, the electric field, $\boldsymbol{E}(r)$, is

$$|\boldsymbol{E}(r)| = \frac{e\, n_A}{2\epsilon_0 \epsilon} r + \frac{V - (e\, n_A / 4\epsilon_0 \epsilon)(r_2^2 - r_1^2)}{r \ln(r_2/r_1)}, \tag{6.2}$$

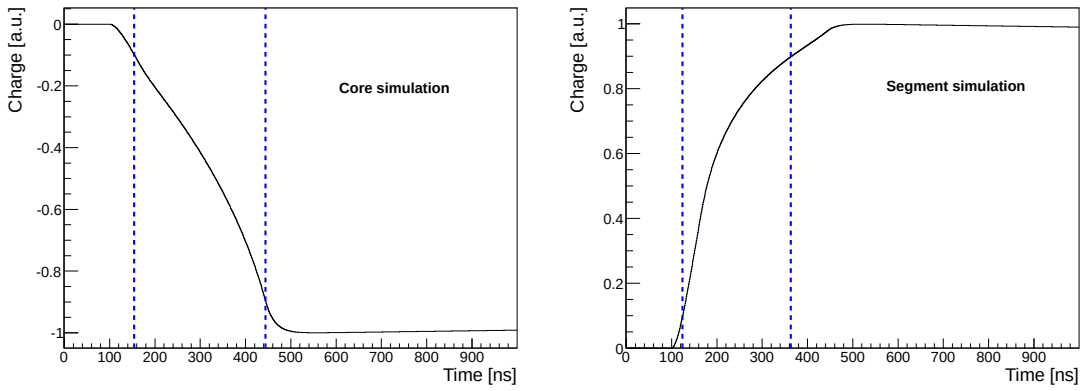

(a) (b)

Figure 6.4: Simulated pulses for (a) the core and (b) the segment. The pulse amplitudes were normalized to the absolute value of the core pulse amplitude The times at which the pulses reach 10 % and 90 % of the amplitude are indicated as dashed lines.

where e is the electron charge, n_A is the electrically active impurity concentration and V is the potential applied to the core contact. The parameters used in Eq. 6.2 were as follows:

- $r_1 = 5\,\mathrm{mm}$, $r_2 = 37.5\,\mathrm{mm}$;
- $n_A = 0.45 \cdot 10^{10}\,\mathrm{cm}^{-3}$;
- $V = 2000\,\mathrm{V}$.

The electric field in the detector for these parameters is shown in Fig. 6.5.

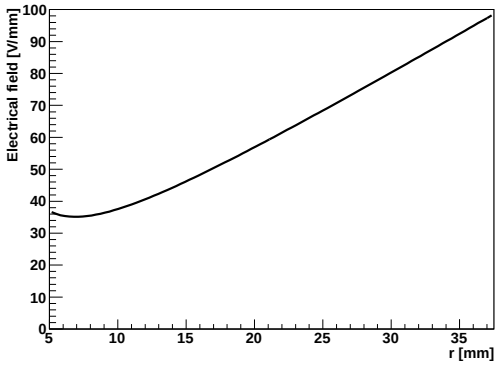

Figure 6.5: Electric field inside Siegfried-II at $z = 0$ for an applied voltage of 2kV.

As explained in Section 3.4, the drift velocity of the charge carriers for electrons and holes, $\boldsymbol{v}_e(\boldsymbol{x})$ and $\boldsymbol{v}_h(\boldsymbol{x})$, can be calculated as:

$$\boldsymbol{v}_{e/h}(\boldsymbol{x}) = \mu_{e/h}(\boldsymbol{x})\boldsymbol{E}(\boldsymbol{x}), \tag{6.3}$$

where $\mu_{e/h}$ is the mobility of the electrons/holes. For detectors operated at low temperatures, the mobility is a complex tensor and the effects of the lattice orientation have to be taken into account. Only if the electric field is parallel to any of the principal crystallographic axes, the charge carriers will follow a straight trajectory [71]. The velocities $\boldsymbol{v}_{e/h}(\boldsymbol{x})$ along the axes are approximated well for $E = |\boldsymbol{E}(\boldsymbol{x})| < 300\,\mathrm{V/mm}$ by the empirical formula from Ref. [61]:

$$\boldsymbol{v}_{e/h}(\boldsymbol{x}) = \frac{\mu^0_{e/h}\boldsymbol{E}(\boldsymbol{x})}{(1 + (\frac{|\boldsymbol{E}(\boldsymbol{x})|}{E_0})^\beta)^{1/\beta)}}, \tag{6.4}$$

where $\mu^0_{e/h}, E_0, \beta$ are parameters determined by fitting. The parameters at 77.4 K are listed in Table 6.2.

Carrier	Axis	$\mu^0_{e/h}$ $[\frac{\mathrm{cm}^2}{\mathrm{V\cdot s}}]$	E_0 $[\frac{\mathrm{V}}{\mathrm{mm}}]$	β
e	$\langle 111 \rangle$	38536	53.8	0.641
	$\langle 100 \rangle$	38609	51.1	0.805
h	$\langle 111 \rangle$	61215	18.2	0.662
	$\langle 100 \rangle$	61824	18.5	0.942

Table 6.2: Parameters for the experimental drift velocities in the $\langle 111 \rangle$ and $\langle 100 \rangle$ directions used in the simulation. Taken from Ref. [70].

As the electric field is of the same order of magnitude throughout the detector, see Fig. 6.5, formula 6.4 can be approximated as:

$$\boldsymbol{v}_{e/h}(r) = \mu^{\mathrm{eff}}_{e/h}\boldsymbol{E}(r), \tag{6.5}$$

where an effective mobility, $\mu^{\mathrm{eff}}_{e/h}$, is introduced as

$$\mu^{\mathrm{eff}} = \frac{\mu^0_{e/h}}{\left(1 + \left(\frac{E_{\mathrm{aver}}}{E_0}\right)^\beta\right)^{(1/\beta)}} \tag{6.6}$$

with $E_{\mathrm{aver}} = 70\,\mathrm{V}$ being the average value of $\boldsymbol{E}(r)$.

The measurements were done using low energy gammas, causing energy deposits located close to the surface. Therefore, the pulse shapes are defined mainly by the drift of the electrons. The parameters for electrons drifting along the $\langle 100 \rangle$ axis were taken from Table 6.2. Hence,

$$\mu^{\mathrm{eff}}_e = \mu^0_e \cdot 0.3576 = 13806.5\ \frac{\mathrm{cm}^2}{\mathrm{V\cdot s}}. \tag{6.7}$$

According to the model explained in Section 3.4, the temperature dependence of the electron mobility in germanium should be $\mu_e \sim T^{-3/2}$. This should also hold for the μ_e^{eff} parameter, i.e.

$$\mu_e^{\text{eff}} = \mu_e^T \cdot T^{-3/2}, \tag{6.8}$$

with a T-independent constant μ_e^T. The mobility measurements from [70] were carried out at $T = 77\,\text{K}$, for which μ_e^T becomes $\mu_e^{\text{eff}} \cdot T^{3/2} = 940\,\frac{\text{cm}^2\text{K}^{3/2}}{\text{V·s}}$. With the approximations of Eq. 6.5, the differential equation of motion for electrons in cylindrical coordinates becomes

$$v = \frac{dr(t)}{dt} = \mu_e^{\text{eff}} \left(\frac{e\,n_A}{2\epsilon_0\epsilon} r + \frac{V - (e\,n_A/4\epsilon_0\epsilon)(r_2^2 - r_1^2)}{r \ln(r_2/r_1)} \right) = \mu_e^T \cdot T^{-3/2} \cdot \left(Ar + \frac{B}{r} \right), \tag{6.9}$$

where

$$A = \frac{e\,n_A}{2\epsilon_0\epsilon}, \tag{6.10}$$

and

$$B = \frac{V - (e\,n_A/4\epsilon_0\epsilon)(r_2^2 - r_1^2)}{\ln(r_2/r_1)}. \tag{6.11}$$

This equation can be solved. Electrons start to drift along the electric field from the outer surface to the inner surface, yielding the boundary condition $r(t = 0) = r_2$. The solution, $t(r)$, is:

$$t(r) = \frac{\ln\left(\frac{Ar_2^2+B}{Ar^2+B}\right)}{2A \cdot \mu_e^{\text{T}} \cdot T^{-3/2}} \widehat{=} \frac{C_{\text{det}}}{\mu_e^{\text{T}} \cdot T^{-3/2}}, \tag{6.12}$$

where C_{det} is a detector-specific constant. For Siegfried-II, $C_{\text{det}} = 5.9 \cdot 10^{-3}\,\text{cm}^2/\text{V}$. Numerically, the dependence of the total rise time, $t_{\text{r,total}}^{\langle 100\rangle}(T)$ along the $\langle 100\rangle$ axis, can be expressed as

$$t(r_1, T) \equiv t_{\text{r,total}}(T) = 0.63 \cdot T^{3/2}\,[\text{ns}]. \tag{6.13}$$

The predictions of this model will be compared to the measurements in Section 6.6.

6.5 Extraction of measured pulses

The values of the parameters of measured pulses were not extracted directly due to noise that distorts the pulses, especially for low energies. To reduce the effect of noise, a simulated standard pulse was used as a reference. This pulse was taken as a template and was fitted to every measured pulse. This procedure allows the usage of the entire information of the usually 90 points of the pulse to obtain A and t_r.

The measured pulses were reconstructed as follows:

- The baseline was subtracted from each pulse; it was calculated as the average of the samples recorded for the first 200 ns. This was possible as the DAQ was always adjusted to delays larger than 200 ns;
- The noise level was determined for every measurement using the first 200 ns of several hundred baseline subtracted pulses. The noise distribution was fitted with a Gauss function, see Fig. 6.6(a); the sigma of the fit is assigned as the uncertainty to each point of the measured pulse. Typical noise levels were 3 % of the amplitude.

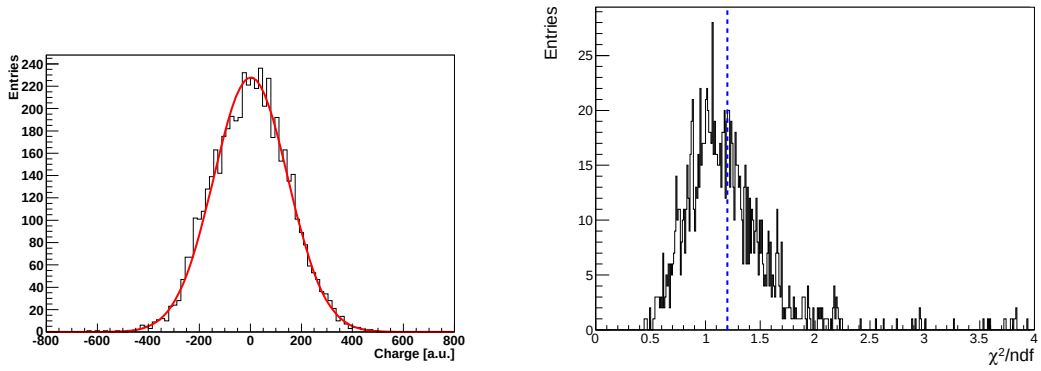

(a) (b)

Figure 6.6: (a) Typical noise level distribution in arbitrary units. Also shown is a Gaussian fit. (b) An example of the χ^2 distribution for the core for DS2. Also shown is the 50% limit, taken as the cut.

The simulated pulses were fitted to the measured pulses for core and segments as follows:

$$C^{c,s}_{\text{meas}}(t) = A^{c,s} \cdot C^{c,s}_{\text{sim}}(t/t^{c,s}_{\text{scale}} + t^{c,s}_{\text{offset}}), \tag{6.14}$$

where $C^{c,s}_{\text{sim}}(t)$ is the function describing the simulated pulse.
The fit had three parameters:

- the relative amplitude, $A^{c,s}$;
- the time scaling factor, t_{scale};
- the time offset, t_{offset}.

The fitted $t^{c,s}_{\text{scale}}$ parameters were used to calculate the 10–90 rise times of the core and segment pulses. Only good fits were considered. A fit was qualified as good, if $\chi^2/\text{ndf} \leq \chi^2_{c,s}$, where $\chi^2_{c,s}$ was adjusted for each dataset. The values of $\chi^2_{c,s}$ were set to reject 50% of the pulses assuming as this was the worst rate of background events. They were set to 1.1(2.0) for DS1, 1.2(1.7) for DS2 and 1.7(1.9) for DS3 for the core(segment). An example of the χ^2 distribution and the cut is shown in Fig. 6.6(b). Figure 6.7 shows two events with good and bad fits for both core and segment pulses.

A bad fit could indicate that the interaction point was not close to the outer mantle, or the event topology did not correspond to the simulated pulse. Unwanted topologies are, for example, photons associated with the Compton background, or multiple interactions, resulting in pulses with extra kinks. The pulses shown in Fig. 6.7(b) seem to have extra kinks, however this could also be due to too much noise.

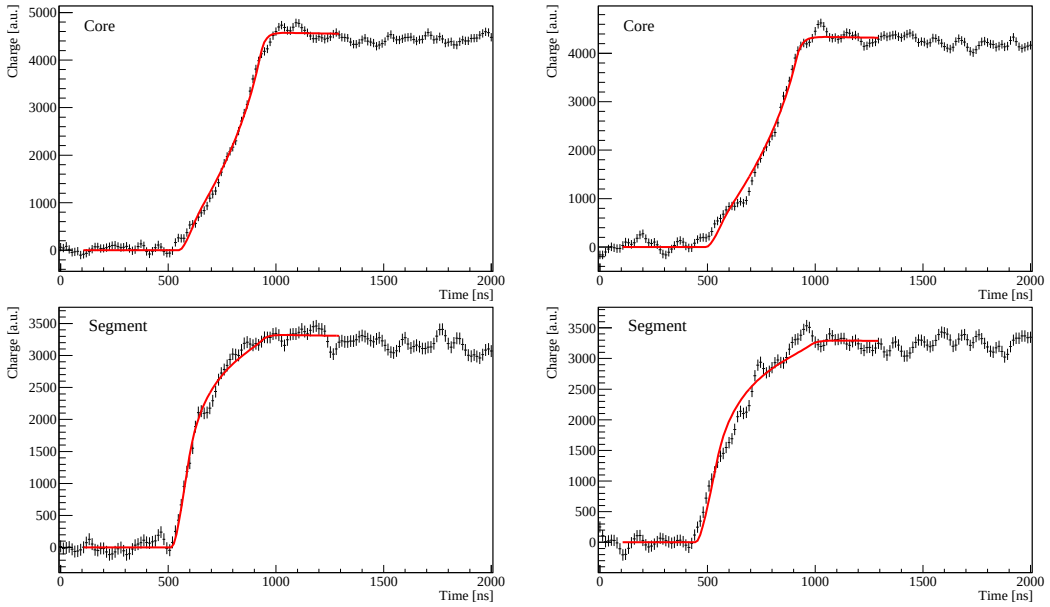

(a) $\chi^2/\text{ndf} = 1.47(1.31)$ for the core(segment) (b) $\chi^2/\text{ndf} = 2.64(2.96)$ for the core(segment)

Figure 6.7: Measured pulses in the core and the segment of a typical event from DS3 at $T_{\text{mon}} = 100\,\text{K}$. Also shown are the fits with the simulated pulses: a) good fit, b) bad fit.

After applying the fitting procedure to each measured pulse and the χ^2/ndf cut, the t_{scale} distribution was fitted with a Gauss function. The $t^{c,s}_{\text{scale}}$ distributions with the fits at different temperatures and source positions are shown in Figs. 6.8 – 6.10. The data of the different DSs were collected under different conditions and with different noise levels. Therefore, the widths of the distributions are slighly different. The core signal usually has a lower level of noise and thus the distributions for the core are narrower than for the segments.

6.6 Results

The fitted mean of the $t^{c,s}_{\text{scale}}$ distributions, $t^{c,s}_{\text{scale-mean}}$, were used to evaluate the temperature dependence of the rise times. The values of $t^{c,s}_{\text{scale-mean}}$ at selected temperatures are listed in Table 6.3. These values at different T_{mon} were used to reconstruct the 10–90 rise times, $t_{\text{r}}^{10\text{–}90}(T)$, using the definition of the scaling factor:

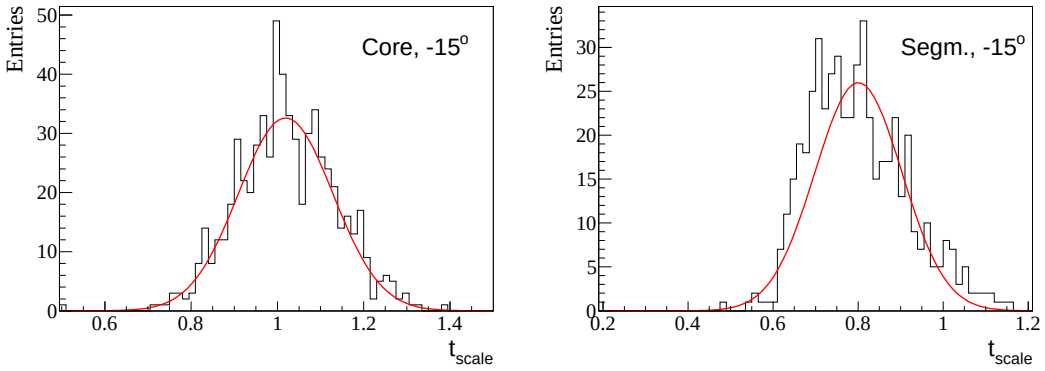

(a) -15°

(b) -15°

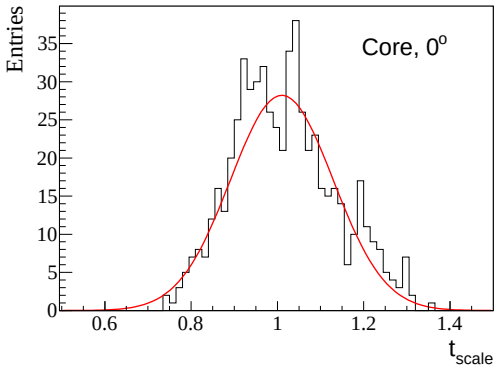

(c) 0°, ⟨110⟩

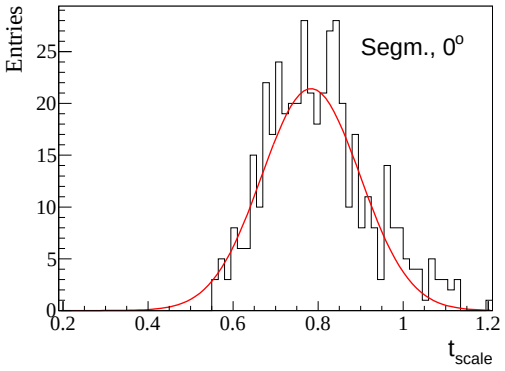

(d) 0°, ⟨110⟩

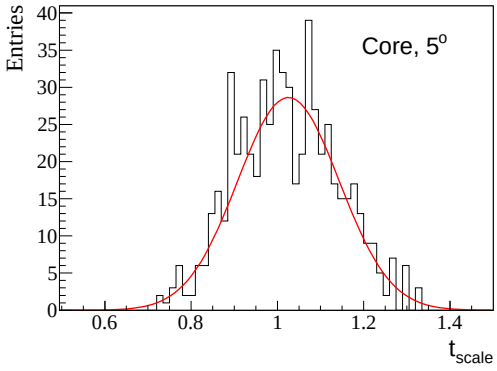

(e) 5°

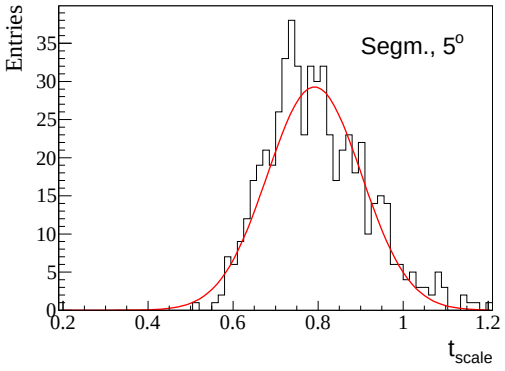

(f) 5°

Figure 6.8: The t_{scale} distributions and the fits for DS1 at $T_{\mathrm{mon}} = 77\,\mathrm{K}$.

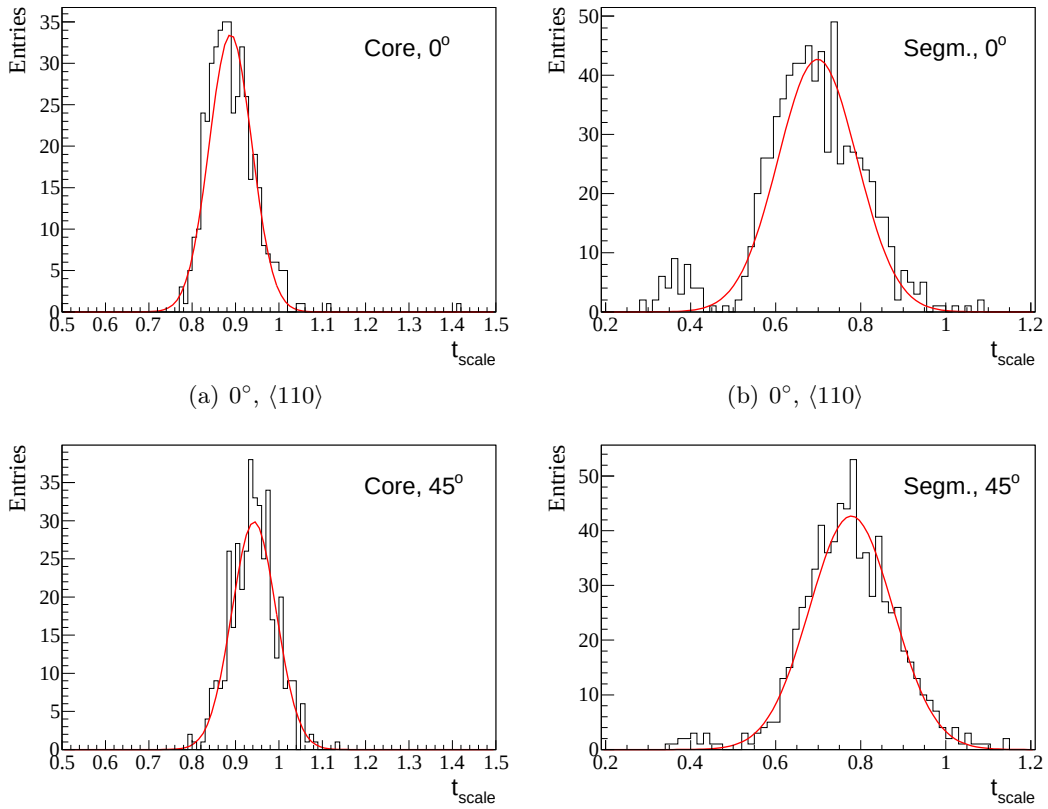

(a) 0°, ⟨110⟩ (b) 0°, ⟨110⟩

(c) 45°, ⟨100⟩ (d) 45°, ⟨100⟩

Figure 6.9: The t_{scale} distributions and the fits for DS2 at $T_{\text{mon}} = 96\,\text{K}$

Orientation	**DS1** 77 K	**DS2** 96 K	**DS3** 105 K
⟨110⟩-15°	1.019	-	0.810
⟨110⟩	1.010	0.889	0.813
⟨110⟩+5°	1.026	-	0.813
⟨100⟩	-	0.943	0.809

(a) Core

DS1 77 K	**DS2** 96 K	**DS3** 105 K
0.801	-	0.663
0.783	0.699	0.654
0.791	-	0.654
-	0.778	0.656

(b) Segment

Table 6.3: The $t^{c,s}_{\text{scale-mean}}$ values for selected T_{mon}.

$$t_{\text{r}}^{\text{meas:10–90}} = \frac{t_{\text{r}}^{\text{sim:10–90}}}{t_{\text{scale-mean}}}, \tag{6.15}$$

both for the core and the segment. Here "sim" and "meas" were added to distinguish the simulated and measured rise times, respectively. The values of the extracted $t_r^{c,s:10–90}$ corresponding to Table 6.3 are listed in Table 6.4.

The data were combined to fit the temperature dependence of the risetimes. Contrary

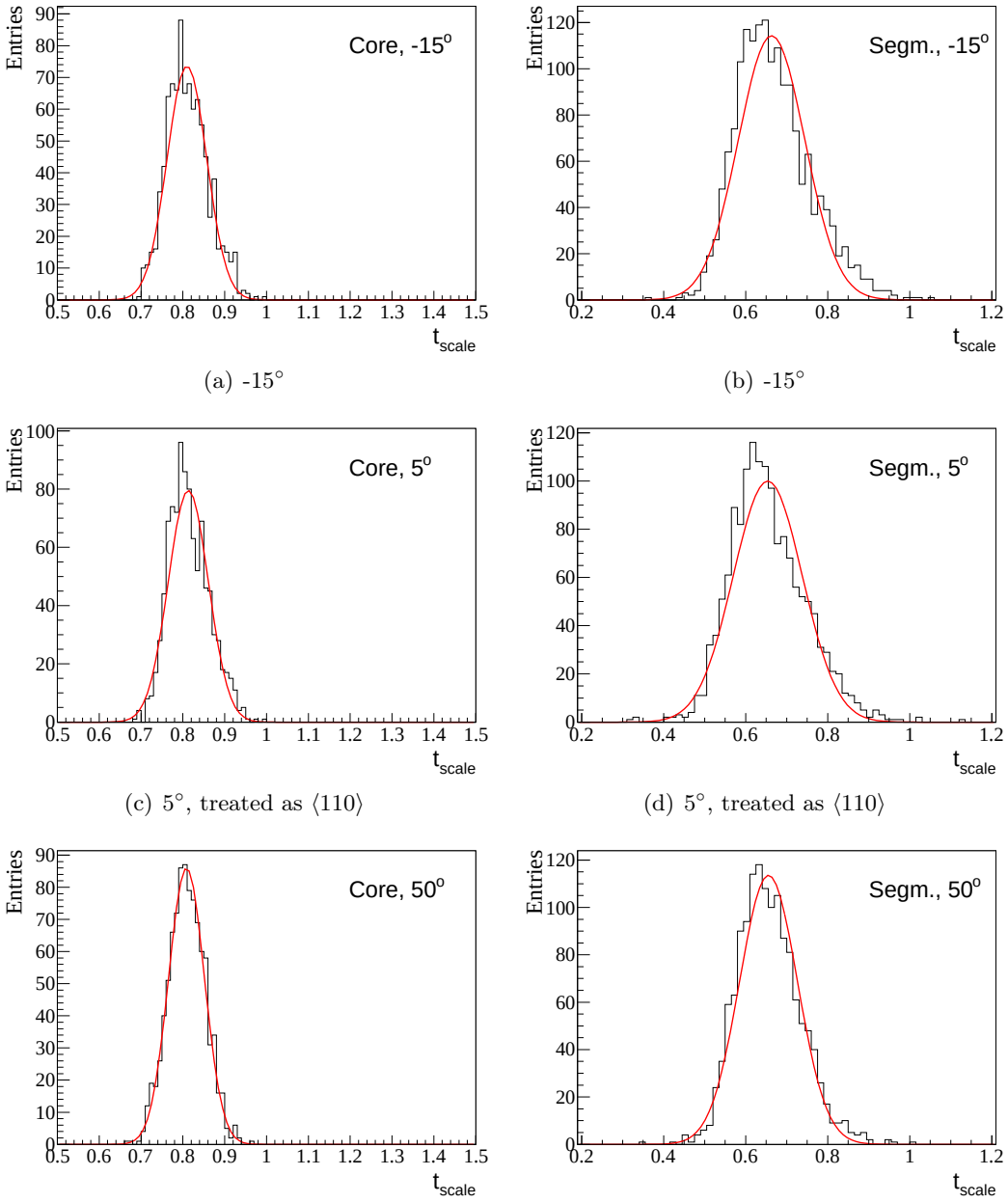

(a) -15°

(b) -15°

(c) 5°, treated as ⟨110⟩

(d) 5°, treated as ⟨110⟩

(e) 50°, treated as ⟨100⟩

(f) 50°, treated as ⟨100⟩

Figure 6.10: The t_{scale} distributions and the fits for DS3 at $T_{\text{mon}} = 105\,\text{K}$

Orientation	**Sim.** 77 K	**DS1** 77 K	**DS2** 96 K	**DS3** 105 K
⟨110⟩-15°	288	285	-	354
⟨110⟩	290	287	327	358
⟨110⟩+5°	290	283	-	358
⟨100⟩	276	-	308	353

(a) Core

Sim. 77 K	**DS1** 77 K	**DS2** 96 K	**DS3** 105 K
234	299	-	358
239	305	344	369
239	302	-	369
223	-	307	350

(b) Segment

Table 6.4: Extracted $t_{\mathrm{r}}^{c,s:10\text{–}90}$ in nanoseconds at selected temperatures.

to expectations, it was impossible to get a good fit of the data with a $T^{3/2}$ or any other power function. Instead, a Boltzmann-like fit function, $p_0 + p_1 \cdot \exp(-p_2/T)$, yielded reasonable results, even though the fit did not describe the data perfectly. As explained in Section 6.1, only T_{mon}, not T itself, is known for DS2 and DS3. Therefore, free parameters $\Delta T_{2,3} = T_{\mathrm{mon}} - T$ were introduced to the fits for DS2 and DS3. The parameters $\Delta T_{2,3}$ were between 4 and 10 K, all within the expected range. They were extracted by fitting $t_{\mathrm{r}}^{10\text{–}90}$ for different $\Delta T_{2,3}$ and minimizing $\chi^2(\Delta T_2, \Delta T_3)$ of the fits.

The fitted temperature dependences of the 10–90 rise times for all the DSs are shown in Figs. 6.11 and 6.12. The values of χ^2/ndf for the best fit were 4 to 6.5 (2 to 3) for the core (segment) fits. The typical values of χ^2/ndf were above 200 (25) for the core (segment) for any fits with $p_0 + p_1 \cdot T^{-3/2}$. For comparison, the predictions from Section 6.4 are also shown in Figs. 6.11 and 6.12. The predictions were calculated for the total rise time and only along one axis, ⟨100⟩. The values were adjusted for off-axis positions and for 10–90 rise times using the simulated pulses described in Section 6.3.

The model expectation was that the T dependence of the rise time would be $T^{3/2}$ for both axes. The fits with a Boltzmann-like function indicate that the rise time along the "slow" axis, ⟨110⟩, increases not as fast with T as for the "fast" axis, ⟨100⟩. At some temperature, $T \gtrsim 110$ K, the rise time along the "fast" axis, ⟨100⟩, becomes as large as along the "slow" axis.

The temperature dependence of the pulse amplitude was also investigated. The amplitude only depends on the number of charge carriers collected on the contacts of the detector, i.e. on the charge collection efficiency. Figures 6.13 and 6.14 show the amplitude of the pulses as a function of T. It indicates that the charge collection is not affected significantly by the temperature in the range of 95–130 K.

6.7 Discussion

The simple model prediction introduced in Section 6.4 does not describe the data at all. It correctly predicts the value at 77.4 K, at which temperature the input parameters for the simulation were measured, but the predicted T dependence is not observed in the data. In general, a form $t_{\mathrm{r}}(T) = a_0 + a_1 \cdot T^{a_2}$ as expected from Section 3.4, does not describe the data well. However, the Boltzmann-like *ansatz* describes the data quite accurately.

The parameters of the Boltzmann *ansatz* were determined from the fit using MINUIT

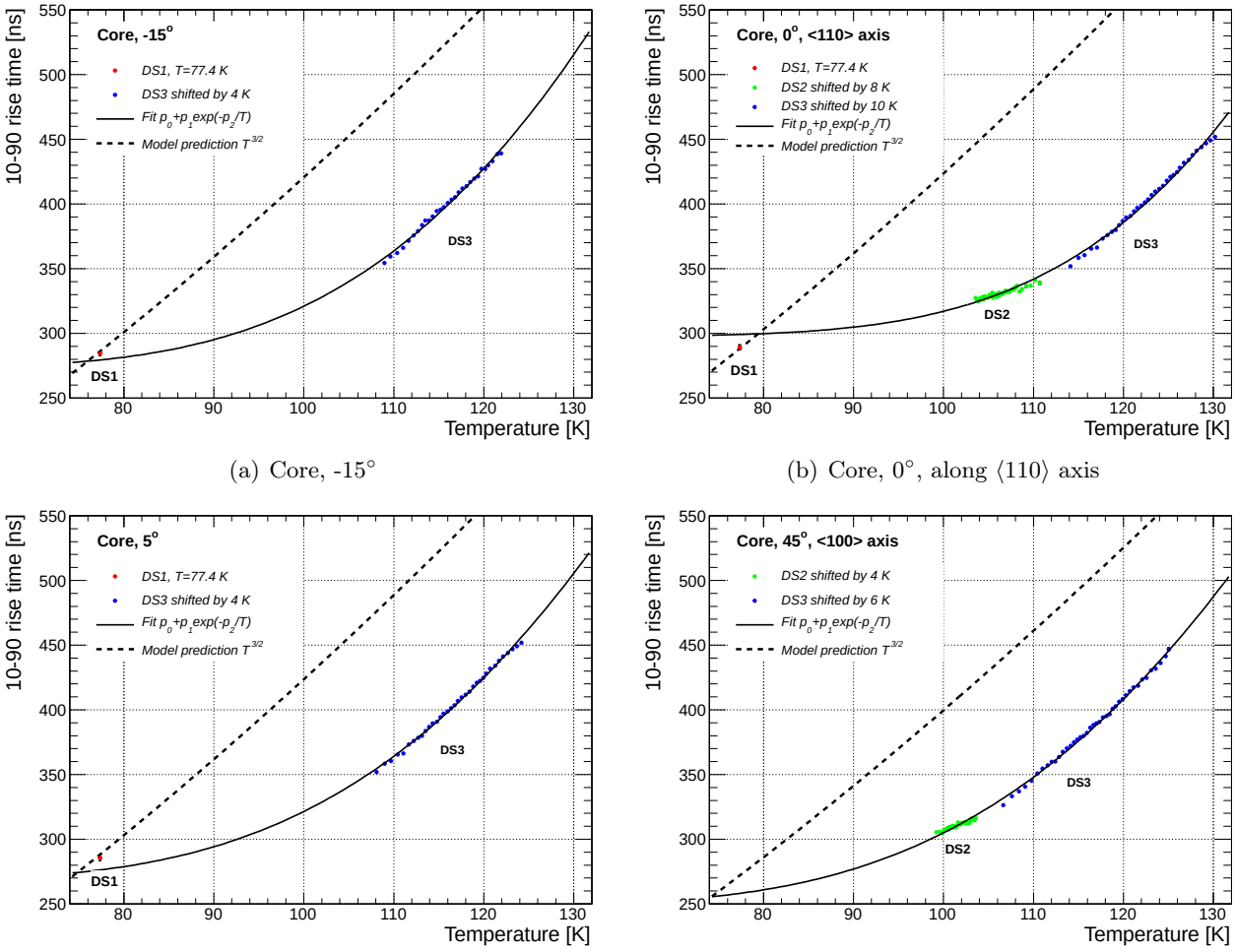

(a) Core, -15°

(b) Core, 0°, along ⟨110⟩ axis

(c) Core, 5°

(d) Core, 45°, along ⟨100⟩ axis

Figure 6.11: Dependence of the core rise time on temperature. Also shown are Boltzmann-like fits $p_0 + p_1 \cdot e^{-p_2/T}$ and the model prediction of $T^{3/2}$. Statistical uncertainties are smaller than the marker size.

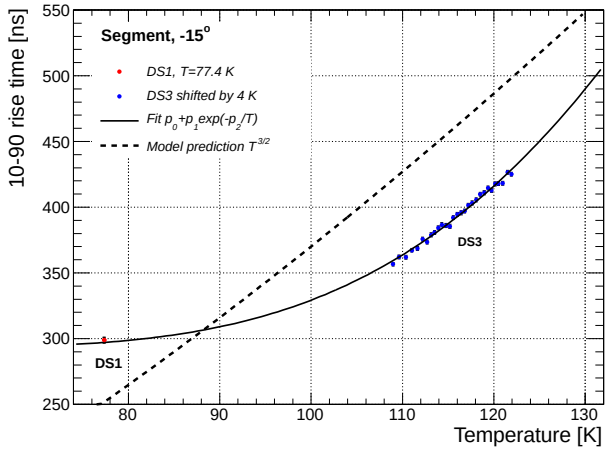

(a) Segment, -15°

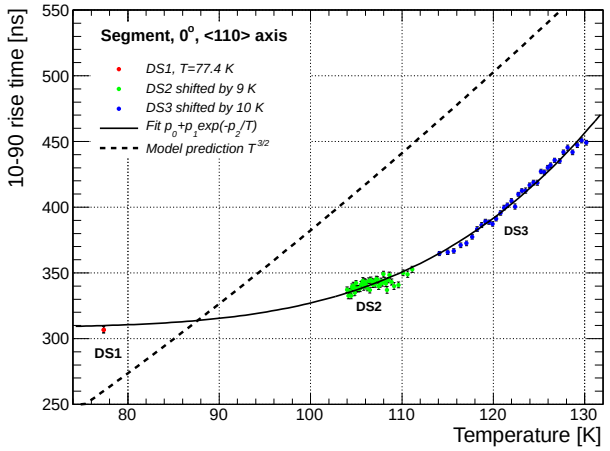

(b) Segment, 0°, along ⟨110⟩ axis

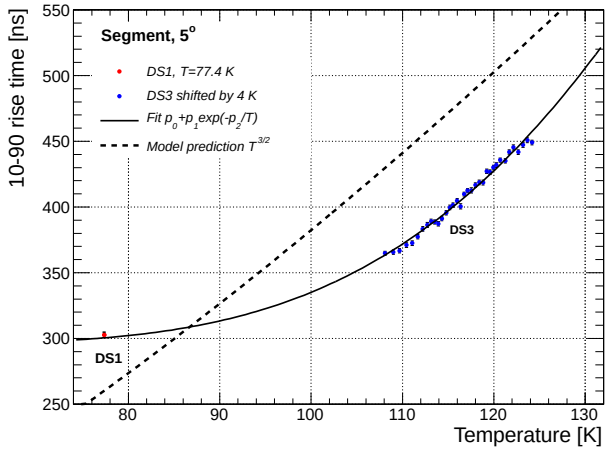

(c) Segment, 5°

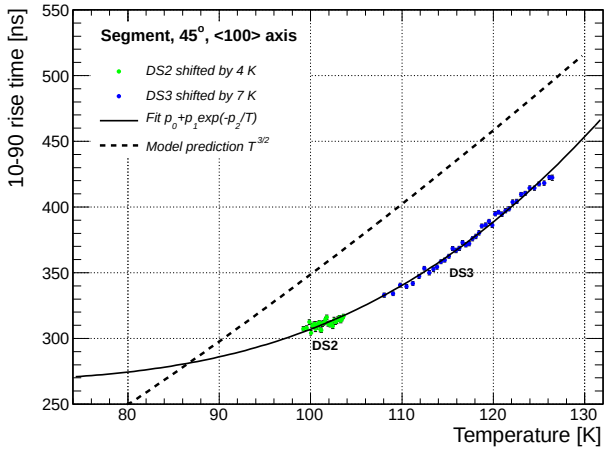

(d) Segment, 45°, along ⟨100⟩ axis

Figure 6.12: Dependence of the segment rise time on temperature. Also shown are Boltzmann-like fits $p_0 + p_1 \cdot e^{-p_2/T}$ and the model prediction $T^{3/2}$. Statistical uncertainties are shown, but are mostly smaller than the marker size.

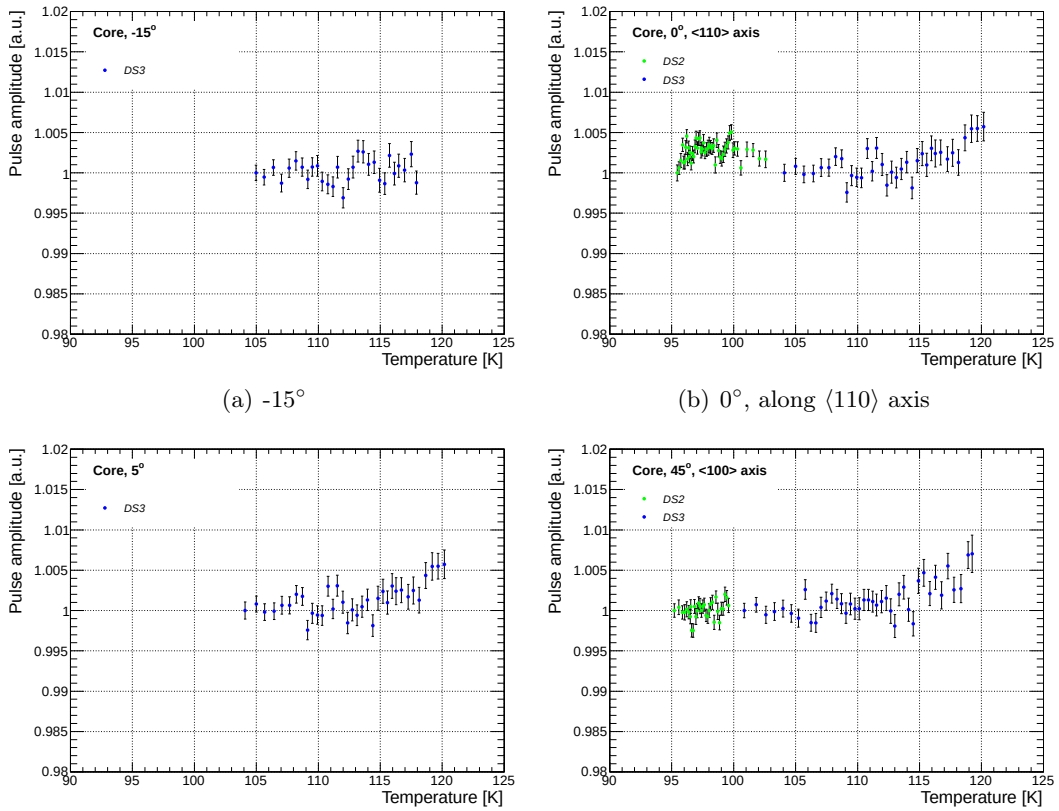

(a) -15°

(b) 0°, along ⟨110⟩ axis

(c) 5°

(d) 45°, along ⟨100⟩ axis

Figure 6.13: Pulse amplitude versus temperature at the core contact. The amplitudes were normalized such that the first measurement of each DS is set to 1.

as a part of ROOT. Table 6.5 lists the values of p_1 and p_2 from the fit. The values for p_2 are also shown as energies, E, with $p_2 = E/(2k)$, where k is the Boltzmann constant. The parameters for the segment and the core at the same source orientation agree within the statistical uncertainties. However, they seem to be significantly different for the two axes. The inclusion of DS2 to the ⟨110⟩ fit is what pushes the values of p_1 and p_2 up. The resulting systematic uncertainty on E was estimated to be $\approx 40\,\text{meV}$. The systematic uncertainty could also be connected to the misalignment present in DS3, even though such a strong deviation is not expected for a 5° offset.

The parameters p_1 and p_2 are strongly correlated. This is clearly seen from the probability density map in the parameter space obtained with the Bayesian Analysis Toolkit (BAT) [104]. Examples of the probability density functions (PDFs) and parameter correlation plots for the core are shown in Fig. 6.15 for 0° which includes all the DSs. The PDF integrated over p_0 shown in Fig. 6.15(c) clearly indicates a correlation between p_1 and p_2. As can be seen, the correlation causes the fit to be dependent on the initial values for the parameters when fitting in the global mode. The correlation between the parameters p_1 and p_2 almost does not depend on the DSs included in the fit, which were only DS1

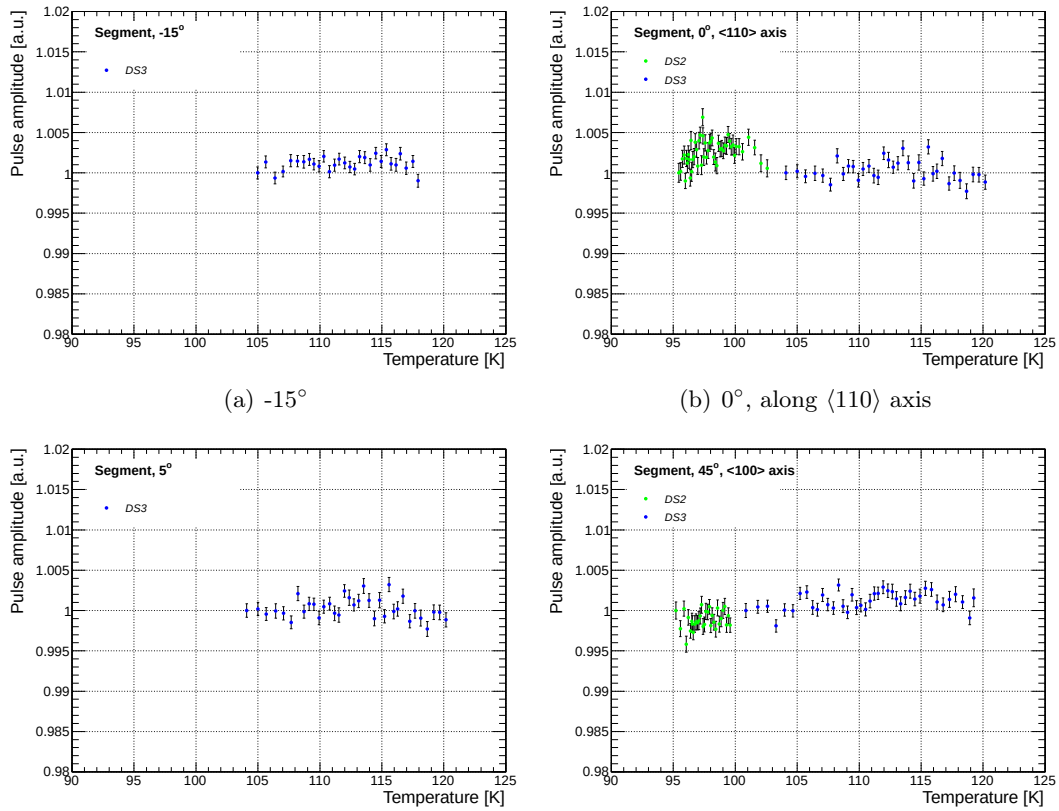

(a) -15°

(b) 0°, along ⟨110⟩ axis

(c) 5°

(d) 45°, along ⟨100⟩ axis

Figure 6.14: Pulse amplitude versus temperature at the segment contact. The amplitudes were normalized such that the first measurement of each DS is set to 1.

Orientation	p_1 [$\cdot 10^4$ ns]	p_2 [K]	E [meV]
⟨110⟩-15°	5.5 ± 0.5	705 ± 13	122 ± 2
⟨110⟩	17.7 ± 1.3	913 ± 10	158 ± 2
⟨110⟩+5°	3.5 ± 0.3	649 ± 12	112 ± 2
⟨100⟩	3.0 ± 0.2	630 ± 8	109 ± 2

(a) Core

p_1 [$\cdot 10^4$ ns]	p_2 [K]	E [meV]
5.5 ± 0.9	732 ± 22	126 ± 4
15.0 ± 2.3	900 ± 20	155 ± 4
5.6 ± 0.7	725 ± 18	125 ± 3
3.1 ± 0.4	666 ± 18	115 ± 3

(b) Segment

Table 6.5: Fit parameters determined for a Boltzmann-like *ansatz* along different crystallographic axes.

and DS3 at 5° and only DS2 and DS3 at 45°. The results from BAT in the global mode correspond to the results from MINUIT.

The success of the Boltzmann-like *ansatz* can be connected to a change in conductivity of germanium [105] in the considered T ranges. The detector was operated relatively closely to the full depletion voltage. If in these conditions the level of electrically active impurities has a slight dependence on temperature, the electric field may change signifi-

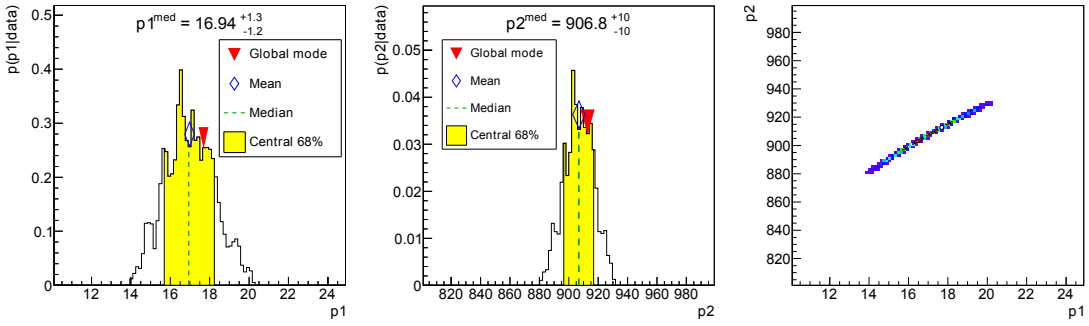

(a) (b) (c)

Figure 6.15: Probability density functions of (a) p_1, (b) p_2 and (c) $p1$ vs p_2 for the core at 0°.

cantly. To check that, the theoretical model was modified to accommodate this and other possible effects by introducing a possible T dependence of the parameters C_{det} and μ^{eff}. Formulas 6.8 and 6.12 were replaced by

$$t(r) = t_r^{T=0} + \frac{C_{\text{det}}(T)}{\mu^{\text{eff}}(T)}. \tag{6.16}$$

Different T dependencies of μ^{eff} and the detector constant C_{det} were tested according to Table 6.6(a) by adding the four fit parameters, $P_0..P_3$. The rise time $t_r^{T=0}$ was introduced as a T-independent component to represent possible effects at low temperatures, $T \sim 0\,\text{K}$. The model however does not extend to 0 K. The concentration of charge carriers in $C_{\text{det}}(T)$, $n_A(T)$, represents a possible first-order change in conductivity with temperature. A general power law of $\mu^{\text{eff}}(T)$ stands for possible models of mobility dependence on temperature. The superscript "init" stands for the initial values of the corresponding parameters used in the original model.

Parameter	Notation
Baseline $t_r^{T=0}$	P_0
n_A in Eqs. 6.10–6.12	$n_A^{\text{init}} \cdot (1 + P_1 \cdot T)$
Mobility μ^{eff} in Eq. 6.8	$P_2 \cdot \mu^{T,\text{init}} \cdot T^{-P_3}$

(a)

Fit parameter	Value	Uncert.
P_0 [ns]	250	0.7
P_1 [1/K]	$1.7 \cdot 10^{-3}$	$4 \cdot 10^{-6}$
P_2 [unitless]	14	0.2
P_3 [unitless]	3.6	0.03

(b)

Table 6.6: (a) Parameters introduced to fit the data; the superscript "init" stands for initial values used in the model. (b) Values of the parameters from a fit at the angle 0°, along ⟨110⟩ axis.

With the fit parameters given in Table 6.6(b) a reasonable description of the data is possible as shown in Fig. 6.16 for the core at 0°, ⟨110⟩ axis. The value of χ^2/ndf was 6.2.

For comparison, for the fit with a Boltzmann-like function, χ^2/ndf was 5.2.

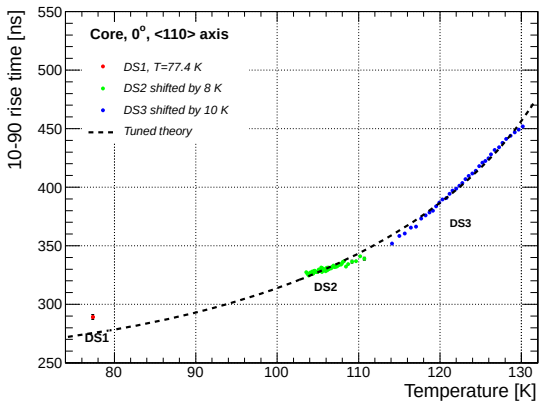

Figure 6.16: Dependence of the core rise time on temperature at 0°, along ⟨110⟩ axis. Also shown is the modified theory described in the text.

The values of the parameters P_2 and P_3 in formula 6.16, i.e. the mobility value and its temperature dependence, could be extracted if more precise measurements were available. The currently available data only yield fit parameters with high uncertainties. In addition, the resulting parameters are highly correlated.

6.8 Summary

A clear temperature dependence of the rise time of pulses was observed. Pulses become slower at higher temperatures. This is the result of a decreasing effective mobility of the charge carriers at higher temperatures. The temperature dependence of the rise time is well described by a Boltzmann-like *ansatz* $p_0 + p_1 \exp(-p_2/T)$. This is in contradiction to the model expectation of a $T^{-3/2}$ behavior.

Earlier experimental results [76, 77] indicate a $T^{-1.6}$ and $T^{-1.66}$ behavior, respectively. However, such an exponent does not provide an adequate description of the data. The measured deviation from the expected $T^{-3/2}$ is significant. Therefore, some additional detector-specific effects are suspected to result in the observed Boltzmann-like behavior. An effective temperature dependence of the charge carrier density was introduced and together with a first order polynomial in T for the mobility, the data could be fitted reasonably. However, the precision of the current data, especially due to the uncertainties in the monitoring of the absolute temperature, does not allow for a final conclusion.

An important observation is that the pulse amplitudes are constant for the T range 95–130 K to better than 0.5 % accuracy. This means that the detector can be operated stably at temperatures up to 130 K.

Chapter 7

Determination of the crystal axes in segmented detectors

The orientation of the crystallographic axes of a detector is important when dealing with pulse shapes, e.g. for pulse shape analyses or pulse shape simulations. As was discussed in Section 3.4, the mobility of charge carriers determines the drift velocity in a given electric field. Being a tensor, the mobility causes transverse anisotropy in a germanium crystal and leads to charge carrier trajectories not being aligned with the electric field. Thus, the axes orientations not only influences the velocity but also the trajectories of the charge carriers. While the $\langle 001 \rangle$ axis is usually aligned to the geometric Z axis a coaxial detector, the orientation of the other two, $\phi_{\langle 100 \rangle}$ and $\phi_{\langle 110 \rangle}$, are usually unknown upon delivery. Their orientation has to be obtained experimentally.

Two methods to determine the axes orientation of high purity germanium detectors were investigated. The first method uses the pulse lengths directly. The pulse lengths depend on the length of the trajectories and the velocity of the charge carriers. The form of a trajectory depends on the distance of the initial energy deposit to the crystallographic axes [71]. The trajectories are straight only along the axes. Elsewhere, they are curved. The shortest pulses occur along the $\langle 100 \rangle$ axis, the longest along the $\langle 110 \rangle$. Thus a periodic ϕ dependence of pulse lengths is expected. To extract the axes orientation, a ϕ scan is performed and the resulting data are fit with a sine function. This method will be denoted as "Scan method".

The second method uses Monte Carlo simulations and can only be applied to segmented detectors. The curved trajectories lead to changes in ϕ of up to 10 degrees between start and end point [71]. This influences the occupancies [1] of the individual segments significantly when a detector is irradiated with a penetrating γ-source. Taking into account axes effects in the simulation, the axes orientation can be determined by varying the axes orientation in the simulation and comparing simulated and measured occupancies. This method will be denoted as "Occupancy method".

[1] Occupancy is defined as the number of counts in a given segment under the selected energy peak per measurement.

7.1 Experimental setup

The measurements were taken using the Siegfried II detector installed inside the vacuum cryostat, K1, see Section 3.5. The operational voltage of the detector was 2000 V. The DAQ as described in Section 3.5 was used to record pulses and reconstruct energy.

A cylindrical coordinate system was chosen with the origin, $z = 0$, at the geometrical center of the detector and $\phi = 0$ on the 15–4 segment boundary. A schematic view of the segmentation scheme is depicted in Fig. 7.1.

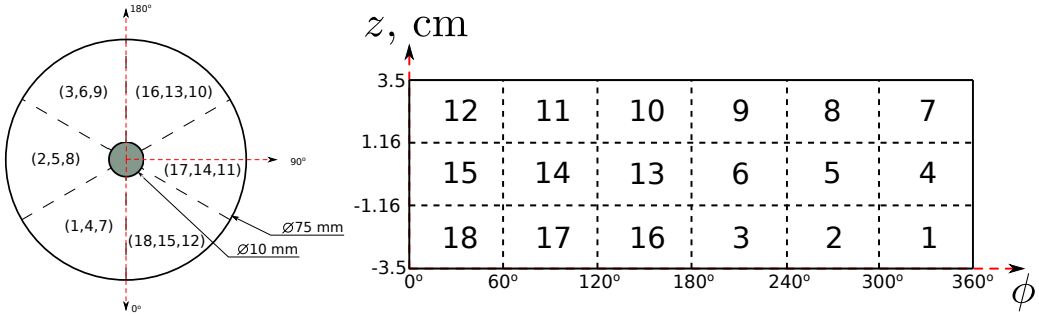

Figure 7.1: Coordinate system and segmentation scheme of Siegfried-II. Numbers in parentheses show the segment numbers for the three layers: (bottom, middle, top).

The different source configurations used for the different methods are summarized in Table 7.1. The height, $h = z - 8.5\,\text{mm}$, of the source relative to the top of the vacuum can is also specified. The ^{152}Eu source was collimated with a $1\,\sigma$ diameter of the beamspot on the outer mantle of the detector of about 5 mm. The ^{60}Co and the ^{228}Th sources were not collimated.

Method	Source	Source positions:			
		r [cm]	z [cm]	h [cm]	ϕ [°]
Scan	75 kBq ^{152}Eu	9.6 ± 0.5	0	-8.5 ± 0.2	0 – 360
Occupancy "on top"	40 kBq ^{60}Co	0	18.5 ± 0.2	10 ± 0.2	-
	28 kBq ^{228}Th	0	18.5 ± 0.2	10 ± 0.2	-
Occupancy "from side"	23 kBq ^{228}Th	17.6 ± 0.2	-2.3 ± 0.2	-10.8 ± 0.2	155 ± 5

Table 7.1: Source configurations used for both methods. The coordinates are explained in the text.

The experimental setups for the occupancy method as implemented in the simulation package, MAGE , are shown in Fig. 7.2.

Details of the experimental setups specific to each method will be described in the corresponding chapters.

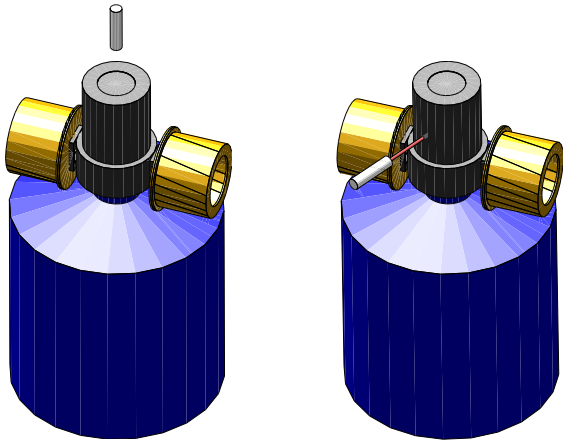

(a) *Top* case (b) *Side* case

Figure 7.2: Schematic views of the experimental setups for the "Occupancy" method as implemented in MaGe .

7.2 Azimuth angle scan

7.2.1 Method description

Measurements were taken with a collimated ^{152}Eu source, varying its ϕ position in ten degree steps between 0° and 350°. The 122 keV line was used as photons of such energy are absorbed within a depth of 0.5 cm and thus induce mostly events at the surface. Each measurement lasted for ≈30 minutes, yielding about 800 events in the 122 keV spectral peak. A second dataset with $-10° \leq \phi \leq 160°$ was taken to study systematic uncertainties.

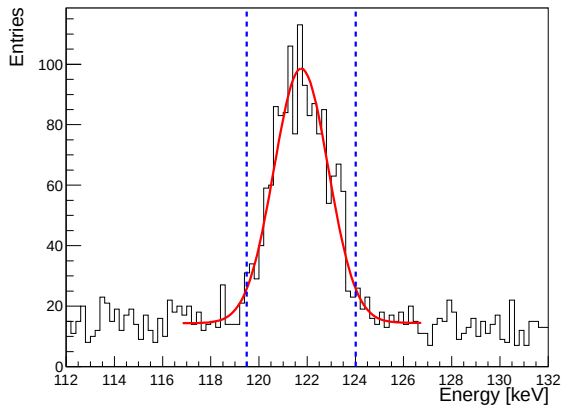

Figure 7.3: Energy spectrum as seen in the irradiated segment 4. Also shown is a fit with a Gauss function plus a first-order polynomial. The 2σ limits are shown as dashed lines.

Pulses were selected using the energies measured in the individual segments. Single segment events were selected by requiring energy deposits of less than 20 keV in all other

segments. Figure 7.3 shows the single segment spectrum around 122 keV observed in the irradiated segment 4 at $\phi = 330°$. The width of the peak was determined by a fit with a Gauss function, and events within $\pm 2\sigma$ were selected. Only events were considered where the segment energy, E_s, was compatible with the core energy, E_c, with $|E_c - E_s| < 10\,\text{keV}$.

7.2.2 Extraction of the axes orientation

The procedure to determine the rise time of a measured segment pulse was discussed in Section 6.5. Baseline and noise were determined using the first 400 ns of a pulse. The level of the noise was typically about 3 % of the pulse amplitude at 122 keV. Typical signal to background ratios were 0.5 to 1.5.

Only good fits were considered. A fit was qualified as good, if $\chi^2/\text{ndf} \leq 1.5$. The value of 1.5 was chosen to keep 68% of the pulses, see Fig. 7.4.

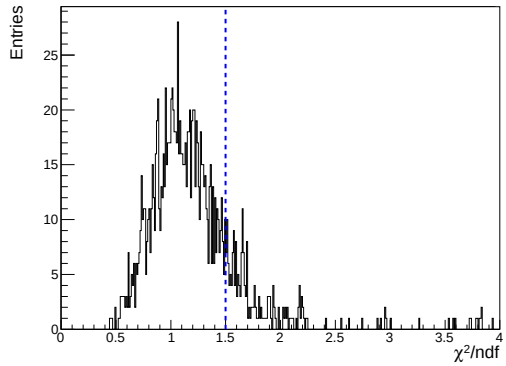

Figure 7.4: An example of the χ^2 distribution for the pulse fits. Also shown is the 68% limit, taken as the cut.

Figure 7.5 shows examples of two events with good and bad fits.

The distribution of the fit parameter t^c_{scale} for all good fits was fitted with a Gauss function, and the resulting mean, $t^c_{\text{scale-mean}}$, was used to calculate t_{r}^{10-90} for the core at a given position. An example of the fit is shown in Fig. 7.6.

The dependence of t_r^{10-90} on the azimuth angle was fitted with the function

$$t_{\text{r}}(\phi) = A + B \cdot \sin\left(\frac{2\pi}{90}\left(\phi + \phi_{\langle 110\rangle}\right)\right), \tag{7.1}$$

where $\phi_{\langle 110\rangle}$ is a free parameter. Figure 7.7 shows the data together with the fit according to Eq. 7.1.

7.2.3 Systematic uncertainties

The following sources of systematic uncertainty of this analysis method were investigated:

- the cut on the difference of the core and segment energies, $|E_c - E_s|$, was varied to 5 keV and 20 keV;

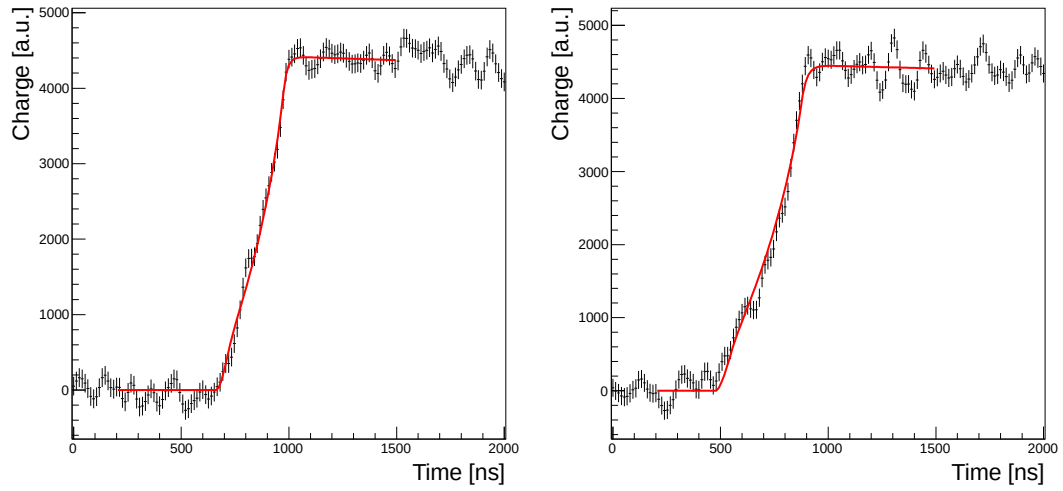

(a) (b)

Figure 7.5: Measured pulses fitted with the simulated pulse: (a) "good" fit with $\chi^2/\text{ndf} = 0.91$, (b) "bad" fit with $\chi^2/\text{ndf} = 2.23$.

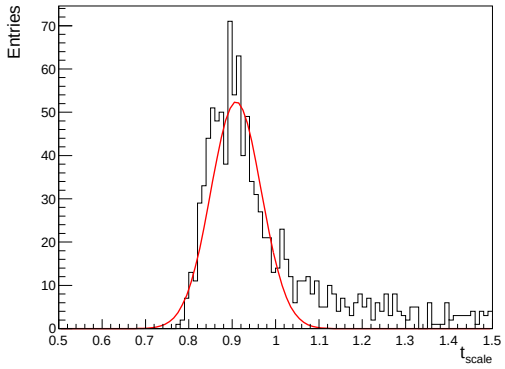

Figure 7.6: An example of the t^c_{scale} distribution. Also shown is a Gauss fit.

- the cut on χ^2 was varied by $\pm 20\%$;
- the second dataset was used. The quality of the vacuum and the temperature were different than for the reference measurements. This resulted in a systematic shift of the rise time to higher values. The fit is shown in Fig. 7.8. The temperature changes during the data taking was significantly larger than for the reference measurements. It resulted in a stretching of the pulses over time, which is represented by the sizeable linear term in the fit.

Table 7.2 shows the obtained values of the systematic uncertainties. In addition, the dominating systematic uncertainty is connected to the placement of the detector within the cryostat. This could only be controlled to 3°. The uncertainties were added in quadrature to give separately positive and negative total uncertainties.

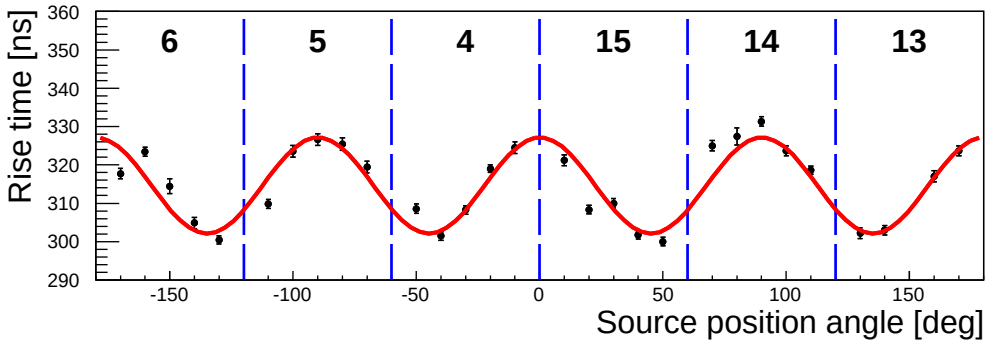

Figure 7.7: Extracted dependence of t_r^{10-90} on ϕ, fitted with the function from Eq. 7.1. Segment boundaries are shown as dashed lines. If the uncertainties are not seen, they are smaller than the markers.

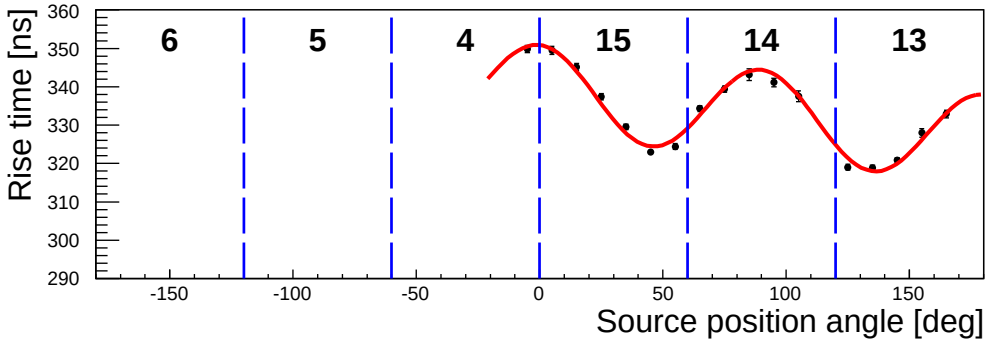

Figure 7.8: Same as Fig. 7.7 for the dataset taken under different conditions. A linear term represents the zero-order approximation of the effect of rising temperature during the data taking. Please refer to the text for the explanation.

Varied quantity	Deviation [°]
$\lvert E_c - E_s \rvert = 10\,\text{keV} \rightarrow 5\,\text{keV}$	-0.50
$\lvert E_c - E_s \rvert = 10\,\text{keV} \rightarrow 20\,\text{keV}$	-0.16
$\chi^2/\text{ndf} = 1.5 \rightarrow 1.2$	0.44
$\chi^2/\text{ndf} = 1.5 \rightarrow 1.8$	0.22
Second dataset used	± 0.08

Table 7.2: Systematic uncertainties for the "Scan" method

7.2.4 Results

The orientation of the $\langle 110 \rangle$ axis was measured using the azimuth scan method for events induced by 122 keV gammas from the ^{152}Eu radioactive source. The orientation of the $\langle 110 \rangle$ axis was calculated to be $\phi_{\langle 110 \rangle} = -0.2° \pm 0.4°(\text{stat.}) \pm 3.1°(\text{syst.})$, where the statistical uncertainty was taken from the fit, and the systematic uncertainty was calculated

as explained in Section 7.2.3.

7.3 Occupancy analysis

7.3.1 Method description

The occupancies of the individual segments were measured with γ-sources that emit photons with high enough energies to interact throughout the detector. The method is based on comparing measured to simulated occupancies; there is no analytic formula to calculate the occupancy as a function of axes orientation. The experimental technique presented here for a segmented detector extracts the $\langle 110 \rangle$ orientation using the six segments of any horizontal layer. The occupancies are simulated for each possible axes orientation and a test statistic is used to find the orientation for which the simulation fits best.

The experimental setup and the source configuration were discussed in Section 7.1. For the *side* case the non-collimated ^{228}Th source was positioned on a 10.3 cm long source holder made of polyvinyl chloride (PVC).

7.3.2 Simulation

The simulation of the experimental setup was done within the MaGe framework [86], based on Geant4 [87].

The "DarkMatter realm" settings for electromagnetic processes within MaGe were used with a trace length for gammas (e^+, e^-) in germanium of 5 (0.5) μm, corresponding to a hit energy threshold of $\approx$1 keV. These settings resulted in $O(70)$ hits for events with a 2.6 MeV photon fully absorbed.

For the analysis presented here, gammas of selected lines fully absorbed in the detector are of interest. Therefore, only the gammas from these lines were simulated. For each sample from Table 7.1, $O(5 \cdot 10^6)$ events with any energy deposit in the detector were simulated. The number of fully absorbed events seen in the segment spectra, depending on the energy, was $\approx 8 \cdot 10^5$ in the core, corresponding to $\approx 4 \cdot 10^4$ per segment.

Hits from the event simulation were combined whenever their distance was less than 1 mm. The electron and hole drift trajectories of each combined hit were simulated using the pulse shape simulation package [71] according to the pre-tabulated electric field using the 4th order Runge-Kutta method. The time step for the drift was 1 ns [2]. The velocities of the charge carriers were assumed to be constant during this period. The drift simulation was performed with the location of the axis angle, $\phi^{sim}_{\langle 110 \rangle}$, as an input parameter which was varied. The final positions, ϕ_{EP} and z_{EP}, of the holes after the drift to the outer surface of the detector were recorded.

As was expected from the crystal anisotropy caused by the tensor nature of the mobility, final positions of the holes after the drift significantly differed from the initial positions of energy deposits. A demonstration of this effect is shown in Fig. 7.9. It shows the comparison between the initial ϕ position, ϕ_{hit}, and ϕ_{EP} of the hole trajectories for the

[2] Larger steps, e.g. 10 ns, result in significant differences in charge carrier trajectories compared to the more accurate simulations. Smaller steps do not change the trajectories significantly.

middle layer of the detector for the two source positions described in Section 7.1. For the *top* case, the minima are aligned with the ⟨110⟩ axes.

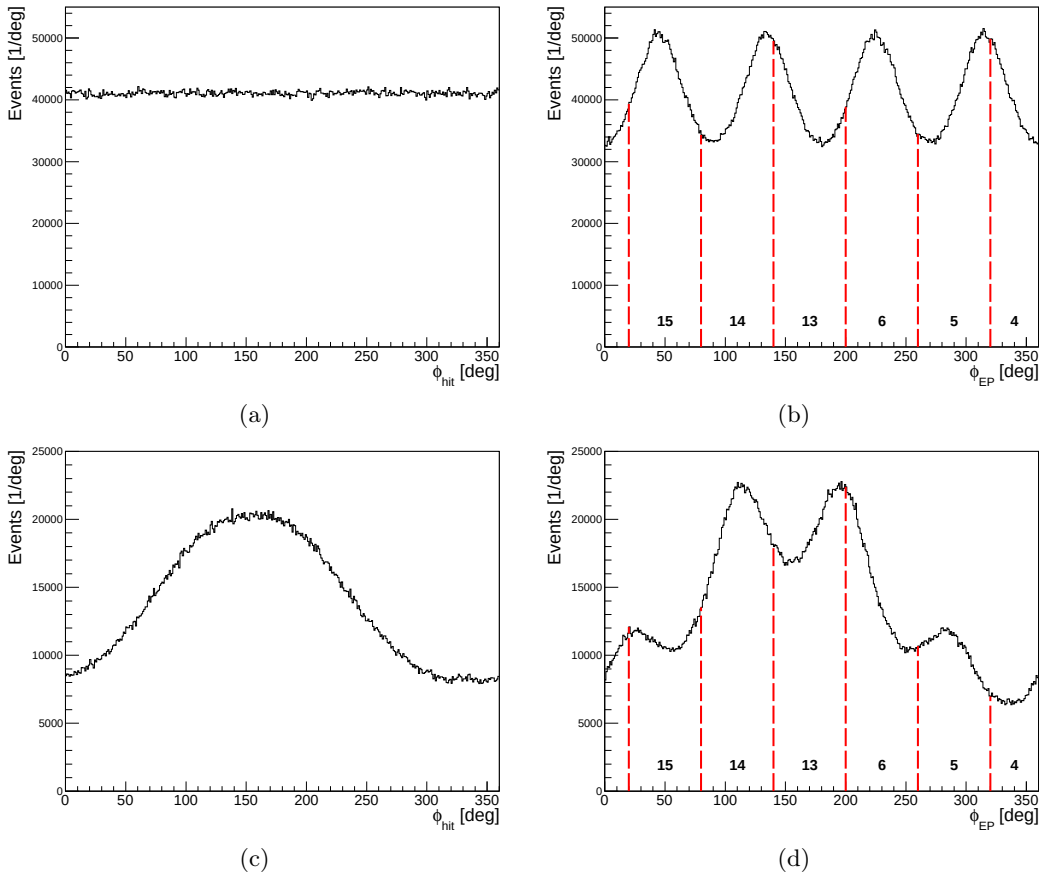

Figure 7.9: Distributions of the azimuth angle of (a)/(c) energy deposits inside the detector and (b)/(d) ϕ_{EP} for the *top*/*side* cases. Also shown is a possible detector segmentation. In (c) and (d) the source is at $\phi = 155°$.

7.3.3 Crosstalk and event selection

The measured occupancies can be influenced by crosstalk. This effect thus has to be accounted for. A detailed discussion of crosstalk can be found in Appendix A. The present analysis does not require a perfect energy resolution, and it is performed for high-energy, i.e. $\gtrsim 500\,\mathrm{keV}$, single-segment events, for which the influence of crosstalk can be avoided. To do so, the cuts to select single segment events were adjusted. The event selection was as follows:

- The energy deposit in the segment, E_s, is close to the core energy, $|E_c - E_s| < 50\,\mathrm{keV}$;
- All other segments have $E_s < 150\,\mathrm{keV}$ ($200\,\mathrm{keV}$ for 2.61 MeV gamma line). Note: the

energy in segment 9 was not taken into account for this selection.

The same selection was used for simulation and data.

7.3.4 Extraction of occupancies

The following full absorption peaks with energies E_γ were used to calculate the occupancies:

1. *Top case.* 0.58 MeV and 2.61 MeV from ^{208}Tl from the ^{228}Th decay chain; 1.17 MeV and 1.33 MeV from ^{60}Co.
2. *Side case.* 0.58 MeV and 2.61 MeV from ^{208}Tl from the ^{228}Th decay chain. Note: the occupancy in segment 9 was not used due to very poor energy resolution (see Section 3.5).

The segment occupancies were extracted from the energy spectra. As the separately measured background spectra did not show lines associated to ^{60}Co, the background was not subtracted for the analysis of these lines. The background did contain the lines of ^{208}Tl. The background spectra collected in a dedicated measurement were normalized according to the measurement time and subtracted from the corresponding spectra collected with the source.

The influence of the background is maximal for the segments that are most distant from the source, where the occupancy is smaller than in the other segments. For the *top* case, it especially affects lower-energy lines at the bottom layer of the detector. Figure 7.10(a) shows a spectrum measured in segment 3 at the bottom layer for the irradiation from the top and the corresponding normalized background spectrum. For the *side* case, the background influences predominantly the segments on the opposite side of the detector relative to the source position. In both cases, the background was not homogeneous and distorted the occupancies.

The resulting segment-spectra were fitted using the binned Log-likelihood method with the function $f(E_s)$ composed of a Gauss function to represent the peak and a sigmoid:

$$f(E_s) = \frac{A}{\sqrt{2\pi}\sigma} e^{-\frac{(E_s-E_\gamma)^2}{2\sigma^2}} + B + \frac{C}{e^{2\frac{E_s-E_\gamma}{\sigma}}+1}, \tag{7.2}$$

where the free parameters for each segment, i, are A_i, B_i, C_i. The sigmoid part represents the background shape that drops for energies above E_γ. Fig. 7.10(b) shows the result of the fit to the background-subtracted spectrum around 0.58 MeV for the irradiation with ^{208}Tl from the top. The contributions from the terms A, B and C are indicated. The occupancy, $\mathcal{O}_i^{E_\gamma}$, for segment i at E_γ was taken from the fit, normalizing A_i by the bin widths of the corresponding histogram, $\mathcal{O}_i^{E_\gamma} = \frac{A_i}{\text{bin width}}$.

Figure 7.11 shows an example of the fitted spectra for all segments at $E_\gamma = 1.33$ MeV for the *top* case.

Each layer of the detector containing six segments was analyzed independently. The measured occupancy distributions for the middle layer are presented in Figs. 7.12 and 7.13 for the *top* case and the *side* case, respectively.

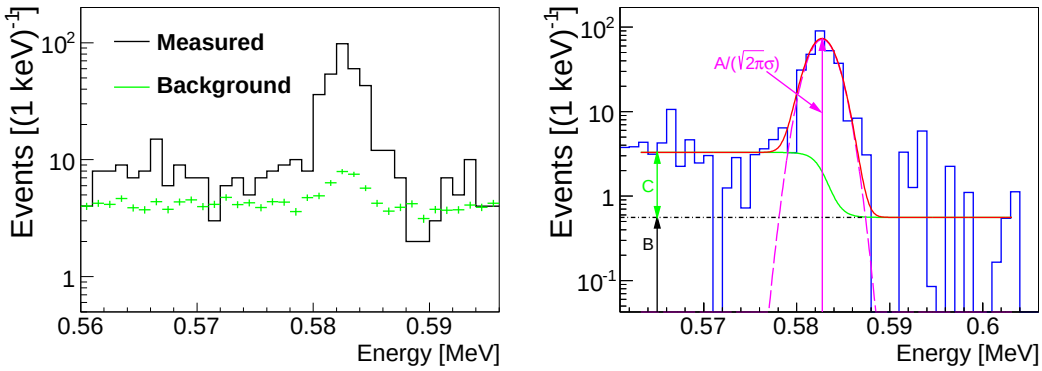

(a) (b)

Figure 7.10: (a) Measured signal and background spectrum in segment 3 around 0.58 MeV and (b) the corresponding fit to the background-subtracted measured spectrum with the function given in Eq. 7.2.

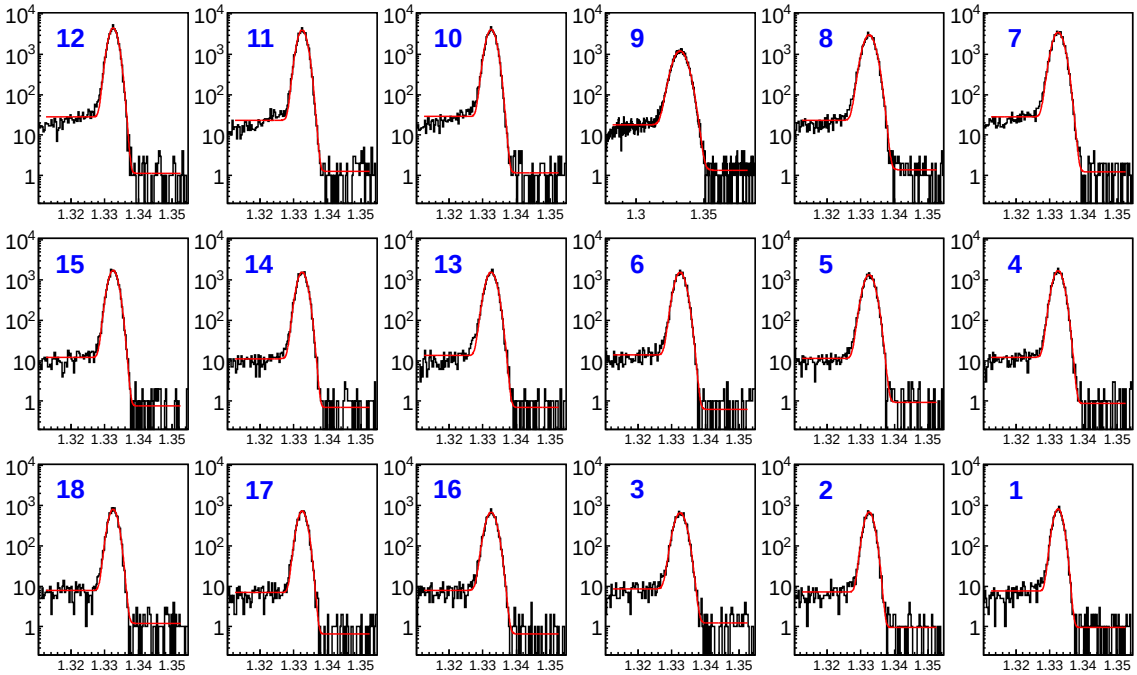

Figure 7.11: Energy spectra measured in the segments at $E_\gamma = 1.33\,\text{MeV}$, fitted with $f(E)$ from Eq. 7.2. The scale of the energy axis for segment 9 is different.

For the simulation, the occupancies were calculated as follows. After the drift, a hit was assigned to the segments according to ϕ_{EP} and z_{EP}. Segment energies were calculated as the sum of the energies of the corresponding hits. The energy resolution was not simulated, resulting in sharp energy peaks in the spectra with almost zero width. A

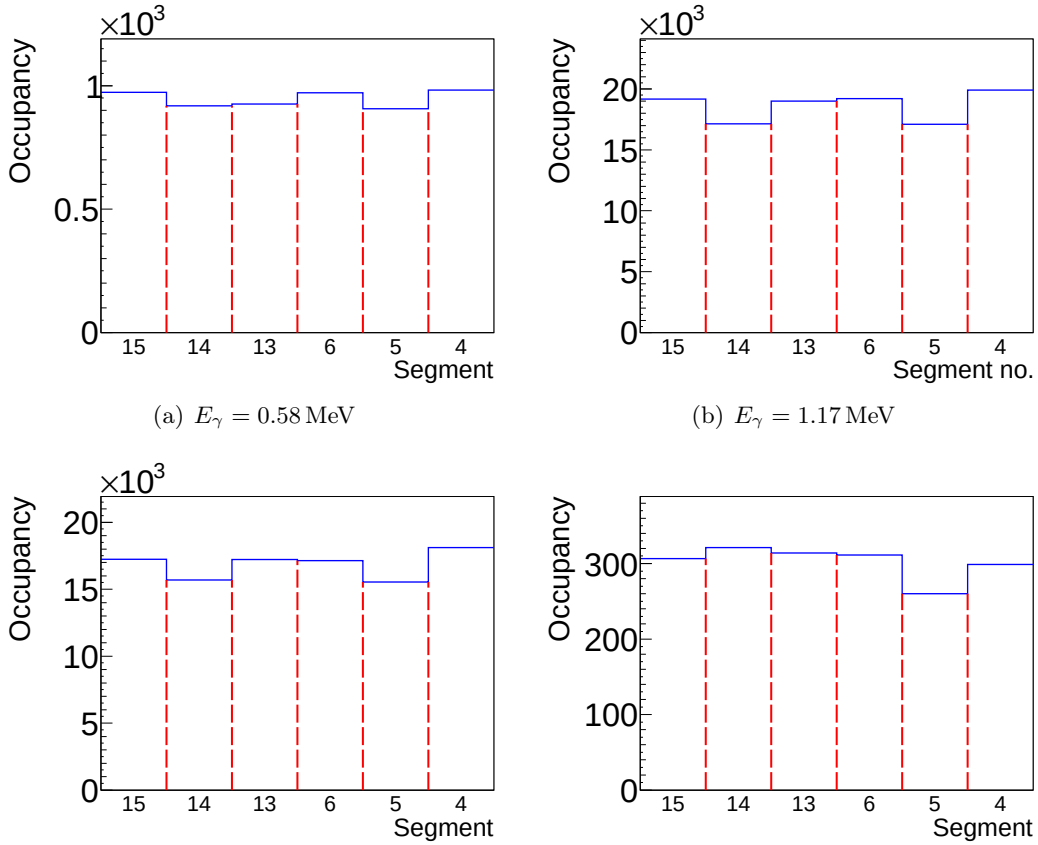

(a) $E_\gamma = 0.58\,\mathrm{MeV}$ (b) $E_\gamma = 1.17\,\mathrm{MeV}$

(c) $E_\gamma = 1.33\,\mathrm{MeV}$ (d) $E_\gamma = 2.61\,\mathrm{MeV}$

Figure 7.12: Measured segment occupancies of the middle layer for the *top* case.

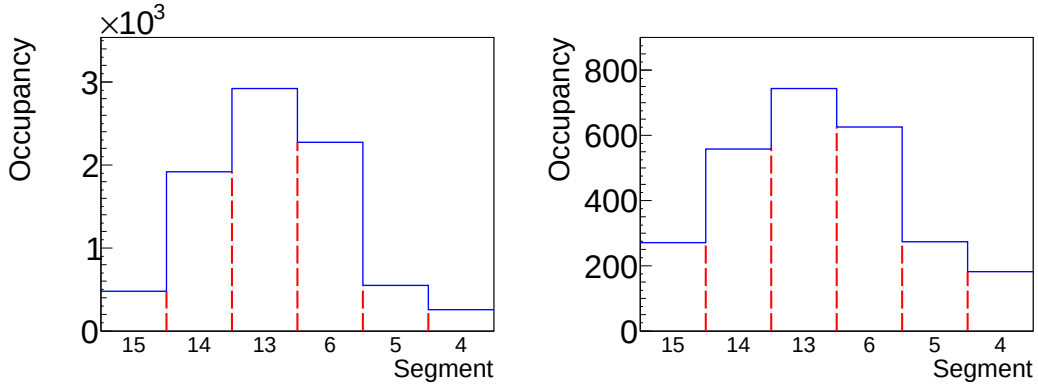

(a) $E_\gamma = 0.58\,\mathrm{MeV}$ (b) $E_\gamma = 2.61\,\mathrm{MeV}$

Figure 7.13: Measured segment occupancies of the middle layer for the *side* case.

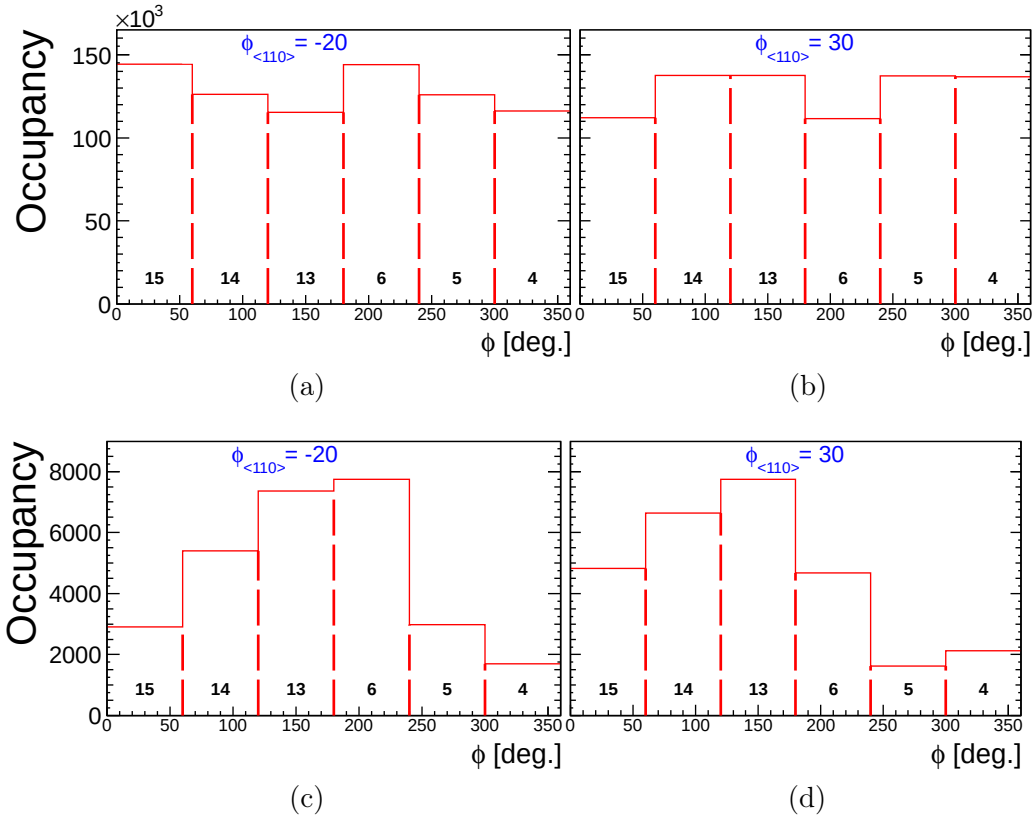

Figure 7.14: Simulated occupancies for (a),(b) *top* case and (c),(d) *side* case for $\phi^{sim}_{\langle 110\rangle} = -20°$ and $\phi^{sim}_{\langle 110\rangle} = 30°$.

possible background spectrum was not simulated. The occupancy of each segment was defined as the number of counts in the energy spectrum in the range $E_\gamma \pm 2\,\mathrm{keV}$ for each peak. Occupancies were calculated for varying $\phi^{sim}_{\langle 110\rangle}$.

The extraction of the occupancies is the most time consuming part of the analysis which was optimized to run in parallel using the power of modern CPUs. More details on the procedure can be found in Appendix B.

For the *top* case, in which the experimental setup was symmetrical, the axis angle variation could be logically replaced by changing the segmentation angle, i.e. instead of simulating different axis orientation, the segmentation scheme was varied. Only one set of Monte Carlo sample was required.

For the *side* case, the detector segmentation angle has to be kept because it has to correspond to the source position. Therefore, this method required drift simulations for each axis angle orientation which was technically more time consuming.

An illustration of the way occupancies change with $\phi^{sim}_{\langle 110\rangle}$ is given in Fig. 7.14 for the middle layer.

7.3.5 Extraction of the axis orientation

The axes orientation was determined by comparing the occupancies measured to the occupancies simulated for varying $\phi^{sim}_{\langle 110\rangle}$. The value of $\phi^{sim}_{\langle 110\rangle}$ was changed in 1° steps within [-45°, 45°] for the *top* case and [110°, 200°] for the *side* case. A test statistic, ϵ, was used to evaluate the agreement between data and simulation:

$$\epsilon = \sum_{i=1}^{6} \frac{(D_i - MC_i)^2}{D_i^2}, \tag{7.3}$$

where D_i and MC_i denote the measured and simulated occupancies in segment i of a given layer, respectively, and the sum over i is taken for the six segments of each layer. For the *side* case, the sum for the top layer excludes Segment 9. The dependence of ϵ on $\phi^{sim}_{\langle 110\rangle}$ is a smooth function with a minimum, $\Phi_{\min\epsilon}$, which is expected to occur at the real orientation of the $\langle 110\rangle$ axis. The value of $\Phi_{\min\epsilon}$ was determined by a second order polynomial fit with a fit window of 20°. The dependencies of ϵ on $\phi^{sim}_{\langle 110\rangle}$ and the corresponding fits are shown in Figs. 7.15 for the *top* case and 7.16 for the *side* case.

The minimum values, $\epsilon_{\min}$, from the fits were used to calculate weights, $w = \epsilon^{-1}_{\min}$. Such a weight for the chosen test statistic provides a possibility to combine results obtained for different layers and energies. The values of $\Phi_{\min\epsilon}$ and w are listed in Table 7.3.

Case	Energy	Top layer		Middle layer		Bottom layer	
	[MeV]	$\Phi_{\min\epsilon}$ [°]	w	$\Phi_{\min\epsilon}$ [°]	w	$\Phi_{\min\epsilon}$ [°]	w
Top	0.58	**-11.1 ± 0.1**	79	**-8.6 ± 0.1**	52	**13.1 ± 0.1**	52
Top	1.17	**-7.7 ± 0.1**	100	**1.4 ± 0.1**	115	**-3.7 ± 0.1**	167
Top	1.33	**-7.1 ± 0.1**	88	**4.2 ± 0.1**	99	**1.1 ± 0.1**	117
Top	2.61	**0.3 ± 0.2**	38	**-6.2 ± 0.2**	23	**-6.3 ± 0.2**	44
Side	0.58	**-21.9 ± 0.1**	33.5	**-14.2 ± 0.1**	52	**-23.4 ± 0.2**	63
Side	2.61	**-18.6 ± 0.1**	18.5	**-15.6 ± 0.1**	43	**-15.9 ± 0.2**	24

Table 7.3: Values of the extracted axis orientations and weights of the fits for different energy peaks and layers. The results for the *side* case were rotated by 180° to be directly comparable.

7.3.6 Systematic uncertainties

The spread of results obtained with different layers and different energy lines was investigated. The sources of systematic uncertainty fall into two categories:

- parameters used in the treatment of the data, i.e. choices for the analysis;
- imperfections of the simulation.

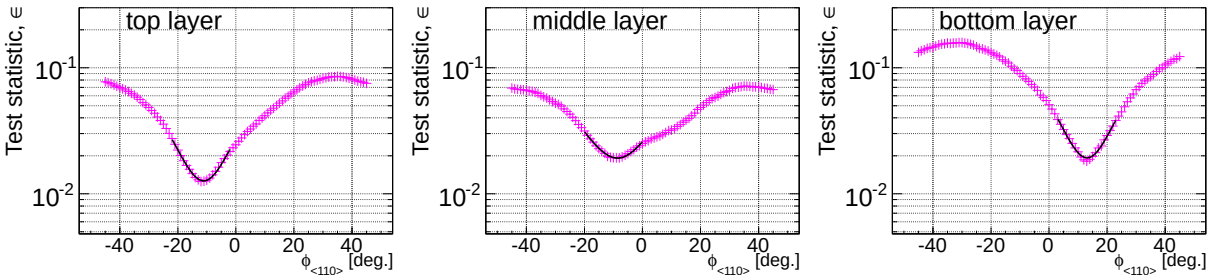

(a) *Top* case, 0.58 MeV

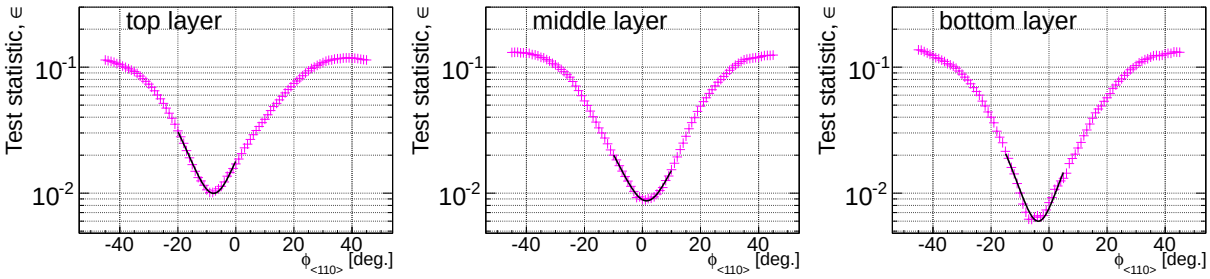

(b) *Top* case, 1.17 MeV

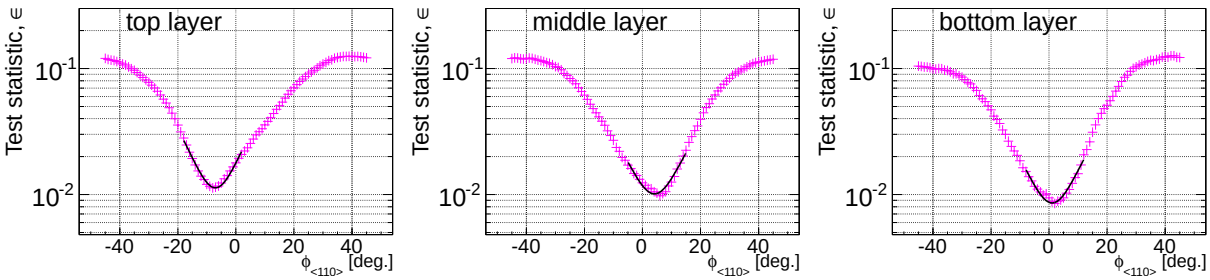

(c) *Top* case, 1.33 MeV

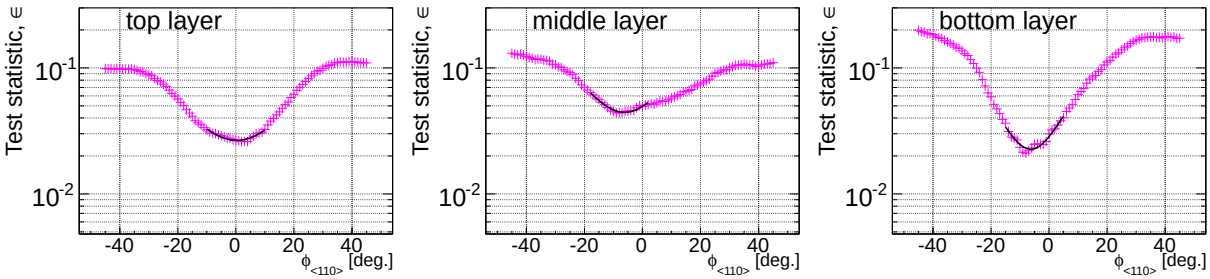

(d) *Top* case, 2.61 MeV

Figure 7.15: Dependence of ϵ on $\phi^{sim}_{\langle 110\rangle}$. Also shown are the second order polynomial fits.

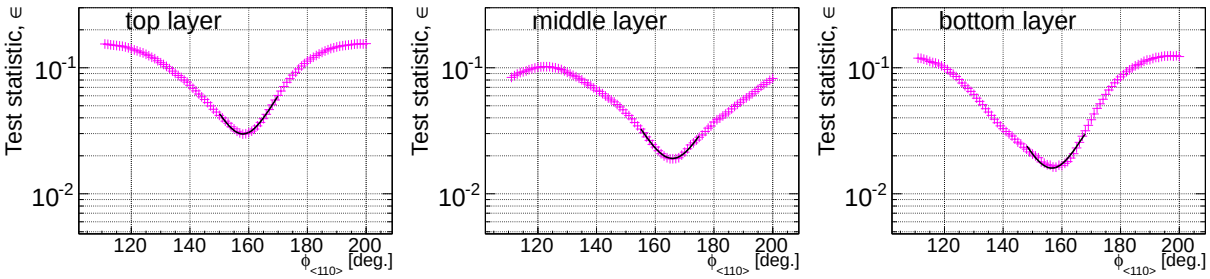

(a) *Side* case, 0.58 MeV

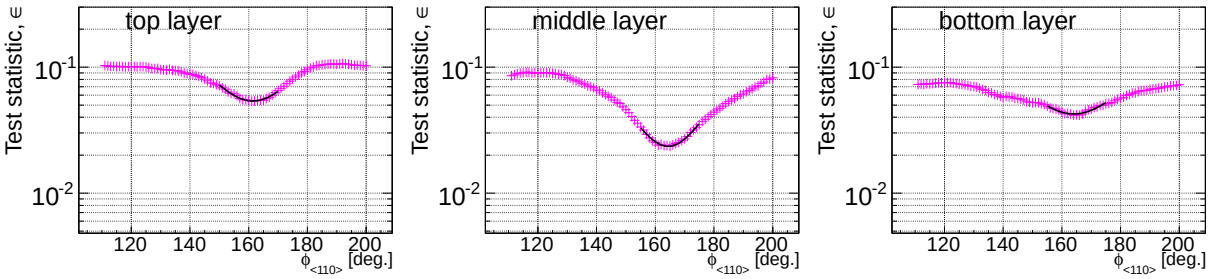

(b) *Side* case, 2.61 MeV

Figure 7.16: Dependence of ϵ on $\phi^{sim}_{\langle 110\rangle}$. Also shown are the second order polynomial fits.

The uncertainties in the treatment of the data are connected with the definition of the ϵ test statistic. It is different from a classical Neyman χ^2 test statistic,

$$\chi^2 = \sum_{i=1}^{6} \frac{(D_i - MC_i)^2}{D_i}, \tag{7.4}$$

and puts more emphasis on bins with low content. The minimum values of $\Phi_{\min}$ using χ^2, $\Phi_{\min\,\chi^2}$, and their weights are listed in Table 7.4.

The difference of the results obtained with different test statistic is not large for the *top* case, resulting in a systematic uncertainty of 1°. For the *side* case, in which the difference in occupancies of individual segments are significant, the uncertainty was estimated to be 3°.

Various possible impacts on the parameters of the ϵ-distribution fit were also studied. The fit window was changed to 10° and 30°. The resulting uncertainty was 1°. The fit result also depends on the center of the fitting ranges, which was chosen by eye. Variation of the initial choice yielded an uncertainty of 2°. The total uncertainty connected to ϵ was estimated as the quadratic sum of the individual uncertainties. It was 2.4°(3.7°) for the *top* (*side*) case.

The second category includes the uncertainties of the simulation of the experimental setup. The default clustering size of the hits before the drift was changed from 1 mm to 2 mm. The influence on the results is very small, see Table 7.5(a)-(b).

Case	Energy	Top layer		Middle layer		Bottom layer	
	[MeV]	$\Phi_{\min\chi^2}$ [°]	w	$\Phi_{\min\chi^2}$ [°]	w	$\Phi_{\min\chi^2}$ [°]	w
Top	0.58	**-10.8 ± 0.1**	453	**-8.1 ± 0.1**	311	**13.2 ± 0.1**	326
Top	1.17	**-7.4 ± 0.1**	590	**1.5 ± 0.1**	680	**-3.5 ± 0.2**	963
Top	1.33	**-6.7 ± 0.1**	527	**4.0 ± 0.1**	608	**1.0 ± 0.1**	690
Top	2.61	**0.4 ± 0.2**	227	**-6.5 ± 0.2**	129	**-5.6 ± 0.2**	260
Side	0.58	**-32.0 ± 0.6**	179	**-11.9 ± 0.4**	486	**-20.4 ± 0.1**	593
Side	2.61	**-26.0 ± 0.1**	128	**-17.6 ± 0.2**	262	**-19.4 ± 0.2**	276

Table 7.4: Values of the extracted axis orientation using the χ^2 test statistic from Eq. 7.4, $\Phi_{\min\chi^2}$. Also listed are the weights of the fits, however the results cannot be combined using weights from the χ^2 test statistic. The results for the *side* case were rotated by 180°to be directly comparable.

The influence of the impurity variation in the detector was studied using a simulated lower impurity detector with a ρ_{imp} gradient of $(0.00-0.35) \times 10^{10}/\text{cm}^3$. The average impurity densities for the nominal detector, Siegfried-II, and the lower-impurity detector are (0.38, 0.45, 0.52) and (0.06, 0.18, 0.29) in the units of $10^{10}/\text{cm}^3$, respectively, for the (bottom, middle, top) layers. Figure 7.17(a) and 7.17(b) show the expectations for the occupancy patterns for $\phi^{sim}_{\langle 110\rangle} = 0°$.

The effect of the impurity variation can be quantified using the definition of the **pattern amplitude**, A_{i-j}, as the depth of a first step of the pattern, i.e. the difference between occupancies for the segments i and j located in the same layer. For the middle layer, $A_{15\text{–}14}$ is 0.0326 for the nominal detector and 0.0339 for the lower-impurity one. This is a small change of 0.6 % in a 20 % effect of the occupancy difference with respect to the occupancy of 1/6=0.17 in all segments if there was no anisotropy.

Figures 7.17(a) and 7.17(b) also show the deviations in the patterns, $\Delta_{k\text{–}l}$, for the top and bottom layers from the middle layer, where k and l denote the relevant segment in different layers, but at the same ϕ. The values of $\Delta_{k\text{–}l}$ reach 10 % of the amplitude. The 180° degenerate pattern is broken in the top and bottom layers due to a drift component along z arising from the impurity change in z, which is compensated for the middle layer.

The shape of the pattern, however, does not change significantly due to modified impurities. The resulting absolute values of ϵ will change but the results will not. Thus, the influence of modified impurities levels on the results is again small, see Table 7.5(c).

The most important uncertainty arises from any source misalignment relative to the detector. Figure 7.18 shows the predicted patterns for the 1.33 MeV and 2.66 MeV lines for the *top* case with two shifts by $r = 5\,\text{mm}$, the precision of the source location in the experimental setup, one at $\phi = 45°$ and one at $\phi = 90°$. The misalignment causes distortions of the pattern by 10 % of the amplitude. The occupancy in each bin does not directly depend on the distance between the source and the geometrical center of the considered segment but rather on the solid angle of the segment as seen by the source. For different energy lines, this effect varies as the effective volumes[3] differ and so does the event

[3]volumes at which a photon can be fully contained in a segment.

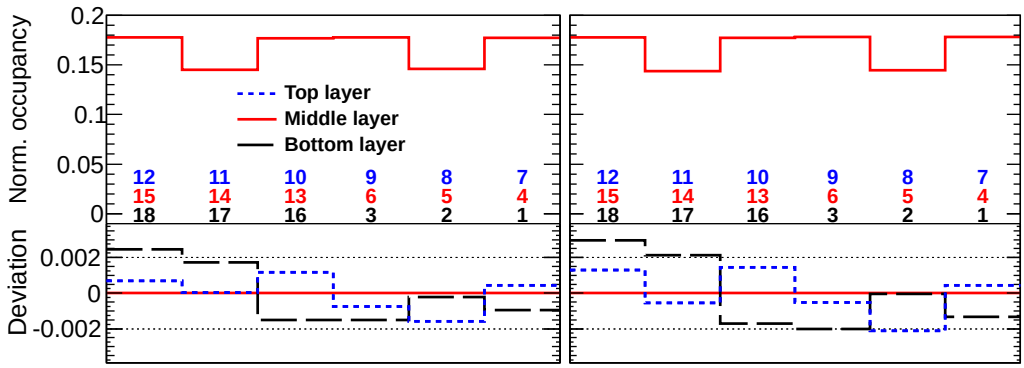

(a) (b)

Figure 7.17: Comparison of the normalized predicted occupancies for the 1.33 MeV line and $\phi^{\text{sim}}_{\langle 110\rangle} = 0°$ for (a) the middle, top and bottom layers of the Siegfried-II-like simulated detector and (b) a crystal with ρ_{imp} changing linearly with z from $0.00 \times 10^{10}/\text{cm}^3$ to $0.35 \times 10^{10}/\text{cm}^3$. The difference between different layers is small, on a percent level. Therefore, the deviations from the middle layer are shown.

topology. This explains why when the 1.33 MeV source was misaligned at 45°, segment 13 "sees" more events than in the nominal position, even though it is more distant from the segment center, see Fig. 7.18 and Fig. 7.1. The corresponding systematic uncertainty for the *top* method is 5°, see Table 7.5(d)-(g).

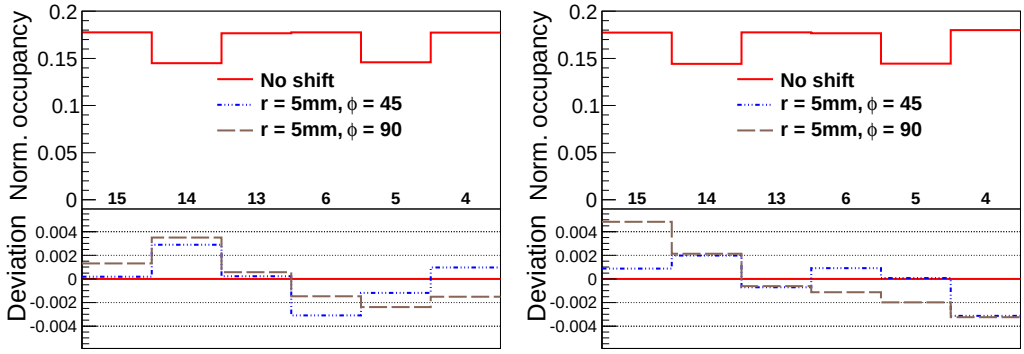

Figure 7.18: Comparison of the normalized predicted occupancies for $\phi^{sim}_{\langle 110\rangle} = 0°$ for the middle layer for (a) the 1.33 MeV line and for (b) the 2.61 MeV line for irradiation from the top. Also shown are the pattern distortions predicted for a 5 mm misalignment of the source along 45° and 90°.

The systematic uncertainty for the *side* case is also dominated by the accuracy of the source position. The detector was remounted for the *side* measurement and its relative rotation could be controlled to about 3°. The source angular position could only be controlled to about 5°. Added in quadrature, it results in a 6° uncertainty.

Case	Energy	Top layer		Middle layer		Bottom layer	
	[MeV]	Var. [°]	w	Var. [°]	w	Var. [°]	w
(a) 2mm hit cluster.	1.17	**-0.04**	107	**0.06**	116	**-0.16**	190
(b) 2mm hit cluster.	1.33	**0.12**	88	**-0.03**	102	**0.30**	114
(c) Imp. variation	1.33	**-0.10**	65	**-0.16**	79	**0.03**	95
(d) Displacement 45°	1.33	**0.27**	95	**-2.2**	110	**-2.4**	77
(e) Displacement 90°	1.33	**0.63**	103	**0.29**	101	**-2.1**	107
(f) Displacement 45°	2.61	**-7.1**	34	**2.3**	25	**3.2**	33
(g) Displacement 90°	2.61	**-8.9**	37	**-4.1**	23	**3.7**	38

Table 7.5: Variation of the extracted axis orientation with respect to the corresponding results listed in Table 7.3 for the *top* case, corresponding to different systematics studies. Also listed are the weights for the extracted values of $\Phi_{\min \epsilon}$.

Background sources have a strong influence on the occupancy patterns, especially if they contain the same lines as used in the analysis. If the background is not stable in time, e.g. is different for measurements and dedicated background data taking, or the equipment in the lab was moved, or the experimental setup was rotated, the spectra may not be properly subtracted and the results will change. It especially affects the irradiation from the side where the segments have significantly different numbers of events. To estimate the uncertainty, the analysis was conducted for the irradiation with ^{208}Tl without the background subtraction. It showed a systematic uncertainty of 1° and 7° for the *top* and *side* cases, respectively.

Any inaccuracy of the description of the experimental setup in the simulation is also reflected in the results. For the *top* case, the amount of material between the source and the detector is minimal. For the *side* case, the source was installed on a 10.3 cm long PVC stick which was positioned directly between the source and segment 16. This material absorbed about 30 % of the gammas in the 2.61 MeV line and affected the gammas with lower energies even more. In addition, the material of the stick is not precisely known and therefore a precise description is not possible. The influence of different materials of the stick and the uncertainty in its length were not studied. However, only the segments directly facing the source were affected.

In total, the systematic uncertainties for the irradiation from the top and the side were evaluated to be 6° and 10°, respectively. They are dominated by the uncertainties on the source positions.

7.3.7 Results

The statistical uncertainties coming from the individual fits as listed in Table 7.3 are always below 0.3° and are negligible compared to the systematic uncertainties. Deviations in the results for the different layers obtained with the 2.6 MeV line for the *top* case cannot be explained by the systematic uncertainties estimated in Section 7.3.6. An ensemble test was performed to estimate the statistical uncertainty connected to fluctuations in

individual bins. The content of each bin, $\mathcal{O}_i^{2.61\,\mathrm{MeV}}$, was randomly modified by adding a value according to a Gauss distribution with $\sigma_i = \sqrt{\mathcal{O}_i^{2.61\,\mathrm{MeV}}}$, i.e. according to its statistical uncertainty. Each time the result of $\Phi_{\min\epsilon}$ using the modified pattern was computed. The fit range for the ϵ dependence was 30°. The distributions of $\Phi_{\min\epsilon}$ for the ensemble test are shown in Fig. 7.19. The ensemble test with 10000 loops yielded statistical uncertainties for the top, middle and bottom layer of 4.2°, 4.1° and 3.6°, respectively.

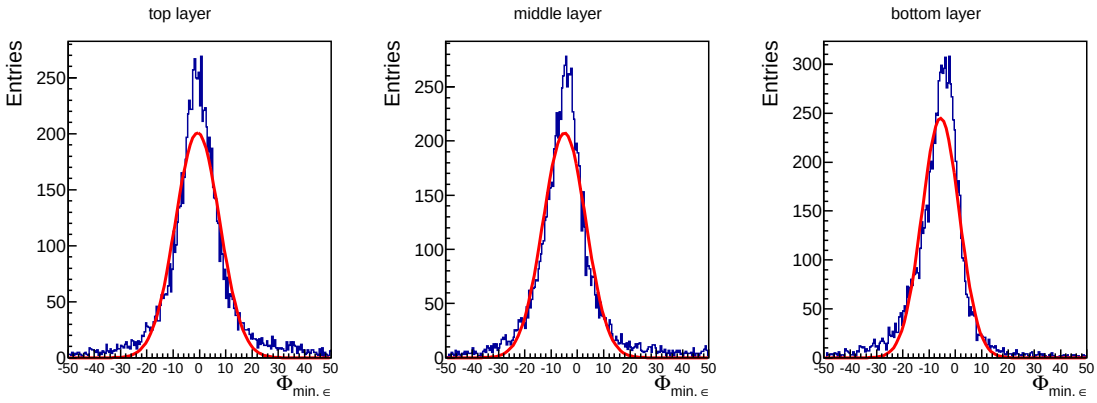

Figure 7.19: $\Phi_{\min\epsilon}$ distributions for the ensemble test described in the text.

The statistical and systematic uncertainties of the results are different for each source position, energy and layer. Therefore, the axis orientation was determined separately for each set as the weighted average:

$$\phi_{\langle 110\rangle}^{sim} = \frac{\sum \Phi_{\min\epsilon} \times w}{\sum w}. \tag{7.5}$$

For the *top* case, the sum runs over all layers and energies of the same source. The results for the Cobalt and Thallium lines are:

$$\phi_{\langle 110\rangle}^{\mathrm{Co,top}} = -1.8° \pm 1°(\mathrm{stat.}) \pm 6°(\mathrm{syst.}) \tag{7.6}$$

$$\phi_{\langle 110\rangle}^{\mathrm{Tl,top}} = -3.6° \pm 4°(\mathrm{stat.}) \pm 6°(\mathrm{syst.}) \tag{7.7}$$

For the *side* case, the individual values of $\Phi_{\min}$ deviate consistently by more than 10° from the expectation. The ensemble test for the 2.6 MeV line, as described previously in this chapter, yielded a statistical uncertainty of 4° and 6° for the middle and bottom layers, respectively. Even though segment 9 was not used in the averaging for the top layer, the results are still consistent with the results for the other layers. The top layer was, however, excluded from averaging. For the *side* case, the result is:

$$\phi_{\langle 110\rangle}^{\mathrm{Tl,side}} = -17.9° \pm 5°(\mathrm{stat.}) \pm 10°(\mathrm{syst.}). \tag{7.8}$$

Examples of occupancy distributions in the middle layer for the closest integer values to $\Phi_{\min\epsilon}$ from Table 7.3 are shown in Figs. 7.20 and 7.21 for the *top* case and the *side* case, respectively.

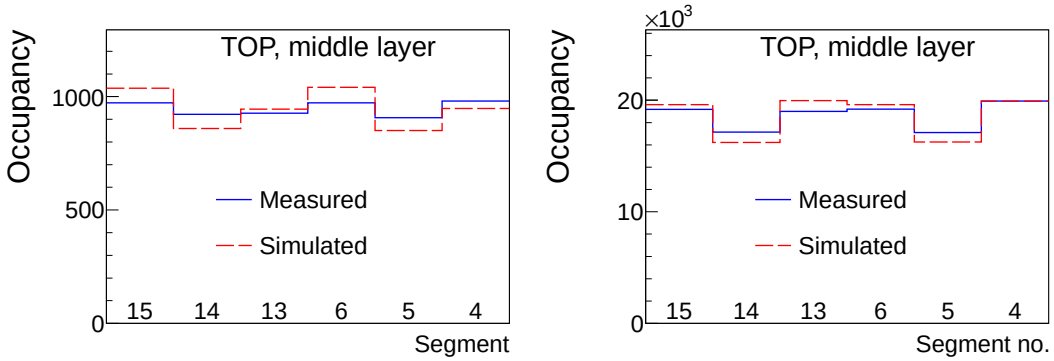

(a) *Top* case, 0.58 MeV, $\phi^{sim}_{\langle 110\rangle} = -9°$

(b) *Top* case, 1.17 MeV, $\phi^{sim}_{\langle 110\rangle} = 1°$

(c) *Top* case, 1.33 MeV, $\phi^{sim}_{\langle 110\rangle} = 4°$

(d) *Top* case, 2.61 MeV, $\phi^{sim}_{\langle 110\rangle} = -6°$

Figure 7.20: Measured and simulated occupancies for the corresponding $\Phi_{\min\epsilon}$ in the middle layer for the *top* case.

The results for the *top* case using the ^{60}Co source show a very good agreement with the azimuth angle method which is considered the most accurate. This is well explained by the high statistics of the collected data and the event topology for the gamma lines used. Photons of energies 1.17 MeV and 1.33 MeV have a higher chance to be contained in a single segment than those of e.g. 2.61 MeV. On the other hand, their penetration depth is much higher than for e.g. 0.58 MeV. For the present analysis and experimental setup, the ^{60}Co source was suited the best.

The result obtained for the *side* case is barely consistent with the one obtained with the scan. However, the simulated occupancy patterns for the best fit shows a good agreement in shape. Most likely, the relative source position was not known as precisely as was hoped. Moreover, the background contribution was not properly controlled. Most of the systematic uncertainties discussed above can be significantly reduced in future analyses.

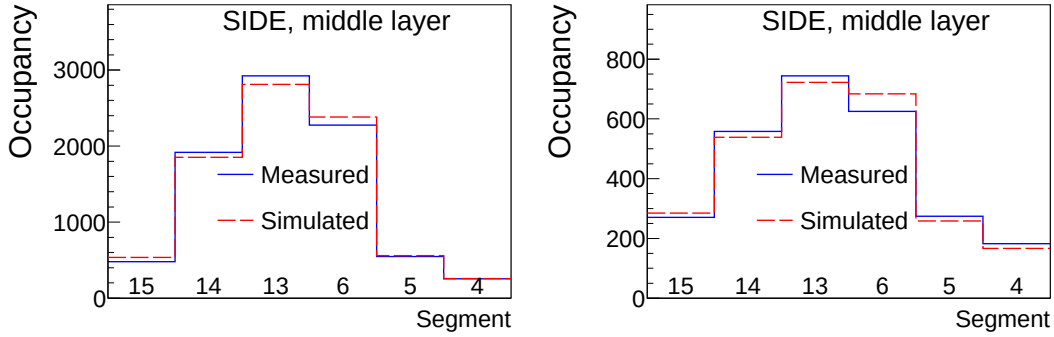

(a) *Side* case, 0.58 MeV, $\phi^{sim}_{\langle 110\rangle} = 166°$ (b) *Side* case, 2.61 MeV, $\phi^{sim}_{\langle 110\rangle} = 164°$

Figure 7.21: Measured and simulated occupancies for the corresponding $\Phi_{\min\epsilon}$ in the middle layer for the *side* case.

7.3.8 Discussion of uncertainties in the mobility

The enhanced patterns indicate that the curvature of the hole trajectories is overestimated in the simulation. The curvature of the drift trajectories of holes can be described in terms of the transverse component of the drift velocity, v_ϕ. Its numerical expression is given by the model reported in Ref. [70] as:

$$v_\phi \propto \Omega(k_0), \tag{7.9}$$

$$\Omega(k_0) = 0.006550\,k_0 - 0.19946\,k_0^2 + 0.09859\,k_0^3 - 0.01559\,k_0^4, \tag{7.10}$$

$$k_0(v_{\text{rel}}) = 9.2652 - 26.3467\,v_{\text{rel}} + 29.6137\,v_{\text{rel}}^2 - 12.3689\,v_{\text{rel}}^3, \tag{7.11}$$

$$v_{\text{rel}} = v_{\langle 111\rangle}/v_{\langle 100\rangle}, \tag{7.12}$$

where $v_{\langle 111\rangle}$ and $v_{\langle 100\rangle}$ are the hole velocities along the corresponding axes that are calculated according to formula 6.4,

$$v(\boldsymbol{x}) = \frac{\mu^0 E(\boldsymbol{x})}{(1 + (\frac{E(\boldsymbol{x})}{E_0})^\beta)^{1/\beta)}},$$

with the fit parameters: E_0, β and the mobility μ^0. The approximation according to Eqs. 7.9–7.12 is highly non-linear and only depends on the relative velocity v_{rel} at a given point but not on the absolute values of $v_{\langle 111\rangle}$ and $v_{\langle 100\rangle}$. The absolute values of the mobilities can only change the drift speed, but not the trajectories.

To accommodate for discrepancies between simulated and measured occupancies, the hole mobility along the $\langle 111\rangle$ axis was changed through the μ^0 parameter according to the values listed in Table 7.6. The effect on the curvature of the hole trajectories is shown in Fig. 7.22. The effect is strong. The maximal angle between the starting point at the inner contact and the final point at the outer contact of the hole trajectories are listed in Table 7.6 for different values of μ_0.

	μ_0, along $\langle 111 \rangle$ [cm^2/Vs]	Max. deviation in ϕ	**Pattern amplitude**
50%	30608	35°	0.092
90%	55094	17°	0.032
Nominal	61215	13°	0.022
110%	67337	9°	0.015

Table 7.6: Effect of changing $v_{111} \propto \mu_0$ on the angular shift of the hole drift and the pattern amplitude.

The patterns for the modified values of $v_{\langle 111 \rangle}$ were simulated in a simplified way. The hole drifts from homogeneously distributed energy deposits of the same energy, see Fig. 7.23(a), were computed. In total 3872 hole drift paths were simulated. The occupancy distributions obtained from the simulation are shown in Fig. 7.23(b). For each value of $v_{\langle 111 \rangle}$, the pattern amplitude $A_{15\text{–}14}$ of the resulting occupancy distribution for the middle layer was calculated. The results are given in Table 7.6.

The shape of the occupancy distributions are quite well described by the simulation. However, the pattern amplitude is overestimated by the simulation by ≈40%. Such a large discrepancy can neither be explained by an incorrectly simulated impurity density in the crystal nor by a small displacement of the source. The mobility parameter μ^0 is not the only parameter that enters the theoretical model. However, even a slight variation of this parameter results in a significant change of the amplitudes of the simulated occupancy distributions. The discrepancy between the predicted and measured amplitudes could be explained by an underestimated value of $v_{\langle 111 \rangle}$ and thus v_{rel} by $\approx 10\,\%$. Dedicated, more detailed studies are required to investigate the influence of the other parameters entering the theoretical model of mobilities. However, the measurement of occupancy patterns might open a path to measure relative mobilities.

7.4 Summary

Two options to determine the orientation of the crystallographic axes in a segmented detector were investigated. The axis orientation can be determined to the best accuracy using an azimuth scan with a low-energy radioactive source such as ^{152}Eu. This method, however, requires a special setup for a detector with the option to move the source around the detector.

The axes can also be located using the occupancy method that is performed using a simulation of the experimental setup including the charge drift in the detector. In this case, any setup can be used and the measurement time can be significantly reduced in comparison to the scan method. The occupancy method works with any source in any setup as long as the setup geometry is sufficiently well simulated and the background, if present, is properly taken into account. The method works best when a gamma line is

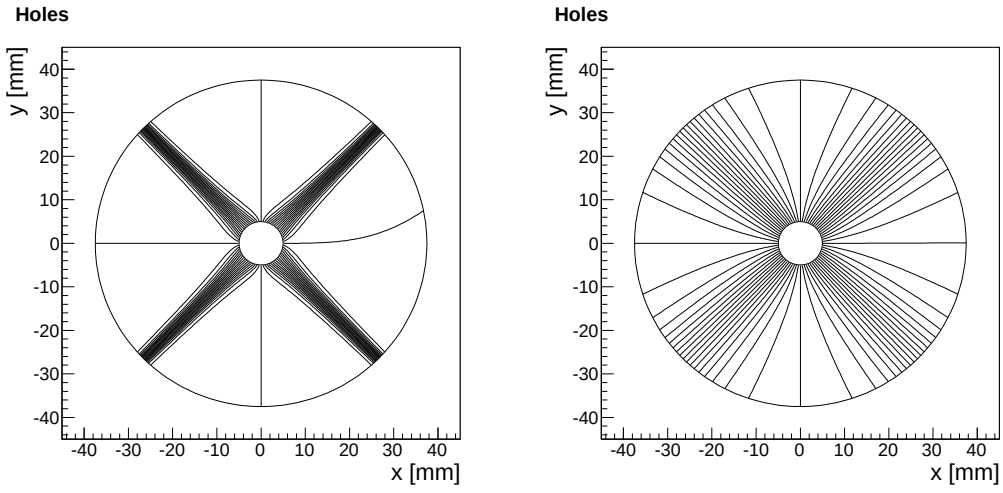

(a) 50%

(b) 90%

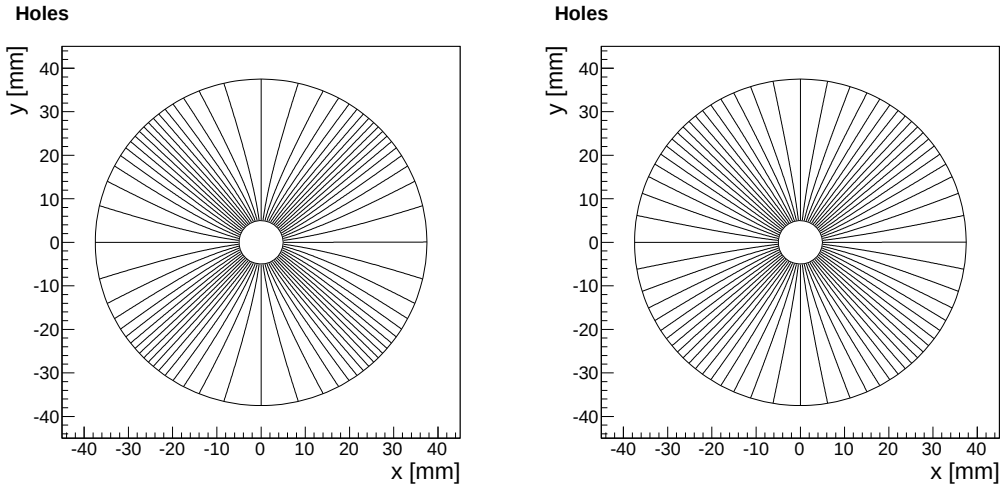

(c) Nominal

(d) 110%

Figure 7.22: Drift trajectories of holes for different modifications of $v_{\langle 111 \rangle}$. (a) also shows a numerical breakdown of the calculation at $\phi = 0°$ for a $v_{\langle 111 \rangle}$ at 50 % of the nominal value. The trajectory should follow the axis.

chosen such that it results in a good illumination of the crystal and the probability that a photon deposits all its energy in one segment is reasonably high.

The investigation of occupancy patterns in general is interesting. If such patterns are measured with a high precision, they might open a path to extract information about hole mobilities which are in general hard to measure.

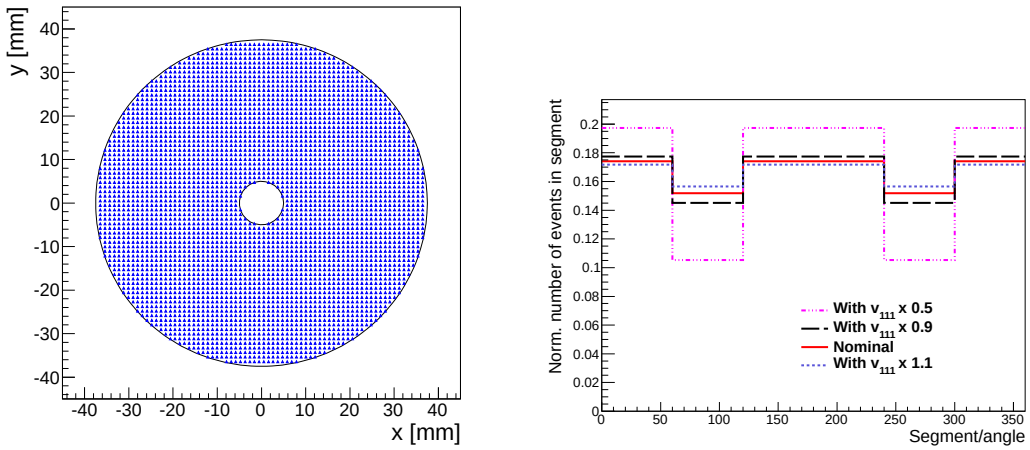

(a) (b)

Figure 7.23: (a) Distribution of hits for a simple occupancy comparison. (b) Comparison of normalized occupancies for the nominal and modified values of $v_{\langle 111 \rangle}$.

Chapter 8

Localization of the source position

Knowledge of the position of a radioactive source may be important to many applications like security in public places [106]. In low background experiments the possibility to reconstruct the location of a radioactive source may help to identify the origin of unexpected background sources. In such an experiment a segmented germanium detector or a detector array, denoted below as *detector system*, could be used. The reconstruction methods described in this chapter are based on Compton scattered events. A photon can scatter in one part and may deposit the rest of its energy in a different location of the *detector system*. The source position can be reconstructed if the deposited energies and their location are known. Key point of the method is to have a detector granularity. A single module of the *detector system* device such as a detector segment or a detector in an array will be denoted below as *granularity module*.

Two methods to reconstruct the source position will be discussed. Data taken with a segmented detector (Siegfried-II, see Section 3.5) are used to demonstrate the feasibility of the methods. In both methods, events with a single Compton-scattering occurring in one *granularity module*, segment in this case, accompanied by the full absorption of the scattered photon in a different *granularity module* were used. The *granularity module* in which the Compton scattering occurred will be denoted as S_C and the one with the full absorption as S_{FA}. An example of such an event is depicted in Fig. 8.1. The values of measured energy deposits in these two *granularity modules*, E_C and E_{FA}, can be used to extract the scattering angle, Ω, using the Compton scattering formula 3.1 from Section 3.1:

$$\begin{aligned} 1 + \frac{E_\gamma}{m_e c^2}\,(1 - \cos\Omega) &= \frac{E_\gamma}{E_{FA}}, \\ E_C + E_{FA} &= E_\gamma, \end{aligned} \tag{8.1}$$

where E_γ is the energy of the incoming photon. The locations of the corresponding energy deposits, $\boldsymbol{r}_C$ and $\boldsymbol{r}_{FA}$, cannot be determined precisely due to the finite size of the *granularity module*. As an approximation, the segment barycenters [1] are assumed as places of energy deposits. Such an approximation automatically introduces a systematic uncertainty of about 45° in θ and about 60° in ϕ.

[1] The barycenter of a segment in Siegfried-II is at radius $r = 25.4\,\text{mm}$. The z and ϕ coordinates of the barycenter correspond to the average values of segment z and ϕ, respectively.

The measured values of E_C and E_{FA} and their corresponding locations, defined by the vectors $\boldsymbol{r}_C$ and $\boldsymbol{r}_{FA}$, can only determine a conical surface of possible source positions. Figure 8.1 shows an example of such *event cone*. The following notation as from Fig. 8.1 will be used for the cone definition in space. It is unambiguously defined by the *vertex* position, $\boldsymbol{r}_C$, the *axis vector*, $\boldsymbol{v} = \boldsymbol{r}_C - \boldsymbol{r}_{FA}$, and the aperture, 2Ω.

In addition to the angular ambiguity, the values of E_C and E_{FA} can also reveal a second, complementary, cone, also shown in Fig. 8.1. The value of its aperture is defined by swapping E_C and E_{FA} in Eq. 8.1. This corresponds to the inverted order of the energy depositions. These ambiguities result in the non-capability to extract the source orientation on an event-by-event basis. Statistical methods are therefore needed.

The double-cone degeneracy can be broken by a proper selection of events. The energy E_{FA} in Eq. 8.1 is limited by the minimal value, $E_{FA,\mathrm{min}} = E_\gamma/(1 + 2E_\gamma/m_e)$, which corresponds to a back-scattering event with $\cos\Omega = -1$. If $E_{FA} < E_{FA,\mathrm{min}}$, only one event cone is possible. Such events will be denoted as *single-cone events*. Events for which both cones are energetically allowed will be denoted as *double-cone events*.

In an infinitely granular detector with a perfect energy resolution all reconstructed cones originating from different vertices intersect in the point of the source location. It can be determined using the intersection of cones from several events. Two different methods to reconstruct the source position are discussed in this chapter. The first method, denoted as *Direction method*, uses the projections of the cones on the spherical surfaces. Their intersection reveal the direction of the source but not the absolute coordinates.

In the second method, denoted as *Absolute coordinate method*, the cones and vertices are calculated and the (x, y, z) space is scanned by determining the distance from every point in space to all selected cones. In the point where the source was located, the distance should be minimal. Such a method can provide reconstruction of the source coordinates.

The two methods can be used together, iteratively.

After the work presented here was completed, it was noted that an approach similar to the *direction* method was previously used by AGATA [107, 108].

8.1 Experimental setup and simulation

The same datasets as described in Section 7.1 were used in the present analysis for both measurements and simulation. The simulation was performed using the MAGE [86] framework based on GEANT4 [87]. The sources were located in one of the positions that were shown in Fig. 7.2. In addition, the dataset with the *far top* position of the source was used in simulation. Information on the datasets is listed in Table 8.1. Spherical and Cartesian coordinate systems, depending on the method, were used. Both have their origins in the same point as in the cylindrical coordinate system described in Section 7.1.

The simulated energy deposits were assigned to segments as was discussed in Section 7.3.2.

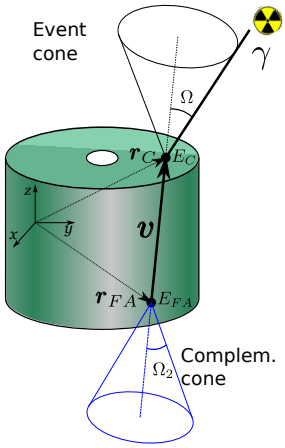

Figure 8.1: A Compton scattering event with two reconstructed cones of the source location, an *event cone*, with the source being on it, and a *complementary cone* that is reconstructed along with the *event cone*. For the notations please refer to the text.

Notation	Source, line	Source positions:	
		Spherical (r [cm], θ, ϕ)	Cartesian (x, y, z) [cm]
top position	40 kBq ^{60}Co, 1.33 MeV	(18.5, 0°, -)	(0, 0, 18.5)
top position	28 kBq ^{228}Th, 2.61 MeV	(18.5, 0°, -)	(0, 0, 18.5)
far top position	^{60}Co, 1.33 MeV	(158.5, 0°, -)	(0, 0, 158.5)
side position	23 kBq ^{228}Th, 2.61 MeV	(17.7, 97.4°, 155°)	(−16.0, 7.4, −2.3)

Table 8.1: Source configurations used in the studies. The *far top* position was only used in simulation.

8.2 Event selection

Only two-segment events of selected full absorption lines of a source, E_γ, with the following criteria were used:

- the energy measured in the core, E_0, was close to E_γ, $|E_0 - E_\gamma| < 50\,\text{keV}$;
- the energy measured in the core was close to the summed energy in two segments, $|E_0 - E_C - E_{FA}| < 50\,\text{keV}$.

In addition, the following criteria were applied in measurements:

- both segments showed energies above 150 (200) keV for 1.33 (2.61) MeV photons. This cut removes the influence from the crosstalk between the segments and the core. A detailed discussion of crosstalk can be found in Appendix A;

- neither of the two segments was Segment 9, as this segment had a bad energy resolution (see Section 3.5).

The number of selected events are summarized in Tables 8.2 and 8.3 for simulated and measured data, respectively. The minimal energy deposited in S_{FA} are $E_{FA,\mathrm{min}} = 233\,\mathrm{keV}$ for a 2.6 MeV photon and $E_{FA,\mathrm{min}} = 214\,\mathrm{keV}$ for a 1.33 MeV photon which are very close to the cut values of 150 keV and 200 keV, respectively, due to the crosstalk. This results in a significant reduction of single-cone events for the measured datasets.

	1.33 MeV, top	2.61 MeV, top	2.61 MeV, side
Total events	100 000	100 000	100 000
Two-segment events with $E_C + E_{FA} = E_\gamma$	10 813	7 117	6 720
Number of reconstructed cones (incl. complementary cones)	18 528	12 278	11 604
among which:			
number of single-cone events	3 098	1 956	1 836
number of double-cone events	7 715	5 161	4 884

Table 8.2: Number of events and reconstructed cones in the corresponding datasets in **simulation**.

	1.33 MeV, top	2.61 MeV, top	2.61 MeV, side
Total events	1 000 000	2 023 680	785 664
Two-segment events with $E_C + E_{FA} = E_\gamma$	28 003	22 664	9 066
Number of reconstructed cones (incl. complementary cones)	51 445	43 288	17 296
among which:			
number of single-cone events	4 561	2 040	836
number of double-cone events	23 442	20 624	8 230

Table 8.3: Number of events and reconstructed cones in the corresponding datasets in **measurements**.

8.3 Direction method

The position of a localized γ-source can be determined using intersections of a set of cones. The structure of the intersections is complicated in three dimensions, therefore a simplified approach was taken. Each cone was projected onto a spherical surface centered in the cone *vertex*, resulting in a circular intersection curve in space (see Fig. 8.2(a)). The displacement of cone *vertices*, i.e. the difference in the location of *granularity modules*,

was neglected for the sake of simplification. This determines the limitation of the method to the cases where the source is relatively far from the *detector system*. More detailed discussion will be given in Section 8.5.

In case the cone *vertex* is placed in the center of a sphere, the intersection of the cone with the sphere can be described by the relation between the polar, θ, and the azimuthal, ϕ, coordinates as (for the derivation refer to Appendix C):

$$\cos(\phi - \phi_0)\ \sin\theta\ \sin\theta_0 = \cos\Omega - \cos\theta\ \sin\theta_0 \tag{8.2}$$

where θ_0 and ϕ_0 are the spherical coordinates of the *axis vector* $\boldsymbol{v}$. An example of a cone intersection is depicted in Fig. 8.2(a). Please note that the r dependence cancels out. This would not be the case if the cone *vertex* was placed elsewhere than in the center of the sphere. It also means that this algorithm can only determine the direction of the source position, but not its real position.

The dependence $\phi(\theta)$ was plotted onto a 2D-histogram with 2° bin width in both θ and ϕ. An example of the resulting pattern for several cones is shown in Fig. 8.2(b). By histogramming intersection positions of a set of events the bins corresponding to the source direction will have the most entries.

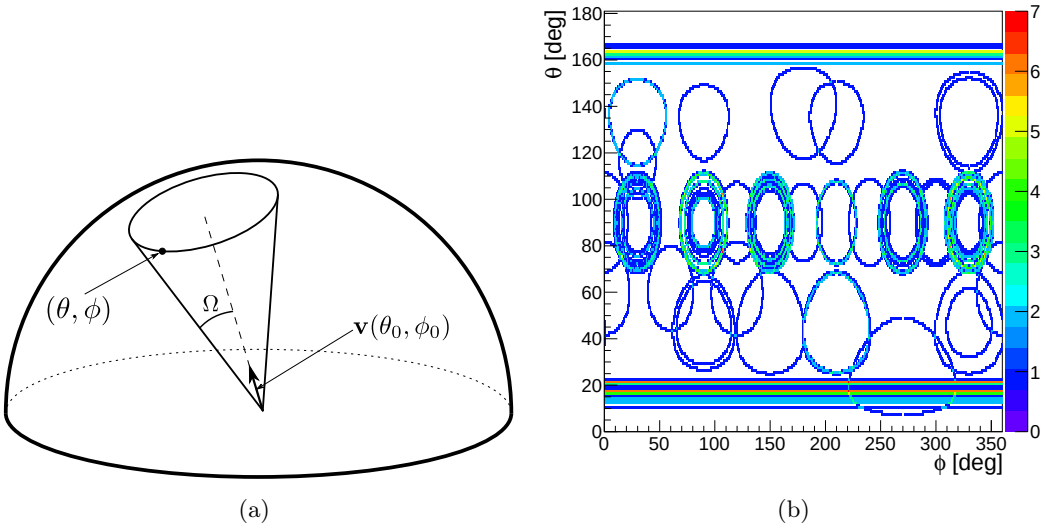

(a) (b)

Figure 8.2: (a) A cone intersection with a sphere. The equation of the intersection, $\phi(\theta)$ is described in the text. (b) Examples of the cone projections in $\theta - \phi$ for a set of events. The color palette reflects the number of bin entries.

The method was tested using measurements and simulation with 1.33 MeV photons from ^{60}Co and 2.6 MeV photons from ^{228}Th. The results of the simulation are shown in Fig. 8.3. Prominent lines at $\theta \approx 23°$ in Fig. 8.3(a) and $\theta \approx 12°$ in Fig. 8.3(b) hint for a relative top position of the source. This was indeed the case. The deviation from 0° in θ is determined by the cone *vertices* not being at the same location. These are the angles at which the source is seen from the corresponding segment pairs.

The pattern shown in Fig. 8.3(c) hints for a source position at $\phi \approx 150°$, $\theta \approx 90°$ and again well corresponds to the simulated position.

Figure 8.3(d) shows the pattern for a combined dataset of the *side* position and the *top* position. It represents the case where two point-like sources irradiated the detector simultaneously. In this case both source directions can be recognized.

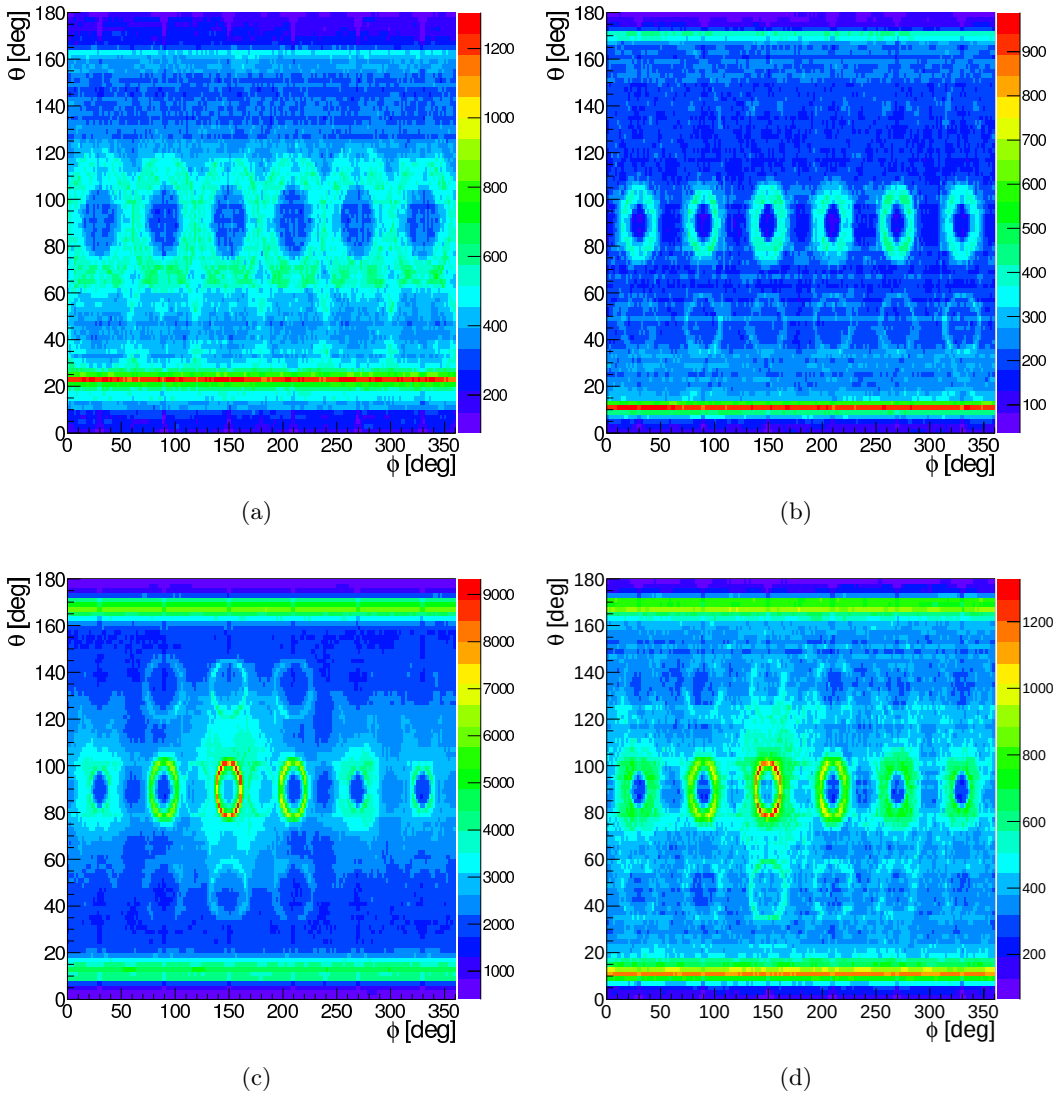

Figure 8.3: Distributions of the reconstructed cone projections in **simulation** for (a) 1.33 MeV line, *top* source position, (b) 2.6 MeV line, *top* source position and (c) 2.6 MeV line, *side* source position (d) 2.6 MeV, combined *top* and *side* set. The color palette reflects the number of bin entries.

The direction of the source, (θ_S, ϕ_S), can be calculated as the barycenter of the θ, ϕ

pattern using its values in each bin, $P_{i,j}$:

$$\theta_S = \frac{\sum_{i,j} \theta_i \cdot P_{ij}}{\sum_{i,j} P_{ij}}$$
$$\phi_S = \frac{\sum_{i,j} \phi_i \cdot P_{ij}}{\sum_{i,j} P_{ij}} \tag{8.3}$$

where i and j denote bins of θ and ϕ, respectively. To remove background, only bins with $P_{i,j} > 0.9 \cdot P_{\max}$ were considered, where $P_{\max}$ corresponds to the highest bin content.

The reconstructed average source directions, $\langle(\theta, \phi)\rangle$, and the deviations from the true positions $\Delta(\theta, \phi)$, are summarized in Table 8.4. For the pattern shown in Fig. 8.3(d) the source positions was also extracted by independently averaging the corresponding parts of the pattern, $20 < \theta < 160$ and outside this region.

Line, case	$(\theta, \phi)_{\text{true}}$	$\langle(\theta, \phi)\rangle$	$\Delta(\theta, \phi)$
1.33 MeV, top	(0°, -)	(23°, 178°)	(23°, -)
2.61 MeV, top	(0°, -)	(11°, 178°)	(11°, -)
2.61 MeV, side	(97°, 155°)	(92°, 151°)	(-5°, -4°)
2.61 MeV, combined	(-, -)	(80°, 163°)	-
2.61 MeV, combined,	(97°, 155°)	(90°, 151°)	(-7°, -4°)
separately reconstructed	(0°, -)	(11°, 180°)	(11°, -)

Table 8.4: The true, $(\theta, \phi)_{\text{true}}$, and extracted source orientations in **simulation** samples using the *direction* method. The last row represents the deviations between the true and the corresponding reconstructed positions. The pattern areas chosen for the separate reconstruction for the *combined* case is explained in the text.

The averaging algorithm can only be used for a single point-like source, for which a small area with high bin contents on the θ, ϕ pattern is expected. For the case with more sources, e.g. as depicted in Fig. 8.3(d), the pattern will have more such areas, and the averaging over the full pattern will give non-consistent results. The averaging in this case should be applied to different parts of the pattern separately.

The pattern reflects the type of the source. As was mentioned, for single-like sources it will have areas with high bin contents. For homogeneously distributed sources the pattern will be smoother. The type of the source can be determined visually. More precise algorithms of pattern analyses need to be developed to quantify the source homogeneity and the systematic uncertainties.

Similar patterns resulted from the measured datasets. They are shown in Fig. 8.4. As in the simulation, the reconstructed direction of the source also well correspond to the reality. The numerical results on the source orientations are listed in Table 8.5.

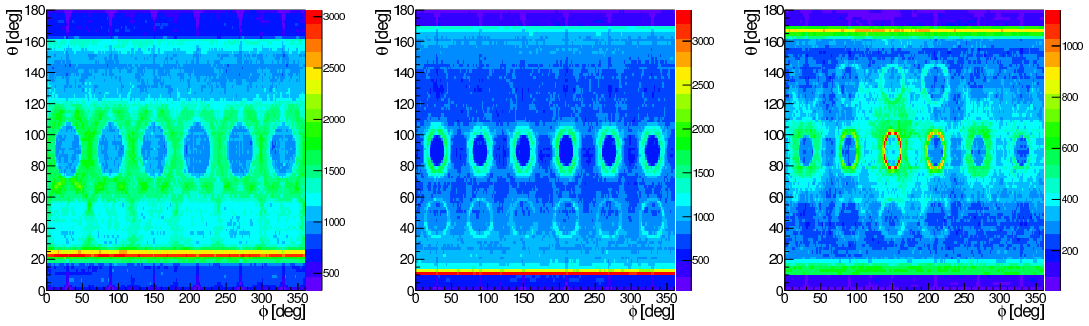

(a) (b) (c)

Figure 8.4: Distributions of the reconstructed cone projections in **measurements** for (a) 1.33 MeV line, *top* source position, (b) 2.6 MeV line, *top* source position and (c) 2.6 MeV line, *side* source position. The color palette reflects the number of bin entries.

Line, case	$(\theta, \phi)_{\text{true}}$	$\langle(\theta, \phi)\rangle$	$\Delta(\theta, \phi)$
1.33 MeV, top	(0°, -)	(23°, 176°)	(23°, -)
2.61 MeV, top	(0°, -)	(11°, 180°)	(11°, -)
2.61 MeV, side	(97°, 155°)	(90°, 150°)	(-7°, -5°)

Table 8.5: The true, $(\theta, \phi)_{\text{true}}$, and extracted source orientations in **measurements** using the *direction* method. The last row represents the deviations between the true and the corresponding reconstructed positions.

8.4 Absolute coordinate method

The position of the source can also be determined by scanning the full surrounding space and by determining the point that has the smallest average distance to all the cones. For a given point in space, $\boldsymbol{x}_0$, a measure, $\mathcal{M}$, to quantify the distance from the point to the reconstructed cones is calculated. The definition of $\mathcal{M}$ can be chosen according to the following requirement: for a point that lies on the cone $\mathcal{M}$ is zero. The closer it is to the cone, the smaller $\mathcal{M}$ should be. Using such a requirement, the following two measures were tested:

1. minimal linear distance, h, between the point $\boldsymbol{x}_0$ and the cone with vertex $\boldsymbol{x}$. It is calculated as demonstrated in Fig. 8.5. Using notations from the figure, the value of h can be calculated as

$$\cos(\beta + \Omega) = \frac{\boldsymbol{v} \cdot \boldsymbol{L}}{v\ L} \Rightarrow \beta = \arccos\left(\frac{\boldsymbol{v} \cdot \boldsymbol{L}}{v\ L}\right) - \Omega \tag{8.4}$$

$$h = \begin{cases} L\ \sin\beta & |\beta| < 90°, \\ L & \text{otherwise} \end{cases} \tag{8.5}$$

2. minimal angular distance to the cone, $|\beta|$ in Fig. 8.5.

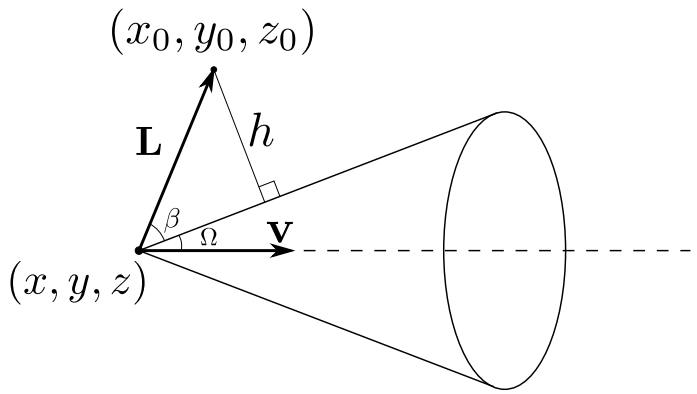

Figure 8.5: Definition of the distance measures $\mathcal{M}$, linear h and angular β, between cone with vertex $\boldsymbol{x}$ and point $\boldsymbol{x}_0$.

The usage of the linear measure h did not show any outstanding results. Considering the uncertainties of r_C and r_{FA} on the level of the segment size, ∼cm, the minimal value of h was obtained for the points inside the detector or close to it. Cuts, e.g. taking only the event cones with $|\beta| < 90°$ or regions inside(outside) the cones with $\beta < (>)0°$, did not help. Most probably, detectors with segmentation of the size of Siegfried-II cannot be used along with the linear distance measure.

The angular distance β does not have such a strong impact from segmentation and can be used with segmented detectors. The measure was defined as the averaged angular distance to the cones surviving the cut $|\beta| < 90°$. In each source position 1000 reconstructed cones were considered. The number of cones used was optimized to get a sufficient accuracy and reasonable processing time.

The resulting distribution of β in space is a 3D-histogram, i.e. a 4D-structure. It was projected onto XY, YZ and XZ planes onto a set of 2D histograms. Candidates for the source positions are found by determining the minima in the projections. This can be done visually for all the projections. To quantify the most likely source position, the barycenter of the pattern, $\boldsymbol{x}_S$, can be determined by summing over all positions using the inverted measures β as the weights for individual positions:

$$\boldsymbol{x}_S = \frac{\sum_{ijk} \boldsymbol{x}_{ijk}/\beta_{ijk}}{\sum_{ijk} 1/\beta_{ijk}} \tag{8.6}$$

where the sum indices i, j and k denote the bins of x, y and z coordinates, respectively. To cut points in space that have very high distances to the cones, only those bins having their bin content below a threshold value $\beta_{\text{threshold}}$ were considered. The value of $\beta_{\text{threshold}}$ was taken to be above the minimal β by 30 % of the difference between the maximal and the minimal values of β, $\beta_{\text{threshold}} = 0.7 \cdot \beta_{\text{min}} + 0.3 \cdot \beta_{\text{max}}$, where β_{min} and β_{max} denote the minimal and the maximal values, respectively.

The measures β were calculated for points in space contained in a box of varied width with 50 steps along each dimension. The center of the box was always positioned at the center of the coordinate system. Examples of the projections onto planes close to the simulated source position (see Table 8.1) are shown in Figure 8.6(a–c) for the 1.33 MeV line, *top* position. Figure 8.6(d) represents a plane that is far from the expected source position.

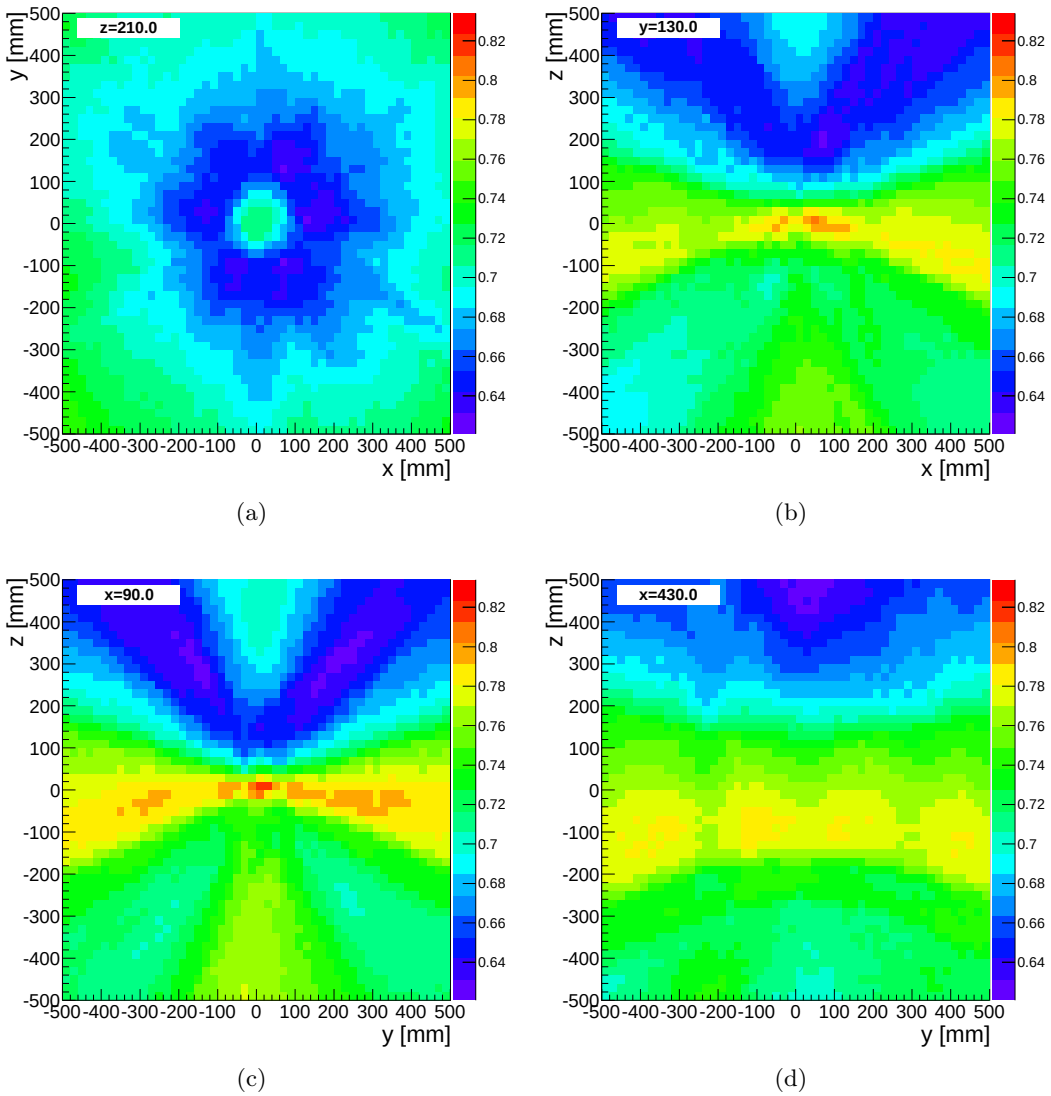

Figure 8.6: The projections of the measure β for 1.33 MeV Cobalt-line for the *top* source position at (0 cm, 0 cm, 18.5 cm) in **simulation**: (a) in XY plane at $z = 210$ mm, (b) in XZ plane at $y = 130$ mm, (c) in YZ plane at $x = 90$ mm, (d) in YZ plane at $x = 430$ mm. The color code represents the β-value for individual positions.

Similar patterns result for the 2.6 MeV line. They are depicted in Figs. 8.7(a)–8.7(d). Figures 8.7(c) and 8.7(d) represent a different pattern representation, showing the value of the measure as the third coordinate of the histogram[2].

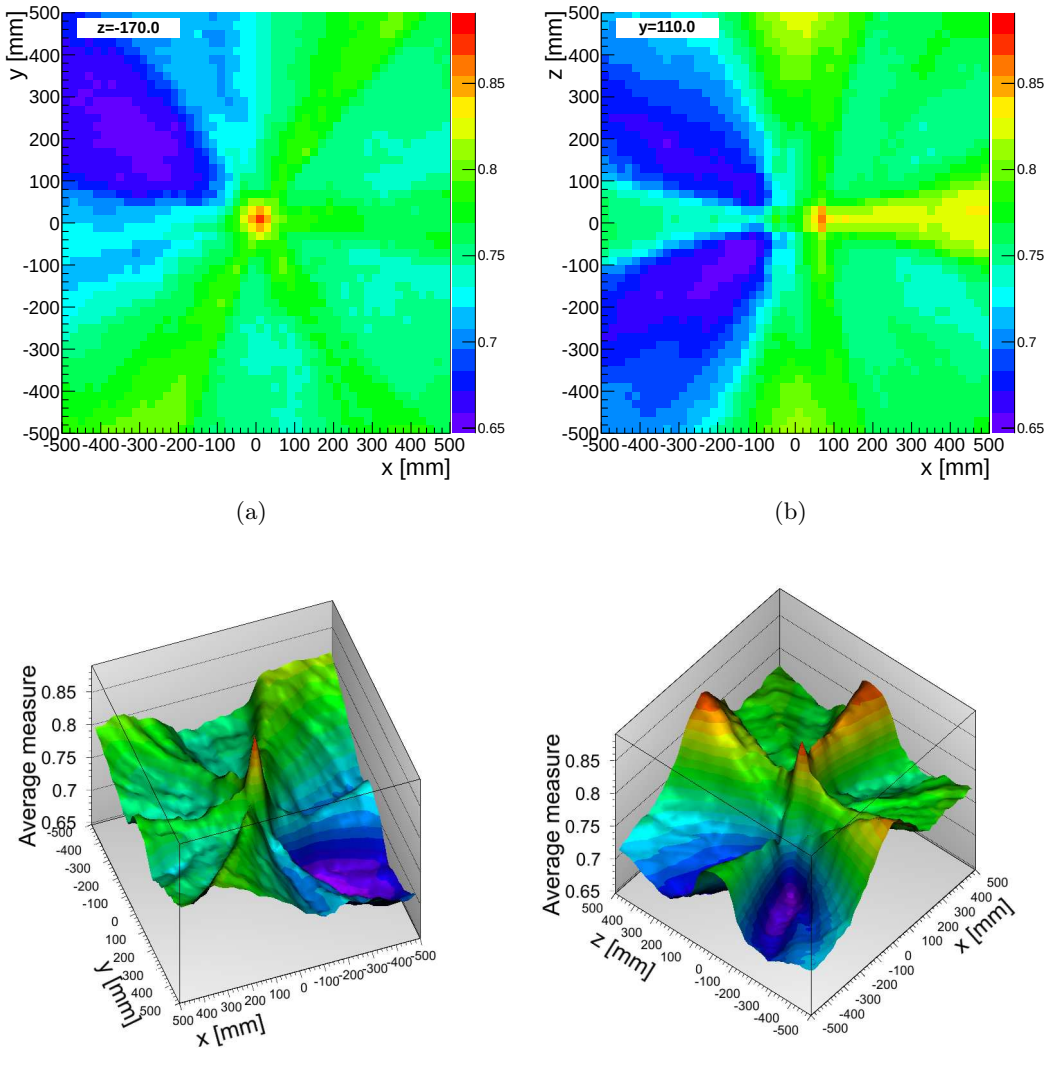

(a) (b)

(c) (d)

Figure 8.7: The projections of the measure β for 2.61 MeV Thallium-line for the *side* source position at (-16 cm, 7.4 cm, -2.3 cm) in **simulation**: (a) in XY plane at $z = -170$ mm, (b) in XZ plane at $y = 110$ mm, (c) in XY plane at $z = -130$ mm, (d) in XZ plane at $y = 90$ mm. The color code represents the β-value for individual positions.

[2]Not to confuse the z coordinate of the point $\boldsymbol{x}_0$ and the third dimension, the color code, of the histogram.

Tables 8.6–8.8 summarize the calculated barycenters for different source positions and box widths. Also listed are the distance between the reconstructed and the simulated position, $|\Delta\boldsymbol{x}|$. Depending on the box width, the results differ. The quality of the reconstruction can be controlled by a quality parameter defined as

$$\mu = \sum_{ijk} \left(\beta_{ijk} - \overline{\beta}\right)^2, \tag{8.7}$$

where $\overline{\beta}$ is the average value of β over the full considered space. For the sum, all bins are considered without a threshold value. The parameter μ is related to the inhomogeneity of β in space. If the space box is too small and does not contain the point of the source position, the measures β will always be large and their distribution tends to be smooth. Thus, the value of μ will be small. With the increasing size the box approaches the position in space where the source is located. The measure drops for some bins and the inhomogeneity, and thus μ, increases. Once the box extends far away from the source position, the quality parameter will be dominated by the many bin contents with big difference and thus μ will be high. Quantitatively, the size of the box needed for good accuracy corresponds can be determined by finding the steepest rise of μ with increase of the box size. Such a behavior is seen in Tables 8.6–8.7 for the *top* position of 1.3 MeV and 2.6 MeV sources. A 20 cm wide box does not contain the source. Increasing its size to include the source location significantly increases μ. For the *side* source case, the box of 20 cm is close to contain the source location. The value of μ is thus approximately constant with increasing box width.

The situation is not clear for the *far top* position. The value of μ does not change smoothly with increasing box size, see Table 8.6. It indicates that the method does not provide a sufficient spatial resolution for large source distances. The direction of the reconstructed source position nevertheless corresponds to the simulated one.

For the *combined set*, the reconstructed source position is located very close to the detector, even for large box sizes, which does not correspond to any of the true positions of either sources, see Table 8.8. The existence of more than one source in this case results in the averaged out reconstructed position, close to the detector. Such cases should be investigated in details. For example, the direction of the most prominent source can be

Box size	1.33 MeV, top $\boldsymbol{x}_{S,\text{true}} = (0, 0, 18.5)$ cm			1.33 MeV, far top $\boldsymbol{x}_{S,\text{true}} = (0, 0, 158.5)$ cm		
	$\boldsymbol{x}_S$	$\lvert\Delta\boldsymbol{x}\rvert$ [cm]	μ	$\boldsymbol{x}_S$ [cm]	$\lvert\Delta\boldsymbol{x}\rvert$ [cm]	μ
20 cm	(-0.3, 0.6, 7.9)	10.6	207	(-1.1, 0.4, 7.5)	151.0	276
40 cm	(-1.3, 0.7, 14.5)	4.3	243	(-1.9, 1.0, 14.4)	144.1	336
100 cm	(-3.8, 1.3, 34.7)	16.7	251	(-4.2, 2.3, 34.8)	123.8	365
200 cm	(-8.0, 2.3, 68.3)	50.5	254	(-13.4, -4.6, 71.7)	87.9	336
600 cm	(-19.9, 3.9, 215.8)	198.3	226	(-23.1, 14.3, 210.1)	58.3	355

Table 8.6: Reconstructed source positions, deviations from the true positions, $|\Delta\boldsymbol{x}|$, and μ for the *coordinate* method for **simulation** for selected box sizes. Also specified are the true source positions, $\boldsymbol{x}_{S,\text{true}}$.

Box size	2.61 MeV, top $\boldsymbol{x}_{S,\text{true}} = (0, 0, 18.5)$ cm			2.61 MeV, side $\boldsymbol{x}_{S,\text{true}} = (-16, 7.4, -2.3)$ cm		
	$\boldsymbol{x}_S$ [cm]	$\lvert\Delta\boldsymbol{x}\rvert$ [cm]	μ	$\boldsymbol{x}_S$ [cm]	$\lvert\Delta\boldsymbol{x}\rvert$ [cm]	μ
20 cm	(-1.0, -0.2, 7.9)	10.6	237	(-7.2, 5.3, -0.8)	9.2	226
40 cm	(-2.3, -0.4, 14.0)	5.1	291	(-13.3, 9.7, -0.6)	3.9	219
100 cm	(-6.0, -0.4, 30.3)	13.2	325	(-31.4, 23.2, 0.2)	22.2	226
200 cm	(-12.3, 0.3, 54.8)	38.3	337	(-61.3, 45.5, 1.9)	59.3	229
600 cm	(-37.4, 2.4, 159.4)	145.8	331	(-181.3, 134.2, 8.6)	208.6	225

Table 8.7: (continued) Reconstructed source positions, deviations from the true positions, $|\Delta\boldsymbol{x}|$, and μ for the *coordinate* method for **simulation** for selected box sizes. Also specified are the true source positions, $\boldsymbol{x}_{S,\text{true}}$.

Box size	2.61 MeV, combined		
	$\boldsymbol{x}_S$ [cm]	$\lvert\Delta\boldsymbol{x}\rvert$ [cm]	μ
20 cm	(-0.1, 2.8, 2.5)	-	174
40 cm	(-1.0, 4.5, 3.5)	-	213
100 cm	(-2.9, 9.3, 6.8)	-	234
200 cm	(-5.9, 20.2, 13.7)	-	222
600 cm	(-15.9, 64.1, 40.0)	-	206

Table 8.8: (continued) Reconstructed source positions and μ for the *coordinate* method for **simulation** for selected box sizes.

determined with the *direction* method. Regions around its expected position can be excluded from consideration in the *coordinate* method, providing information of the second source, and so on. This process can be repeated iteratively.

The results determined for measurements are listed in Table 8.9. The reconstructed source positions again well correspond to reality for box sizes containing the source, but not much exceeding it. The situation regarding the quality parameter μ is less clear in this case. This might be due to the increased number of double-cone events compared to the number of single-cone events. More investigations are necessary.

The method was tested so far with a significant number of events. This is usually not the case for low-background experiments. In this case, only a few Compton two-site events, if at all, are available. Such cases were studied. The results of the reconstruction of the source position for selected number of cones is listed in Table 8.10 for the *side* source position in simulation. The box width was 40 cm. As seen from the optimal μ value, the minimal number of cones that are needed for an operation of the method was estimated to be ≈ 100, but this number may depend on the homogeneity of the source. More detailed studies are needed.

Box size	1.33 MeV, top $\boldsymbol{x}_{S,\text{true}} = (0,\ 0,\ 18.5)$ cm			2.61 MeV, side $\boldsymbol{x}_{S,\text{true}} = (-16,\ 7.4,\ -2.3)$ cm		
	$\boldsymbol{x}_S$ [cm]	$\lvert\Delta\boldsymbol{x}\rvert$ [cm]	μ	$\boldsymbol{x}_S$ [cm]	$\lvert\Delta\boldsymbol{x}\rvert$ [cm]	μ
20 cm	(-1.1, 0.5, 7.4)	11.2	134	(-7.0, 3.0, -4.2)	10.2	193
40 cm	(-1.4, 1.7, 12.7)	6.2	145	(-14.1, 9.6, -1.9)	2.9	184
100 cm	(-4.0, 8.0, 35.1)	18.9	161	(-32.4, 26.2, -6.4)	25.3	218
200 cm	(-8.9, 0.3, 48.6)	31.4	211	(-64.5, 49.5, -24.6)	68.0	195
600 cm	(-33.2, -2.1, 206.1)	190.5	111	(-206.7, 132.2, -34.7)	230.2	157

Table 8.9: Reconstructed source positions, deviations from the true positions, $|\Delta\boldsymbol{x}|$, and μ for the *coordinate* method for **measurements** for selected box sizes. Also specified are the true source positions, $\boldsymbol{x}_{S,\text{true}}$.

Number of cones	$\boldsymbol{x}_S$ [cm]	$\lvert\Delta\boldsymbol{x}\rvert$ [cm]	μ
10	(-3.4, 6.7, -1.4)	12.7	1390
20	(-11.8, 7.6, -1.4)	4.3	1169
50	(-10.0, 4.4, 0.6)	7.3	528
100	(-10.2, 7.4, -2.3)	5.8	262
500	(-13.4, 9.7, -0.6)	3.9	222
1000	(-13.3, 9.7, -0.6)	3.9	219

Table 8.10: Quality parameter for different number of reconstructed cones for the 2.6 MeV line, *side* position. The true source position was at $\boldsymbol{x}_{S,\text{true}} = (-16,\ 7.4,\ -2.3)$ cm.

8.5 Uncertainties and discussion

The major uncertainty of both methods is connected to the granularity of the *detector system*. For the *direction* method it can be estimated as the average angular deviation of possible real trajectories from the assumed one (see Fig. 8.8). In the worst case for the Siegfried-II detector the uncertainties are approximately $\pm 60°$ in ϕ and $\pm 45°$ in θ. The usage of more events will however improve the accuracy due to averaging out of the real trajectories. The uncertainty for the *coordinate* method will depend on the angular resolution. The more distant the source is, the larger will be the coordinate uncertainties. It can be estimated as $|\Delta\boldsymbol{x}_S| \sim l_S \sin(\Delta\Omega)$, where l_S is the average distance from the *detector system* to the source and $\Delta\Omega$ is the angular resolution, either in θ or in ϕ.

If a granularity of the *detector system* is provided by detector segmentation, the anisotropy of the charge carrier drift studied in details in Chapter 7 will result in different effective segment volumina. This will cause shifts in the corresponding segment barycenters that are used as the locations of the energy deposits. The systematic uncertainty can be up to $10°$ in θ which is the maximum deviation of the charge carrier drift [71].

A sufficient resolution of the *coordinate* method can be obtained if the source is located relatively close to the *detector system*, e.g. within $\sim 10\,l$ around it, where l is the distance

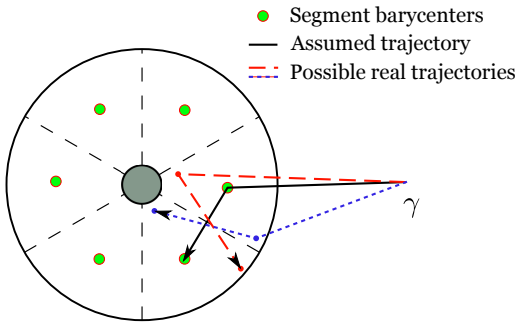

Figure 8.8: Possible trajectories of a photon and the assumed trajectory used for the reconstruction.

between individual *granularity modules* of a system, e.g. between detector segments. For a source located further away, only its direction can be reliably reconstructed.

The cone intersection algorithm of the *direction* method contains a simplifying approximation. The coordinates of the cone *vertices* are not taken into account. The coordinate system originates from all the *granularity modules*, for each cone. If the source is far from the *detector system*, $\gtrsim 10\,l$, the location of the *vertices* can be approximated to be the same, e.g. in the center of the *detector system*. In this case the θ, ϕ pattern will peak at the corresponding source direction which can be well reconstructed. If the source is close enough to the *granularity modules*, or is within them, the θ, ϕ pattern will have several peaks, corresponding to the angles, at which the source is "seen" from different *granularity modules*. In comparison to the *coordinate* method, the source should be further from the detectors than $\sim 10\,l$.

A more efficient position reconstruction can be supplemented by additional information, if available, from the *detector system*, such as the relative intensities of the corresponding gamma lines in individual *granularity modules*. Those closer to the source will register more events in the energy spectrum for the gamma line considered. For a segmented detector, the precision of both methods can be increased by more precise determination of the location of energy deposits within the segments using mirror pulses, described in Ref. [67]. Technically it is however more complex as it requires the collection of the pulse shapes during data taking, which significantly increases the amount of recorded and analyzed data, and additional event location reconstruction algorithms.

8.6 Summary

The position of radioactive contaminations can be reconstructed using back-tracking methods applied to a granular device such as a segmented detector or a detector array. For some source configurations, the direction of the source and even its position can be reconstructed. Two methods to do so were proposed.

It was shown that the source direction can be identified by the *direction* method. This method shows best performance if the source is located at distances significantly further

then the size of the *detector system*. If it is located relatively close to the detectors, the (x, y, z) position can be reconstructed using the *absolute coordinate* method. For both methods, more elaborate algorithms of the pattern analysis need to be developed to estimate the source homogeneity and the systematic uncertainties as well as to improve the spatial resolution.

Both methods can and should be used iteratively, especially if the source configuration is complex, like existence of several sources or a homogeneously distributed source.

Summary and conclusions

The success of low background experiments searching for rare events depends on how well the detector and the background sources are understood. The lower the expected event rate is, the more essential it becomes to fully understand all effects influencing the performance of an experiment. The lower the background rate is that has to be achieved, the more effects that could be safely neglected previously, have to be taken into account.

This thesis covered four main topics:

- investigation of possible background sources in GERDA and future experiments and pulse shape analysis methods to suppress these;
- studies of the temperature dependence of the pulses produced by high purity germanium detectors;
- analysis of the transverse anisotropy in germanium crystals and determination of the crystallographic axes in a segmented detector;
- reconstruction of the origin of γ-radiation using the granularity of the detectors.

The first topic is connected to the sensitivity to be achieved in the second phase of the GERDA experiment which requires a background level of the order $10^{-3}\,\mathrm{cts/(kg{\cdot}yr{\cdot}keV)}$ in the energy region of interest; the present value is $\sim 10^{-2}\,\mathrm{cts/(kg{\cdot}yr{\cdot}keV)}$. In this thesis, simulations concerning the following possible contributions to the background in GERDA Phase II or future experiments were discussed:

- the silver isotopes ^{108m}Ag and ^{110m}Ag have been measured in the signal cables. The resulting background index predicted from simulations is below $10^{-6}\,\mathrm{cts/(kg{\cdot}yr{\cdot}keV)}$ in the energy region of interest for both isotopes and will not be significant for GERDA Phase II;
- the thorium isotope ^{228}Th is present in the filling material of the GERDA cleanroom floor. The predicted background index is less than $2 \cdot 10^{-5}\,\mathrm{cts/(kg{\cdot}yr{\cdot}keV)}$. This contamination does not contribute significantly to the background in GERDA Phase II.
- other contaminations are expected in the metalization of the detectors. The resulting background indices are significant for a future tonne-scale high purity germanium,

HPGe, experiment with background requirements one or two orders of magnitude more restrictive than GERDA.

A pulse shape analysis using artificial neural networks, ANN, was used to distinguish between signal-like and background-like events. Systematic effects influencing the results were investigated. It was shown that the ANN method is working quite well. However, it is systematically biased according to the spatial distribution of the events used to train the ANN. The efficiency of the method to recognize signal-like events is $\approx 70\,\%$ with an overall uncertainty of about $10\,\%$.

The second topic of the temperature dependence of pulse shapes was studied operating a segmented 18-fold n-type prototype HPGe detector in the temperature range from 77 K to 130 K. This generously covers the usual temperature range of HPGe detector operation. The temperature dependence of the pulses length was measured. A strong dependence was found. The lengths of the pulses increase by almost $50\,\%$ at 130 K as compared to 77 K. Any analysis of pulse shapes has to take this into account. The measured temperature dependence does not agree with simple model predictions. Possible explanations for this discrepancy were given. The pulse amplitude was measured to be stable in the temperature range of 77 K to 130 K. This shows that energy measurement with HPGe detectors are insensitive to temperature variations and that HPGe detectors can be operated stably at relatively high temperatures.

The third topic was the effects of the transverse crystal anisotropy in germanium. This anisotropy strongly influences the drift paths of the charge carriers and thus has to be taken into account for any pulse shape simulation. In this thesis, a novel method was presented how to determine the orientation of the crystallographic axes from a single measurement with a radioactive source using the transverse anisotropy. The method is based on the comparison of simulated to measured occupancy patterns seen in the segments of a ϕ-segmented detector. The overall accuracy of the reconstructed axis orientation is about $10\,^\circ$. The method was compared to the well-established scanning method and the sources of systematic uncertainty were carefully studied. They are, in the order of importance, the misalignment of the source position, presence of background, choice of the test statistic, assumption on the impurity density of the detector. The method can be used in any detector configuration and with any calibration source as long as the setup can be simulated with sufficient precision.

The fourth topic is connected to the necessity to identify background sources by measuring the direction and distance from which the radiation comes and, if possible, eliminate them. The granularity of a radiation detector system, such as the segments of a detector, or the detectors in an array, can be used using fully absorbed Compton scattering events. Two methods were developed and tested using again the segmented 18-fold n-type prototype HPGe detector. The method that determines the direction of the source works best for a distant source. In a complementary way, the method to determine the absolute (x, y, z) position works better for close sources. Around 100 fully absorbed Compton events are

needed for a successful application of the methods.

From the results obtained on the four topics, it can be concluded that pulse shapes are a powerful tool to understand the data obtained by germanium detectors. However, the systematic effects connected to detector configurations and environmental conditions need to be very well understood. Segmented detectors are an ideal tool to study such systematic effects. They could also be used for future experiments in order to reduce the systematic uncertainties for a large detector device.

Appendix A

Crosstalk

Occupancies can be changed by crosstalk. This could make the usage of occupancies in an analysis impossible. Therefore, the crosstalk between different channels of the detector was investigated and a method to correct for crosstalk was developed.

A segmented detector always has an internal capacitive coupling between the segments, resulting in some charge induced on the other segments. This effect leads to problems in the energy calibration which is usually done with single-segment events. For multi-segment events, this results in events where the core energy not equals the sum of the calibrated segment energies. The problem was investigated in detail for the AGATA detectors [109]. For the present analysis, only single segment events were considered and only the number of events was used. Therefore, the effect of capacitive coupling was not taken into account.

The second type of crosstalk, caused by the proximity of read-out cables or other electronic effects, leads to signals induced on neighboring cables or channels. As a result, all channels can be coupled. The effect can be described by a matrix[1]:

$$\begin{pmatrix} E'_0 \\ \hline E'_1 \\ \cdots \\ E'_{18} \end{pmatrix} = \left(\begin{array}{ccccc} 1 & \alpha_{0,1} & \alpha_{0,2} & \cdots & \alpha_{0,18} \\ \hline \alpha_{1,0} & 1 & \alpha_{1,2} & \cdots & \alpha_{1,18} \\ \vdots & \vdots & \vdots & \ddots & \vdots \\ \alpha_{18,0} & \alpha_{18,1} & \alpha_{18,2} & \cdots & 1 \end{array}\right) \times \begin{pmatrix} E_0^{\text{true}} \\ \hline E_1^{\text{true}} \\ \cdots \\ E_{18}^{\text{true}} \end{pmatrix}, \tag{A.1}$$

or $\vec{E}' = \hat{\alpha} \cdot \vec{E}^{\text{true}}$, where E_i^{true} is the amplitude of the signal in segment i, and E'_i is the corresponding amplitude of the signal that enters the DAQ. The core channel is denoted with the index 0. Assuming that the core signal is amplified inside the cryostat, it causes the largest crosstalk to the segments, i.e. the first column of the matrix $\hat{\alpha}$ is significantly

[1] In the present chapter, the following special notations will be used to emphasize the corresponding structures:

- an arrow for a vector, e.g. $\vec{A}$;
- a hat for a matrix, e.g. $\hat{A}$;
- a variable without a special symbol is assumed to be a scalar

larger then all other non-diagonal elements. It mostly affects the channels on the same feedthrough. The effect of segment-core crosstalk is compensated by the core calibration procedure. The energies are measured in ADC counts, the so called MCA[2] energies. After digitizing, the MCA energies equal $E_k^{\mathrm{MCA}} = C_k \cdot E'_k$ with the digitizing constants C_k, or in the matrix form

$$\vec{E}^{\mathrm{MCA}} = \hat{C} \cdot \vec{E}' = \hat{C} \cdot \hat{\alpha} \cdot \vec{E}^{\mathrm{true}}. \tag{A.2}$$

The matrix $\hat{C}$ is diagonal. The crosstalk matrix can be determined using single segment events, for which the singular segment energy vector is

$$\begin{pmatrix} E_0^{\mathrm{true}} \\ \hline \\ \vdots \\ 0 \\ E_k^{\mathrm{true}} \\ 0 \\ \vdots \end{pmatrix}. \tag{A.3}$$

The following equations have to be solved:

$$E_j^{\mathrm{MCA}} = C_j \cdot E_j^{\mathrm{true}} + C_j \cdot \alpha_{j,0} \cdot E_0^{\mathrm{true}} + \sum_{\substack{i=1 \\ i \neq j}}^{18} C_j \cdot \alpha_{j,i} \cdot E_i^{\mathrm{true}} = 0 + C_j \cdot \alpha_{j,0} \cdot E_0^{\mathrm{true}} + C_j \cdot \alpha_{j,k} \cdot E_k^{\mathrm{true}}. \tag{A.4}$$

For single segment events, $E_0^{\mathrm{true}} = E_k^{\mathrm{true}}$ and in the sum only one term remains, i.e. $E_i^{\mathrm{true}} = 0$ for $i \neq k$. Assuming that the core signal is not affected by the segments, $E_0^{\mathrm{MCA}} = C_0 \cdot E_0^{\mathrm{true}}$. The division of Eq. A.4 by E_0^{MCA} yields:

$$\frac{E_j^{\mathrm{MCA}}}{E_0^{\mathrm{MCA}}} = \frac{C_j \cdot \alpha_{j,0} \cdot E_0^{\mathrm{true}}}{C_0 \cdot E_0^{\mathrm{true}}} + \frac{C_j \cdot \alpha_{j,k} \cdot E_k^{\mathrm{true}}}{C_0 \cdot E_0^{\mathrm{true}}} = \frac{C_j}{C_0} \cdot \alpha_{j,0} + \frac{C_j}{C_0} \cdot \alpha_{j,k}. \tag{A.5}$$

In a first step, the influence of the core onto the segments is considered to be dominating. For this assumption, the term $\frac{C_j}{C_0} \cdot \alpha_{j,k}$ is neglected, i.e. no segment-segment crosstalk is taken into account. The ratio from Eq. A.5 is calculated as follows. First, the segments and the core were calibrated without crosstalk corrections, using the full absorption peaks of the 2.6 MeV line from ^{208}Tl and the 1.33 MeV line from ^{60}Co. This was done in order to be able to select single segment events by requiring the segment energy to be close to the core energy, $|E_0^{\mathrm{meas}} - E_k^{\mathrm{meas}}| < 50\,\mathrm{keV}$, i.e. the calibrated values are required. The distributions of the ratios $E_j^{\mathrm{MCA}}/E_0^{\mathrm{MCA}}$ were analyzed. In a general case with a pronounced crosstalk, a peak at about 0.02 is observed. Figure A.1 shows an example where the peak is observed at 0.012. The ratio in Eq. A.5 is calculated as the peak center as fitted with a Lorentz function.

[2]Multi Channel Analyzer

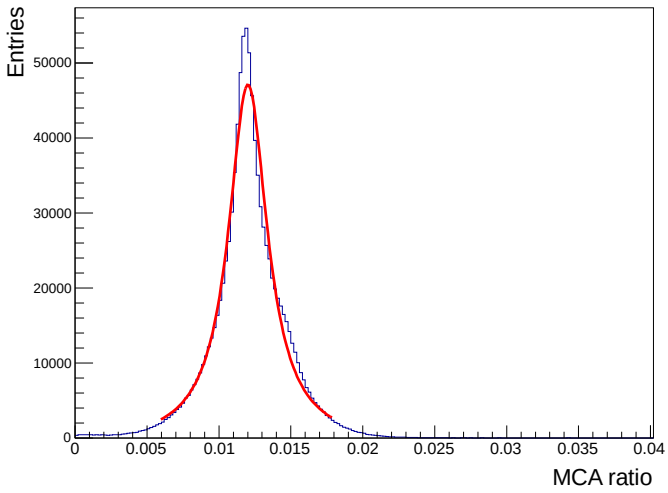

Figure A.1: Examples of the ratio spectrum of $E_6^{\mathrm{MCA}}/E_0^{\mathrm{MCA}}$. Also shown is a Lorentz fit.

The corrected values of the MCA energies, $\vec{E}^{\mathrm{MCA,corr}}$, are then calculated from Eq. A.2:

$$\vec{E}^{\mathrm{MCA,corr}} = \hat{C} \cdot \vec{E}_{\mathrm{true}} = \hat{C} \cdot \hat{\alpha}^{-1}\hat{C}^{-1} \cdot \vec{E}_{\mathrm{MCA}}. \tag{A.6}$$

Since $\hat{C}$ is diagonal, only two terms remain:

$$E_j^{\mathrm{MCA,corr}} = E_j^{\mathrm{MCA}} + \frac{C_j}{C_0} \cdot (\hat{\alpha}^{-1})_{j,0} \cdot E_0^{\mathrm{MCA}}. \tag{A.7}$$

At this stage, the inverted matrix $\hat{\alpha}^{-1}$ has the simple form:

$$\hat{\alpha}^{-1} = \begin{pmatrix} 1 & 0 & 0 & \cdots & 0 \\ \hline \alpha_{1,0} & 1 & 0 & \cdots & 0 \\ \vdots & \vdots & \vdots & \ddots & \vdots \\ \alpha_{18,0} & 0 & 0 & \cdots & 1 \end{pmatrix}^{-1} = \begin{pmatrix} 1 & 0 & 0 & \cdots & 0 \\ \hline -\alpha_{1,0} & 1 & 0 & \cdots & 0 \\ \vdots & \vdots & \vdots & \ddots & \vdots \\ -\alpha_{18,0} & 0 & 0 & \cdots & 1 \end{pmatrix}. \tag{A.8}$$

The corrected energies are:

$$\boxed{E_j^{\mathrm{MCA,corr}} = E_j^{\mathrm{MCA}} - \left(\frac{C_j}{C_0} \cdot \alpha_{j,0}\right) \cdot E_0^{\mathrm{MCA}}.} \tag{A.9}$$

The segment-segment crosstalk matrix elements $\hat{\alpha}$ can not be determined together with the core-segments crosstalk. This can be illustrated by a simple example. Imagine a single segment event with an energy deposition in segment 1:

- Energy in segment 1: $E_1^{\mathrm{meas}} = 1\,\mathrm{MeV}$ that corresponds to MCA energy of $E_1^{\mathrm{MCA}} =$ 2000 MCA;
- Energy as seen by the core: $E_0^{\mathrm{meas}} = 1\,\mathrm{MeV}$ and this corresponds to the core MCA energy of $E_0^{\mathrm{MCA}} = 4000$ MCA;

- Induced charge in segment 2: $E_0^{\mathrm{MCA}} = 40$ MCA.

The ratios become $E_2^{\mathrm{MCA}}/E_0^{\mathrm{MCA}} = 0.01$ and $E_2^{\mathrm{MCA}}/E_1^{\mathrm{MCA}} = 0.02$. If both core-segment and segment-segment crosstalk are corrected simultaneously, the corrected MCA energy in segment 2 according to Eq. A.9 would be but including the segment-segment term:

$$E_2^{\mathrm{MCA,corr}} = E_2^{\mathrm{MCA}} - \left(\frac{C_2}{C_0} \cdot \alpha_{2,0}\right) \cdot E_0^{\mathrm{MCA}} - \left(\frac{C_2}{C_1} \cdot \alpha_{2,1}\right) \cdot E_1^{\mathrm{MCA}}. \tag{A.10}$$

Considering that the elements of the matrix $\hat{\alpha}$ are small, the result would be $E_2^{\mathrm{MCA,corr}} = 40 - 0.01 \cdot 4000 - 0.02 \cdot 2000 = -40$, i.e. the crosstalk was double counted. This is the consequence of having a single-segment energy vector in A.3 with two non-zero components.

After the first step is performed, the segments are corrected for the core-segment crosstalk. The correction of segment-segment crosstalk can be done in a second step. Single segment events in segment k can be used to calculate the terms $\left(\frac{C_j}{C_k} \cdot \alpha_{j,k}\right)$ to be used in Eqs. A.4 and A.6.

The crosstalk was the largest for Run 6, see Section 3.5, where the core read-out cable was connected on the same feedthrough as several segments. It reached values of up to 10 %. It was reduced for Run 7 by moving the core read-out cable to a separate feedthrough, as shown in Fig. 3.8. For data taken during Run 6, some ratios $E_j^{\mathrm{meas}}/E_0^{\mathrm{meas}}$ clearly have a second peak, see Fig. A.2(a).

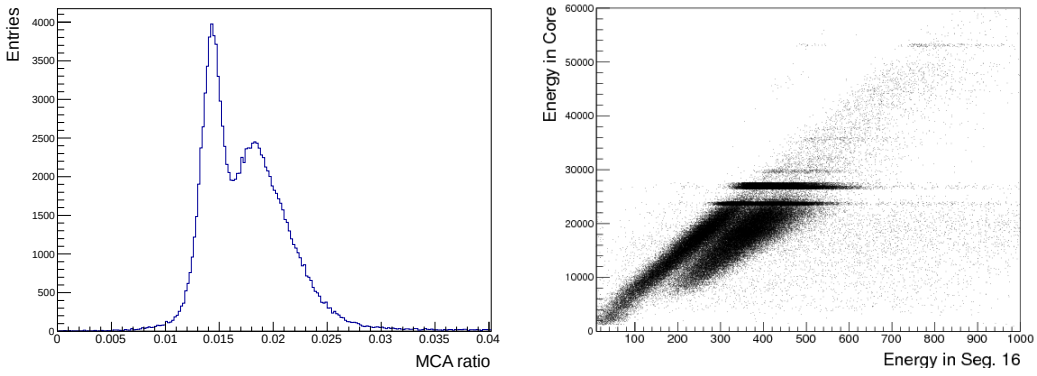

(a) $E_{16}^{\mathrm{MCA}}/E_0^{\mathrm{MCA}}$ (b) Scatter plot E_{16}^{MCA} vs E_0^{MCA}

Figure A.2: (a) An example of the appearance of a double peak in the distribution of $E_{16}^{\mathrm{MCA}}/E_0^{\mathrm{MCA}}$ and (b) the corresponding scatter plot E_{16}^{MCA} versus E_0^{MCA}.

The origin of this peak was investigated and identified as noise. Figure A.3 demonstrates this. The trigger cuts all the events below a given threshold, 100 keV for Fig. A.3(a), with some Fermi-like efficiency, a sigmoid on Fig. A.3(a). Since the noise is random, events of this kind can be picked by the trigger. The sum of noise and crosstalk from the core results in the second peak in the ratio spectrum. The effect is also clearly seen when looking at the scatter plot shown in Fig. A.2(b). The correction for crosstalk with noise is

difficult and could not be performed. Runs affected by this have to be used with a high off-line energy threshold.

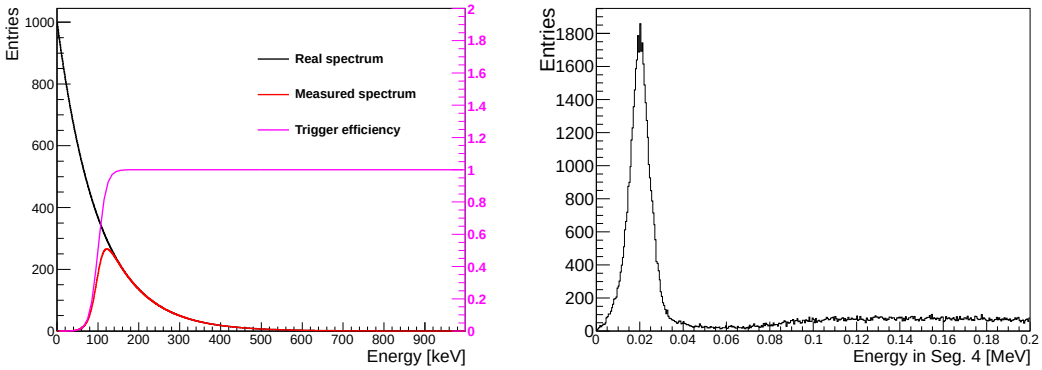

(a) Simulation (b) Example in data

Figure A.3: Demonstration of a noise peak appearing in the energy spectrum.

Appendix B

Optimization and parallelization of occupancy calculation

The occupancy analysis described in Section 7.3.4 required processing of several sets of simulation samples, four for the *top* case and two for the *side* case, plus several more for the systematic studies. The total number of events was about 500 millions and the occupied disk space was 70 GB. The analysis programs were optimized to increase the computational speed and to effectively use available CPU resources. Initially, the total computational CPU time needed to fill the occupancy histograms for all segmentation schemes was several hours. The optimization consisted of two parts:

1. code optimization to reduce the number of unnecessary C++ commands executed by ROOT;
2. code parallelization to use several CPUs at the same time.

An optimization of the code was used to replace slow commands with their faster analogues. Examples are the following:

- Local loop variables become global. An example before and after the change is shown below. The improvement in speed is $O(10\%)$. Usually this case optimization is done by the compiler option **-O2**, i.e. when using **g++ -O2**.

```
for (int i=0..1000000)
{
  int var = 1;
}
```

```
int var;
for (int i=0..1000000)
{
  var = 1;
}
```

- Deactivate unused ROOT branches. This will tell ROOT not to read deactivated branches. An example before and after the change is shown below. The total improvement in speed is proportional to the ratio between the size for of unused branches and the size of used ones. For the current analysis, this ratio was about two.

```
TChain* ch = new TChain("wfTree");
int hits_totnum;
ch->SetBranchAddress("hits_totnum", hits_totnum);
for (int i=0; i<ch->GetEntries(); i++)
{
  ch->GetEntry(i);
  cout<<hits_totnum<<endl;
}
```

```
TChain* ch = new TChain("wfTree");
ch->SetBranchStatus("*", 0);
int hits_totnum;
ch->SetBranchStatus("hits_totnum", 1);
ch->SetBranchAddress("hits_totnum", hits_totnum);
for (int i=0; i<ch->GetEntries(); i++)
{
  ch->GetEntry(i);
  cout<<hits_totnum<<endl;
}
```

- Replace the **TH1::Fill()** command with filling an array. The Fill() command calls many additional functions that slow down the program. An example before and after the change is shown below. The improvement in speed was $O(50\%)$.

```
TH1F* hist = new TH1F("hits", "hits", 100, 0, 100);
for (int i=0; i<ch->GetEntries(); i++)
{
  ch->GetEntry(i);
  hist->Fill(hits_totnum);
}
```

```
int hits_content[100];
for (int i=0; i<ch->GetEntries(); i++)
{
  ch->GetEntry(i);
  hist_content[hits_totnum]++;
}
TH1F* hist = new TH1F("hits", "hits", 100, 0, 100);
for (int j=0; j<100; j++)
{
  hist->SetBinContent(j+1, hist_content[j]);
  hist->SetBinError(j+1, sqrt(hist_content[j]));
}
hist->Sumw2();
```

Beyond code optimization, the code was adjusted to run on several threads using a many-core machine. The analysis is ROOT-based, where data is transferred for each event

[1]. The PROOF (Parallel ROOt Facility) [110] was used to process several events in parallel. It is well known that disk access dominates the processing time. The reading system of PROOF is optimized to read several thousand entries from a .root file at once and send these events to several PROOF processes, *servers*, running locally or on a cluster. It leads to a proportional scaling of the event processing, i.e. the computational speed is proportional to the number of cores/threads used. However, the proportionality vanishes if the data is accessed via a network.

There are several limitations using PROOF. First of all, it requires a selector, **TSelector**-inherited object, created for the analysis. Second, the input parameters and the output, i.e. histograms or arrays, has to be retrieved via the PROOF manager. A direct insertion of parameters into a PROOF thread is not implemented.

The PC used to produce benchmark results had an Intel Core i7 930 CPU (4 cores × 2 threads @ 2.8 GHz with 8 MB L3 cache) with 12 GB RAM, running Ubuntu 10.04 LTS 64-bit linux with a 500 GB hard disk. As a benchmark, the analysis for the ^{60}Co 1.17 MeV gamma line was performed. Simulated histograms were filled for 90 different segmentation angles. To remove the bias from internal caching of the hard disk, the tests were run three times and the last measured time was recorded. The benchmark time for different steps of optimization and parallelization is shown in Table B.1.

Optimization level	Time, s
Non-optimized, 1-thread, no PROOF	180
Optimized, 1-thread, no PROOF	95
Optimized, 1-thread, PROOF	115
Optimized, 4×2-threads, PROOF	25

Table B.1: Computation time for 8.5 M events

Other alternatives, such as CUDA and OpenMP, were tested for parallelization. None of them could be used to create a satisfactory solution for the ROOT-based analysis. CUDA is more suitable for the cases where a large set of data is processed without constant transfer of data between memories of different kinds like GPU RAM and system RAM. For the present analysis, CUDA slows down the computation by up to a factor of 10. The OpenMP system was at the time this work was done a GNU C++-native and did not require any additional software to be installed. But the parallel threads have to be blocked in order to read .root-files from the hard disk and fill the branch variables. Therefore, the parallel approach is lost, so that no improvement in processing speed was observed.

[1]This is the simplest case. In reality, however, a set of events is cached with the buffer size of 10 MB.

Appendix C

Derivation of the cone intersection with a sphere

A circular cone with the vertex at $(0, 0, 0)$ and the axis being aligned to the z-axis can be defined using the following equation in the Cartesian coordinates:

$$x^2 + y^2 - z^2 \ \tan^2 \Omega = 0, \tag{C.1}$$

where (x, y, z) is a point on the cone and Ω is the half-aperture. To be more precise, in the analysis described in Section 8.3, we are only interested in a one-side cone with $z \geq 0$. This will be used later in this chapter. A cone with the axis vector directed arbitrary in (θ_0, ϕ_0) can be obtained by applying a rotational transformation. In the first step, we applied the rotation around the y axis:

$$\begin{aligned} x' &= x \cos\theta_0 - z \sin\theta_0, \\ z' &= x \sin\theta_0 + z \cos\theta_0. \end{aligned} \tag{C.2}$$

Such a transformation brings the cone equation to the following form:

$$\begin{aligned} &x^2 \left(\cos^2\theta_0 - \sin^2\theta_0 \tan^2\Omega\right) - 2xz \cos\theta_0 \sin\theta_0 \left(1 + \tan^2\Omega\right) + \\ &z^2 \left(\sin^2\theta_0 - \cos^2\theta_0 \tan^2\Omega\right) + y^2 = 0. \end{aligned} \tag{C.3}$$

Taking into account simple trigonometrical equalities,

$$\begin{aligned} \cos^2\theta_0 - \sin^2\theta_0 \tan^2\Omega &= 1 - \sin^2\theta_0 - \sin^2\theta_0 \tan^2\Omega \\ &= 1 - \sin^2\theta_0 \left(1 + \tan^2\Omega\right) = 1 - \frac{\sin^2\theta_0}{\cos^2\Omega}, \\ \sin^2\theta_0 - \cos^2\theta_0 \tan^2\Omega &= 1 - \cos^2\theta_0 - \cos^2\theta_0 \tan^2\Omega \\ &= 1 - \cos^2\theta_0 \left(1 + \tan^2\Omega\right) = 1 - \frac{\cos^2\theta_0}{\cos^2\Omega}, \end{aligned} \tag{C.4}$$

Equation C.3 can be written as

$$x^2 \left(1 - \frac{\sin^2\theta_0}{\cos^2\Omega}\right) - 2xz \frac{\cos\theta_0 \sin\theta_0}{\cos^2\Omega} + z^2 \left(1 - \frac{\cos^2\theta_0}{\cos^2\Omega}\right) + y^2 = 0. \tag{C.5}$$

We now can change to the spherical coordinates:

$$\begin{aligned} x &= R\sin\theta\cos\phi, \\ y &= R\sin\theta\sin\phi, \\ z &= R\cos\theta, \end{aligned} \tag{C.6}$$

and substitute this into Eq. C.5. It is easily seen that the R coordinate will cancel. The resulting cone equation in spherical coordinates is now

$$\begin{aligned} &\sin^2\theta\cos^2\phi\left(1-\frac{\sin^2\theta_0}{\cos^2\Omega}\right) - 2\cos\theta\sin\theta\cos\phi\ \frac{\cos\theta_0\sin\theta_0}{\cos^2\Omega}\ + \\ &+\cos^2\theta\left(1-\frac{\cos^2\theta_0}{\cos^2\Omega}\right) + \sin^2\theta\sin^2\phi = 0. \end{aligned} \tag{C.7}$$

After expansion of the brackets, the terms containing $\sin^2\theta, \cos^2\theta$ and $\sin^2\phi, \cos^2\phi$ will give unity. The equation can be then written as

$$1 = \cos^2\phi\sin^2\theta\ \frac{\sin^2\theta_0}{\cos^2\Omega} + 2\cos\phi\cos\theta\sin\theta\ \frac{\cos\theta_0\sin\theta_0}{\cos^2\Omega} + \cos^2\theta\ \frac{\cos^2\theta_0}{\cos^2\Omega}, \tag{C.8}$$

or

$$\cos^2\Omega = \left(\cos\phi\sin\theta\sin\theta_0 + \cos\theta\cos\theta_0\right)^2, \tag{C.9}$$

which gives a simple equation

$$\pm\cos\Omega = \cos\phi\sin\theta\sin\theta_0 + \cos\theta\cos\theta_0. \tag{C.10}$$

The $\pm$ sign represents the both cones, with negative and positive z coordinates. As only $z \geq 0$ are considered, only the "+" sign remains.

The equation of the cone with the axis aligned with the (θ_0, ϕ_0) line can be performed by rotating the coordinates around the z axis. It is a trivial change of the ϕ angle by ϕ_0. The cone can be now parametrized as a $\phi(\theta)$ dependence:

$$\cos\left(\phi-\phi_0\right) = \frac{\cos\Omega - \cos\theta\cos\theta_0}{\sin\theta\sin\theta_0}. \tag{C.11}$$

Bibliography

[1] I. Abt *et al.*, arXiv:hep-ex/0404039.

[2] H. V. Klapdor-Kleingrothaus *et al.*, Phys. Lett. B **586** (2004) 198.

[3] G. W. Rodeback, J. S. Allen, Phys. Rev. **86** (1952) 446.

[4] F. Reines, C. L. Cowan, Jr., Phys. Rev. **92** (1953) 830.

[5] F. Reines, C. L. Cowan, Jr., Nature **178** (1956) 446,
Nature **178** (1956) 523 (erratum),
F. Reines, C. L. Cowan, Jr., Science **124** (1956) 103.

[6] R. Davis, Jr., Phys. Rev. **97** (1955) 766.

[7] B. Pontecorvo, ЖЭТФ **3** (1957) 549-551 (in Russian), Sov. Phys. JETP **6** (1957) 429.

[8] G. Danby *et al.*, Phys. Rev. Lett. **9** (1962) 36.

[9] M. L. Perl *et al.*, Phys. Rev. Lett. **35** (1975) 1489.

[10] K. Kodama *et al.* [DONUT Collaboration], Phys. Lett. B **504** (2000) 218.

[11] R. N. Mohapatra, G. Senjanovic, Phys. Rev. Lett. **44** (1980) 912.

[12] B. Pontecorvo, ЖЭТФ **53** (1967) 1717 (in Russian), Sov. Phys. JETP **26** (1967) 984.

[13] B. Pontecorvo, ЖЭТФ **33** (1957) 549 (in Russian), Sov. Phys. JETP **6** (1957) 429.

[14] B. Pontecorvo, ЖЭТФ **34** (1957) 247 (in Russian), Sov. Phys. JETP **7** (1957) 172.

[15] Z. Maki, M. Nakagawa, and S. Sakata, Prog. Theor. Phys **28** (1962) 870.

[16] M. Doi *et al.*, Phys. Lett. B**102** (1981) 323.

[17] Kai Zuber, *Neutrino Physics*, IOP publishing Ltd (2004).

[18] W. N. Cottingham, D. A. Greenwood, *An Introduction to the Standard Model of Particle Physics*, Cambridge University Press (2007).

[19] K. Nakamura *et al.*, *Particle Data Group*, J. Phys. G **37** (2010) 075021.

[20] J. N. Bahcall, A. M. Serenelli, *Neutrinos in Particle Physics, Astrophysics and Cosmology*, Summer School Proceedings, ed. F. J. P. Soler, Colin D. Froggatt, Franz Muheim, CRC Press, p.119 (2009).

[21] R. Davis, Phys. Rev. Lett. **12** (1964) 303.

[22] W. Hampel *et al.* [GALLEX Collaboration], Phys. Lett. B **447** (1999) 127.

[23] V. Garvin *et al.* [SAGE Collaboration], TAUP 2003 conference, Seattle (2003), Paper URL http://dx.doi.org/10.1016/S0920-5632(03)01302-1.

[24] F. P. An *et al.* [Daya Bay Collaboration], arXiv:1203.1669 [hep-ex].

[25] http://pdglive.lbl.gov. **Remark**: the content changes every two years.

[26] L. Wolfenstein, Phys. Rev. D **17** (1978) 2369,
S. P. Mikheev and A. Yu. Smirnov, Il Nuovo Cimento C **9** (1986) 17.

[27] Q. R. Ahmad *et al.* [SNO Collaboration], Phys. Rev. Lett. **87** (2002) 071301.

[28] Ch. Kraus *et al.*, Eur. Phys. J. C **40** (2003) 447.

[29] V. M. Lobashev *et al.*, Nucl. Phys. A **719** (2003) C153.

[30] Ch. Weinheimer *et al.* [KATRIN Collaboration],
Progr. in Part. and Nucl. Phys. **48** (2002) 141.

[31] M. Sisti *et al.*, Nucl. Instrum. Meth. A **520** (2004) 125.

[32] A. Nucciotti *et al.* [MARE Collaboration], arXiv:1012.2290 [hep-ex].

[33] K. Assamagan *et al.*, Phys. Rev. D **53** (1996) 6065.

[34] R. McNulty, Nucl. Phys. B(*Proc. Suppl.*) **76** (1999) 409.

[35] W. Buchmüller, P. Di Bari, M. Plümacher, Nucl. Phys. B **665** (2003) 445.

[36] R. B. Firestone *et. al*, Table of Isotopes, CD ROM Edition, March 1996.

[37] F. Avignone, S. Elliott, J. Engel, Rev. Mod. Phys. **80** (2008) 481.

[38] A. S. Barabash, AIP Conf. Proc. **1180** (2009) 6.

[39] J. J. Gómez-Cadenas *et al.*, J. Cosm. Astropart. Phys. **06** (2011) 007,
pre-print arXiv:1010.5112[hep-ex].

[40] A. Caldwell and K. Kröninger, Phys. Rev. D. **74** (2006) 092003.

[41] R. Arnold *et al.*, Nucl. Instrum. Meth. A **536** (2005) 79,
URL NEMO 3 publications.

[42] G. Audi *et al.*, Nucl. Phys. A **729** (2003) 3.

[43] C. E. Aalseth *et al.* [IGEX Collaboration] Phys. Rev. D. **65** (2002) 092007.

[44] H. V. Klapdor-Kleingrothaus, I. V. Krivosheina, Mod. Phys. Lett. A **21** (2006) 1547.

[45] I. V. Kirpichnikov, arXiV:1006.2025 [hep-ph].

[46] L. Baudis *et al.*, Phys. Rev. Lett. **83** (1999) 41.

[47] K. V. Klapdor-Kleingrothaus *et al.*, Eur. Phys. J. A **12** (2001) 147.

[48] A. S. Barabash, Phys. Part. Nucl. **42** (2011) 613.

[49] GERDA Collaboration, *Progress Report to the LNGS Scientic Committee - March 2006*,
URL http://www.mpi-hd.mpg.de/gerda/reportsLNGS/gerda-lngs-sc-mar06.pdf

[50] H. Simgen, G. Zuzel, Appl. Rad. Isot. **67** (2009) 922.

[51] J. Janicskó Csáthy, Nucl. Instrum. Meth. A **654** (2011) 225.

[52] J. Janicskó Csáthy for the GERDA collaboration, DPG Spring meeting, "Hadronen und Kerne" (March 2012), talk from the public GERDA webpage
http://www.mpi-hd.mpg.de/gerda/public/2012/t12_dpg_mzHK18.2_jj.pdf.

[53] M. Knapp for the GERDA collaboration, Neutrino Champagne,
5th workshop on Low Energy Neutrino Physics, Reims, France (2009),
talk from the public GERDA webpage:
http://www.mpi-hd.mpg.de/ge76/public/2009/p09_lownu09_muonveto_mk.pdf.

[54] B. Lehnert, *Analysis of Double Beta Decays in Germanium, Palladium and Argon*, Diploma thesis, TU Dresden (2011),
http://iktp.tu-dresden.de/IKTP/pub/11/blehnert_thesis_u1.pdf.

[55] L. Baudis *et al.*, arXiv:hep-ex/0012022

[56] S. Hemmer for the GERDA collaboration, XXVI Rencontres de Physique de La Vallee d'Aoste, La Thuile, Italy (2012), talk from the public GERDA webpage:
http://www.mpi-hd.mpg.de/ge76/public/2012/t12_lathuile_gerda_sh.pdf,
proceedings to be published.

[57] GERDA MediaWiki: list of run configurations, internal,
http://www.mpi-hd.mpg.de/gerdawiki/index.php/GERDA_Analysis.

[58] S. Schönert for the GERDA collaboration, 14th Venice Neutrino Telescope, Venice (2011), talk from the public GERDA webpage:
http://www.mpi-hd.mpg.de/ge76/public/2011/t11_nutel_gerda_sts.pdf.

[59] P. Benetti *et al.*, Nucl. Instrum. Meth. A **574** (2007) 83.

[60] C Dörr, H. V Klapdor-Kleingrothaus, Nucl. Instrum. Meth. A **513** (2003) 596.

[61] G. Knoll, *Radiation Detection and Measurement*, 3rd edn., (Wiley, New York, 1999), 816 pages.

[62] J. Eberth, J. Simpson, Prog. Part. Nucl. Phys. **60** (2008) 283.

[63] I-Yang Lee, J. Simpson, Nucl. Phys. News, **20**, Issue 4, (2010) 23.

[64] I. Abt *et al.*, Nucl. Instrum. Meth. A **583** (2007) 332.

[65] V. Radeka, Ann. Rev. Nucl. Part. Sci. **38** (1988) 217.

[66] Z. He, Nucl. Instrum. Meth. A **463** (2000) 250.

[67] I. Abt *et al.*, Nucl. Instrum. Meth. A **577** (2007) 574.

[68] M. S. Tyagi, *Introduction to semiconductors materials and devices*, (Wiley, Ney York, 1991), 688 pages.

[69] Charles Kittel, *Introduction to Solid State Physics*, 8th edn., (Wiley, Ney York, 2008), 704 pages.

[70] B. Bruyneel *et al.*, Nucl. Instrum. Meth. A **569** (2006) 764.

[71] I. Abt *et al.*, Eur. Phys. J. C **68** (2010) 3.

[72] W. Shockley, Bell System Tech. **30** (1951) 990.

[73] M. Shibuya, Phys. Rev. **99** (1955) 1189.

[74] W. Sasaki, M. Shibuya, J. Phys. Soc. Jpn. **11** (1956) 1202.

[75] J. Bardeen, W. Shockley, Phys. Rev. **80** (1950) 72.

[76] M. B. Prince, Phys.Rev. **92** (1954) 681.

[77] F. J. Morin, Phys.Rev. **93** (1954) 62.

[78] J. Liu, *Development of Segmented Germanium Detectors for Neutrinoless Double Beta Decay Experiments*, PhD thesis, TU Munich (2009), http://mediatum2.ub.tum.de/node?id=701884.

[79] http://www.xia.com/DGF_Pixie-4_Download.html.

[80] I. Abt *et al.*, JINST **4** (2009) P11008.

[81] I. Abt *et al.*, Eur. Phys. J. Appl. Phys. **56** (2011) 10104.

[82] I. Abt *et al.*, Eur. Phys. J. C **72**, (2012) 1950.

[83] K. Kröninger, *Techniques to distinguish between electron and photon induced events using segmented germanium detectors*, PhD thesis, TU Munich (2007), http://mediatum2.ub.tum.de/node?id=618987.

[84] D. Lenz, *Pulse Shapes and Surface Effects in Segmented Germanium Detectors*, PhD thesis, TU Munich (2010), http://mediatum2.ub.tum.de/node?id=969435.

[85] K. Kroeninger, F. Froborg, X. Liu, L. Pandola, J. Schubert, Simulation of the GERDA setup using MAGE within the MCC2 campaign, Internal reports.

[86] M. Boswell *et al.*, IEEE Trans. Nucl. Sci. **58** (2011) 1212.

[87] S. Agostinelli *et al.*, Nucl. Instrum. Meth. A **506** (2003) 250; J. Allison *et al.*, IEEE Trans. Nucl. Sci. **53** (2006) 270.

[88] M. Laubenstein, private communication, Laboratori Nazionali del Gran Sasso, Assergi, Italy.

[89] B. Majorovits *et al.* Nucl. Instrum. Meth. A **647** (2011) 39.

[90] B. Majorovits, *Limitations of next generation neutrinoless double beta-decay germanium experiments*, Habilitation thesis, TU Munich (2011), http://publications.mppmu.mpg.de/2011/MPP-2011-160/FullText.pdf.

[91] R. Quinkertz, *Optimierung der Energienutzung bei der Aluminiumherstellung*, PhD thesis, RWTH Aachen (2002), http://d-nb.info/965686876.

[92] G. Taylor *et al.*, Austral. J. Earth Sci., **55** Suppl. 1 (2008) S45.

[93] J. F. Ziegler, IBM Res. Develop. **42** (1998) 117; J. F. Ziegler, IBM Res. Develop. **40** (1996) 19.

[94] H. Filthuth, Il Nuovo Cimento, Vol. 4, Suppl. 2 (1956) 906.

[95] I. Abt *et al.*, Nucl. Instrum. Meth. A **570** (2007) 479.

[96] F. Petry *et al.*, Nucl. Instrum. Meth. A **332** (1993) 107.

[97] S. R. Elliott *et al.*, Nucl. Instrum. Meth. A **558** (2006) 504.

[98] I. Abt *et al.*, Eur. Phys. J. C **52** (2007) 19.

[99] F. C. L. Crespi *et al.*, Nucl. Instrum. Meth. A **570** (2007) 459.

[100] B. Majorovits, H. V. Klapdor-Kleingrothaus, Eur. Phys. J. A **76** (1999) 463.

[101] C. G. Broyden, IMA J. Appl. Math. **6** (1970) 222, R. Fletcher, Computer J. **13** (1970) 317, D. Goldfarb, Math. Comp. **24** (1970), 23, D. F. Shanno, Math. Comp. **24** (1970), 647, D. F. Shanno, J. Optimiz. Theor. Appl. **46** (1985) 87.

[102] M. Agostini *et al.*, JINST **6** (2011) P08013.

[103] *Canberra manual on Gerda Detector-2 (Siegfried-II)* (2007).

[104] A. Caldwell, D. Kollar, K. Kröninger, Comp. Phys. Commun. **180** (2009) 2197.

[105] K. Irmscher, private communication, Leibniz-Institut für Kristallzüchtung, Berlin.

[106] Andrew S. Hoover *et al.*, Proc. SPIE **5540** (2004) 124.

[107] F. Recchia, *In-beam test and imaging capabilities of the AGATA prototype detector*, PhD thesis, University of Padova (2008), http://paduaresearch.cab.unipd.it/894/.

[108] F. Recchia *et al.*, Nucl. Instrum. Meth. A **604** (2009) 60.

[109] B. Bruyneel *et al.*, Nucl. Instrum. Meth. A **608** (2006) 99.

[110] PROOF-Parallel ROOt Facility, Nucl. Instrum. Meth. A **559** (2006) 13, URL http://root.cern.ch/drupal/content/proof.

Thank you!

It has been a long, challenging and interesting way along my PhD route and I would have never completed it without the help of other people. First of all, I want to thank Prof. Allen Caldwell for the possibility to work in his group. Many many thanks goes to Dr. Béla Majorovits for his excellent support, encouragement and "tasks-for-tomorrow" that was a real fun to complete on time. A special gratitude is addressed to Dr. Iris Abt. In any situation she could always find proper words to inspire and motivate. She taught me a lot of things, especially how to do physics in the most constructive and efficient way. I very much appreciate Iris's and Béla's patience while reading my thesis. Thank you for using your red pens!

Another big piece of thanks goes to Fabiana Cossavella for a very collaborative work together on pulse shape analysis and for being a good friend over these years.

I want to thank the former members of the group, Xiang, Jing and Daniel, for helping me in the first days of my PhD and getting me fast into the business. I received a lot of help and advises from Jason, Luciano and Matteo about C++ and GEANT4. Thank you for that. Additional thanks go to Aaron, Sabine and Sabine for the help with my German. A significant part of the thanks goes to Aaron and Nesli for being best officemates.

It was a lot of fun to feel the atmosphere of the whole Munich GERDA/GeDet group. I will never forget after-meeting Beergarten visits, physics questions, Christmas markets, Oktoberfests, and many other things that were making me happy. I want to thank Chris, Burçin, Oliver, Heng Ye, Lucia and Matteo, whom I did not thank yet but who definitely deserve it. My thanks also go to the interns and summer students and in particular Petar for his help that in the end contributed to a completion of the axes paper.

I want to thank my friends Max for a constant supply with new Metal without which I could not work and Stas for infecting me with long distance biking, which indeed is a very good leisure.

In the end, I want to gratefully and sincerely thank my wife Lena and my whole family, my mom and dad, my brother, granny, uncle and my mother-in-law. You never let me forget that there is something else in this world that are worth noticing apart from physics and computers. **Спасибо вам большое!**